STRUCTURE-CONDUCTIVITY STUDIES IN POLYMER ELECTROLYTES CONTAINING MULTIVALENT CATIONS

by

Madzlan Aziz, B.Sc(Hons), M.Sc.

A thesis presented in partial fulfilment of the requirements for the degree of Doctor of Philosophy awarded by De Montfort University.

Chemistry Department
School of Applied Sciences
De Montfort University
Leicester.

Mac 1996

Structure -Conductivity Studies in Polymer Electrolytes Containing Multivalent Cations.

by
Madzlan Aziz

Abstract

Understanding the structure - conductivity relationship is of paramount importance for the development of polymer electrolytes. The present studies present the techniques found useful in the elucidation of structure - conductivity relationship in PEO_n:$ZnBr_2$ (n = 8, 1000, 2000, 3000, 4000 and 5000) and PEO_n:$FeBr_x$ (n = 8, 20 and 50; x = 2 and 3).

Local structural studies have been undertaken using X-ray absorption fine structures (XAFS) which includes extended X-ray absorption fine structure (EXAFS) and X-ray absorption near edge structure (XANES). EXAFS provides interatomic distance and coordination numbers of the nearest neighbours and results from the EXAFS studies showed that high conductivity is associated with stretched M - O interatomic distance. In the studies on ultra dilute Zn samples it was found that the cation is highly solvated by the heteroatom forming a tightly bound environment which inhibits local segmental motion thus impeding ion migration. XANES studies on the PEO and modified PEO complexes of $NiBr_2$ revealed the sensitivity of XANES to the structural differences. XANES on Zn and Fe samples also revealed the sensitivity to changes in interatomic distances reflected in shifts of the white line. The complementary nature of EXAFS and XANES was reflected in the studies conducted.

Morphological studies were undertaken employing differential scanning calorimetry (DSC), variable temperature polarising microscopy (VTPM) and atomic force microscopy (AFM). DSC evidences helped to explain the texture of the iron samples during the drying process, and showed transitions between low melting, PEO and high melting spherulites, and VTPM is able to visualise the spherulites present in the samples. AFM has successfully imaged the as cast PEO_8:$FeBr_2$ sample and the surface effect causing extra resistance in the impedance spectra could be seen.

Conductivity studies were carried out using a.c. impedance spectra. Fe(II) samples exhibit the typical semicircle-spike plot but the Fe(III) samples displayed an extra semicircle before the spike reflecting a surface effect. This is also manifested in the Arrhenius plots of the same samples where a dip was shown at 100°C. From the conductivity studies on the iron systems it was found that for the dry samples the optimum conductivity was observed in PEO_8:$FeBr_x$ irrespective of the valence state of the cation. For the air-cast samples the optimum conductivity composition depends on the valence state and were shown to be at more dilute compositions.

Abstract

Understanding the structure - conductivity relationship is of paramount importance for the development of polymer electrolytes. The present studies present the techniques found useful in the elucidation of structure - conductivity relationship in $PEO_n:ZnBr_2$ (n = 8, 1000, 2000, 3000, 4000 and 5000) and $PEO_n:FeBr_x$ (n = 8, 20 and 50; x = 2 and 3).

Local structural studies have been undertaken using X-ray absorption fine structures (XAFS) which includes extended X-ray absorption fine structure (EXAFS) and X-ray absorption near edge structure (XANES). EXAFS provides interatomic distance and coordination numbers of the nearest neighbours and results from the EXAFS studies showed that high conductivity is associated with stretched M - O interatomic distance. In the studies on ultra dilute Zn samples it was found that the cation is highly solvated by the heteroatom forming a tightly bound environment which inhibits local segmental motion thus impeding ion migration. XANES studies on the PEO and modified PEO complexes of $NiBr_2$ revealed the sensitivity of XANES to the structural differences. XANES on Zn and Fe samples also revealed the sensitivity to changes in interatomic distances reflected in shifts of the white line. The complementary nature of EXAFS and XANES was reflected in the studies conducted.

Morphological studies were undertaken employing differential scanning calorimetry (DSC), variable temperature polarising microscopy (VTPM) and atomic force microscopy (AFM). DSC evidences helped to explain the texture of the iron samples during the drying process, and showed transitions between low melting, PEO and high melting spherulites, and VTPM is able to visualise the spherulites present in the samples. AFM has successfully imaged the as cast $PEO_8:FeBr_2$ sample and the surface effect causing extra resistance in the impedance spectra could be seen.

Conductivity studies were carried out using a.c. impedance spectra. Fe(II) samples exhibit the typical semicircle-spike plot but the Fe(III) samples displayed an extra semicircle before the spike reflecting a surface effect. This is also manifested in the Arrhenius plots of the same samples where a dip was shown at 100°C. From the conductivity studies on the iron systems it was found that for the dry samples the optimum conductivity was observed in $PEO_8:FeBr_x$ irrespective of the valence state of the cation. For the air-cast samples the optimum conductivity composition depends on the valence state and were shown to be at more dilute compositions.

Declaration

The work in this thesis was carried out by the author, in the Department of Chemistry, School of Applied Science at De Montfort University, between October 1992 and July 1995. None of the work has been submitted for any other degree or qualification.

Signed .....

Date 16/3/96

Acknowledgements

I would like to express my appreciation and gratitude to my supervisors, Prof. R.G. Linford, Dr. R.J. Latham and Dr. W.S. Schlindwein.

I am indebted to the technical and research staff of the School of Applied Sciences, Dr. D. Armitage, Mrs. N. Garrington and Mr. H. Harron.

I would also like to thank the Public Service Department of the Malaysian Government and Universiti Teknologi Malaysia for sponsoring all the expenses throughout the duration of this work.

Last but not least special thanks to my wife Sharifah and my six children for all the considerations given.

Table of Contents

Chapter One: Introduction

1.0 Aims and Objectives 1

1.1 Research Methodology 3

1.2 The Host Polymer 4

1.3 Poly(ethylene oxide)-based Polymer Electrolytes 7

1.4 Interionic and Ion-polymer Interaction in Polymer Electrolytes 11

1.5 Morphology of Polymer Electrolytes 13

1.6 Ionic Conductivity of Polymer Electrolytes 16

Chapter Two: Principles of Techniques

2.0 Introduction 24

2.1 Alternating Current (a.c) Impedance 24

2.1.1 The Essence of Impedance Spectroscopy 25

2.1.2 The Principles of Impedance Spectra 27

2.1.3 The ac Response of Cells Containing Polymer Electrolytes 31

2.2 X-ray Absorption Fine Structure (XAFS) 38

2.2.1 X-rays 38

2.2.2 Extended X-ray Absorption Fine Structure (EXAFS) 42

2.2.2.1 Theory 43

2.2.2.2 Data Analysis 47

2.2.3 X-ray Absorption Near Edge Structure (XANES) 50

2.3 Differential Scanning Calorimetry (DSC) 58

2.4 Variable Temperature Polarising Microscopy (VTPM) 60

2.4.1 Polarising Microscopy 60

2.4.2 Variable Temperature 63

Chapter Three: Experimental Details of Characterisation Techniques

3.0 Introduction 64

3.1 X-ray Absorption Fine Structures (XAFS) 64

3.1.1 Instrumentation 65

3.1.2 Sampling 68

3.1.3 Data Acquisition 69

3.2 A.C Impedance Spectroscopy 69

3.3 Differential Scanning Calorimetry (DSC) 71

3.4 Variable Temperature Polarising Microscopy (VTPM) 72

Chapter Four: XANES Studies on Nickel Systems

4.0 Introduction 73

4.1 The Samples 73

4.2 Experimental of XAFS Studies 74

4.3 Results 74

4.4 Comment on Results 76

Chapter Five: Structure-Conductivity Studies in Zinc Systems

5.0 Introduction 78

5.1 Structure -Conductivity Studies on PEO_8:$ZnBr_2$ 78

5.1.1 Sample Preparation 78

5.1.2 Experimental 80

5.1.3 Results 81

5.1.4 Comments on Results 86

5.2 Structure-Conductivity Studies on Zinc Ultra-dilute Systems 88

5.2.1 Sample Preparation 88

5.2.2 XAFS Studies 90

5.2.2.1 XANES Results 90

5.2.2.2 EXAFS Results 93

5.2.3 Conductivity Studies 99

5.2.4 DSC Studies 105

5.2.5 VTPM Studies 107

5.2.6 Overview of Zinc Ultra dilute Systems 114

Chapter Six: Iron (II) and Iron (III) Systems

6.0 Introduction 117

6.1 Materials and Preparation 117

6.1.1 Results 119

6.2 X-ray Absorption Fine Structure (XAFS) Studies 119

6.2.1 XANES Results 120

6.2.2 EXAFS Results 129

6.2.3 Comments on Results 139

6.3 Conductivity Studies 141

6.3.1 Comments on Results 150

6.4 Differential Scanning Calorimetry (DSC) Studies 152

6.4.1 Comments on Results 155

6.5 Atomic Force Microscopy (AFM) 156

6.5.1 Introduction 156

6.5.2 Experimental 159

6.5.3 Results 159

6.5.4 Comments on Results 165

6.6 Overview of Iron Systems 166

Chapter Seven: Discussion and Conclusions

7.0 Introduction 168

7.1 Structural Studies 168

7.2 Conductivity 177

7.3 Structure-Conductivity Relationships 178

7.4 Conclusions 180

7.5 Further Studies 182

References 184

List of Figures

Figure 1.1	The helical structure of PEO.	5
Figure 1.2	Structure of crystalline PEO_3:$NaClO_4$	14
Figure 1.3	Arrangement of polymer chains in a spherulite.	15
Figure 1.4	Formation of transient crosslinks through (a) a cation and (b) a triple ion.	18
Figure 1.5	The three regions of conductivity in polymer electrolytes.	19
Figure 2.1	Complex impedance plots for a combination of a resistor, *R*, and capacitor, *C*, (a) in series and (b) in parallel.	30
Figure 2.2	Schematic representation of a blocking electrode cell and the equivalent circuit.	32
Figure 2.3	Simulated complex impedance plot for a blocking electrode cell.	33
Figure 2.4	Equivalent circuit and complex impedance plot for electrolyte having one mobile ion with non-blocking electrode.	34
Figure 2.5	Equivalent circuit and complex impedance plot for electrolyte having more than one mobile ions with electrode which is non-blocking to cation only.	35
Figure 2.6	Equivalent circuit and complex impedance plane plot for polymer electrolyte cell exhibiting diffusion-controlled migration of an electroactive ion.	37
Figure 2.7	Interactions of photons with the core levels of an atom emitting fluorescent photons.	40

Figure 2.8 Qualitative rationalisation of EXAFS in one neighbour environment. 43

Figure 2.9 The near edge structure window of the absorption spectra. 51

Figure 2.10 Pictorial view of photoelectron scatering processes in the multiple scattering regime of XANES. 52

Figure 2.11 Schematic representation of a typical X-ray absorption spectra of a transition metal with A as 1*s* -----> 3*d*, B as 1*s* -----> 4*s* and C as 1*s* -----> 4*p*. 56

Figure 2.12 A simplified molecular orbital diagram illustrating the potential ligand to metal charge transfer transitions. 57

Figure 2.13 Illustration of the representation of a DSC system. 58

Figure 2.14 A typical DSC curve of a polymer electrolyte. 59

Figure 2.15 Plane polarised light hitting a birefringent object is split into two rays parallel to each of the directions of refractive index, resulting in different phase retardation for each set of rays. 61

Figure 2.16 The components of a polarising microscope. 62

Figure 3.1 Schematic representation of the XAFS experimental set up. 64

Figure 3.2 Schematic diagram of a transmission EXAFS experimental set up. 66

Figure 3.3 Schematic configuration of a fluorescence EXAFS experiment. 67

Figure 3.4 EXAFS sample holder used in the experiment. 68

Figure 3.5 Conductivity rig for variable temperature a.c. impedance measurements. 70

Figure 4.1 Nickel K-edge absorption spectra of (a) PEG_8:$NiBr_2$, (b) PPG_8:$NiBr_2$, (c) PEO_8:$NiBr_2$, and (d) PPM_8:$NiBr_2$. 75

Figure 4.2 Nickel K-edge spectra of PEO_8:$NiBr_2$ and PPM_8:$NiBr_2$. 76

Figure 5.1 X-ray absorption spectra of PEO_8:$ZnBr_2$ at (a) room temperature and (b) 90°C. 82

Figure 5.2 Expanded X-ray absorption spectra of PEO_8:$ZnBr_2$ at (a) room temperature, (b) 90°C and (c) room temperature after five hours heated at 90°C for one hour. 83

Figure 5.3 The impedance spectra of PEO_8:$ZnBr_2$ at (a) 90°C and (b) 20°C (after cooling from 90°C). 84

Figure 5.4 XANES window of the K-edge spectra of PEO_n:$ZnBr_2$ (Both the axes are not to scale, comparison plots only). 91

Figure 5.5 Weighted EXAFS spectra in *k*-space and the Fourier transforms of PEO_{1000}:$ZnBr_2$. 94

Figure 5.6 Weighted EXAFS spectra in *k*-space and the Fourier transforms of PEO_{3000}:$ZnBr_2$. 95

Figure 5.7 Impedance spectra of PEO_{1000}:$ZnBr_2$ at (a) 70°C and (b) 120°C. 99

Figure 5.8 Impedance spectra of PEO_{3000}:$ZnBr_2$ at (a) 70°C and (b) 120°C. 100

Figure 5.9 The log conductivity versus the reciprocal of temperature plot of PEO_n:$ZnBr_2$ (n = 1000, 2000, 3000, 4000 and 5000). 102

Figure 5.10 Molar conductivity versus concentration plots at 50°C. 103

Figure 5.11 Molar conductivity versus concentration plots at 100°C. 104

Figure 5.12 DSC traces of (a) PEO_{1000}:$ZnBr_2$ and (b) PEO_{2000}:$ZnBr_2$. 106

Figure 5.13 DSC traces of (a) PEO_{3000}:$ZnBr_2$, (b) PEO_{4000}:$ZnBr_2$ and (c) PEO_{5000}:$ZnBr_2$. 106

Figure 5.14 Micrographs of PEO_{1000}:$ZnBr_2$ at (a) 30°C and (b) 70°C. 108

Figure 5.15 Micrographs of PEO_{1000}:$ZnBr_2$ crystallising at (a) 40°C and (b) 30°C. 109

Figure 5.16 Micrographs of PEO_{3000}:$ZnBr_2$ at (a) 30°C and (b) 70°C. 110

Figure 5.17 Micrographs of PEO_{3000}:$ZnBr_2$ crystallising at (a) 40°C and (b) 30°C. 111

Figure 5.18 Micrographs of PEO_{5000}:$ZnBr_2$ at (a) 30°C and (b) 70°C. 112

Figure 5.19 Micrographs of PEO_{5000}:$ZnBr_2$ crystallising at (a) 40°C and (b) 30°C. 113

Figure 6.1 XANES of (a) $FeBr_2$, (b) PEO_8: $FeBr_2$ (air-cast), and (c) PEO_{50}: $FeBr_2$ (air-cast) 121

Figure 6.2 XANES of (a) PEO_8: $FeBr_2$ (dry), (b) PEO_{20}: $FeBr_2$ (dry) and (c) PEO_{50}: $FeBr_2$ (dry) 122

Figure 6.3 XANES of (a) $FeBr_3$, (b) PEO_8: $FeBr_3$ (air-cast), and (c) PEO_{50}: $FeBr_3$ (air-cast) 123

Figure 6.4 XANES of (a) PEO_8: $FeBr_3$ (dry), (b) PEO_{20}: $FeBr_3$ (dry) and (c) PEO_{50}: $FeBr_3$ (dry) 124

Figure 6.5 XANES of PEO_8: $FeBr_x$ (x = 2 and 3) dry samples at (a) 22°C and (b) 70°C 128

Figure 6.6 *Excurv92* plot of PEO_{20}: $FeBr_2$ dry sample. 135

Figure 6.7 *Excurv92* plot of PEO_{20}: $FeBr_3$ dry sample. 136

Figure 6.8 *Excurv92* plot of PEO_8: $FeBr_2$ dry sample at 70°C. 137

Figure 6.9 *Excurv92* plot of PEO_8: $FeBr_3$ dry sample at 70°C. 138

Figure 6.10 Impedance spectra of PEO_8: $FeBr_2$ at (a) 40°C, (b) 70°C and (c) 100°C. 142

Figure 6.11 Impedance spectra of PEO_8: $FeBr_3$ at (a) 40°C, (b) 50°C and (c) 70°C. 143

Figure 6.12 Arrhenius plots of (a) PEO_8: $FeBr_2$ (Dry sample) and (b) PEO_{20}: $FeBr_2$ (Air-cast) 145

Figure 6.13 Arrhenius plots of (a) PEO_8: $FeBr_2$ (Dry sample) and (b) PEO_8: $FeBr_3$ (Dry sample) 146

Figure 6.14 Arrhenius plots of (a) PEO_8: $FeBr_2$ (Air-cast sample) and (b) PEO_8: $FeBr_2$ (Dry sample) 147

Figure 6.15 DSC traces of PEO_8: $FeBr_2$ and PEO_{20}: $FeBr_2$ dry samples 14

Figure 6.16 DSC traces of PEO_8: $FeBr_3$ and PEO_{20}: $FeBr_3$ dry samples 144

Figure 6.17 DSC traces of PEO_8: $FeBr_2$ and PEO_{20}: $FeBr_2$ air-cast samples 144

Figure 6.18 DSC traces of PEO_8: $FeBr_3$ and PEO_{20}: $FeBr_3$ air-cast samples 145

Figure 6.19 DSC trace of PEO_{50}: $FeBr_2$ air-cast sample 145

Figure 6.20 A schematic diagram of an AFM 149

Figure 6.21 (a) Image of as cast PEO_8: $FeBr_2$ film seen by AFM, (b) with contour lines 151

Figure 6.22 Surface view of the AFM image of the as cast PEO_8: $FeBr_2$ film 152

Figure 6.23 AFM image of a spin coat PEO_8: $FeBr_2$ film 152

Figure 6.24 (a) AFM image of the dilute spin coat PEO_{50}: $FeBr_2$ sample and (b) surface view of the AFM image of the dilute spin coat PEO_{50}: $FeBr_2$ sample 153

Figure 6.25 AFM image of the spin coat PEO_{500}: $FeBr_2$ film 154

Figure 6.26 Surface view of the AFM image of PEO_{500}: $FeBr_2$ film showing the boundary between spherulites and a ridge 155

Figure 6.27 Cross-section of the AFM image of PEO_{500}: $FeBr_2$ film showing the depth of the boundary between spherulites and height of the ridge 155

Figure 7.1 Solvate ion pair in PEO_n: $ZnBr_2$ ($n > 2000$) 171

Figure 7.2 Contact ion pair in PEO_n: $ZnBr_2$ ($n < 2000$) 172

Figure 7.3 Trends between local structure and ionic conductivity in zinc ultradilute samples. 178

List of Tables

Table 5.1 The positions of the main absorption peaks of PEO_8:$ZnBr_2$ at the various conditions. 81

Table 5.2 Conductivity of PEO_8:$ZnBr_2$ at various conditions. 85

Table 5.3 Summary of the amount of PEO_{500}:$ZnBr_2$ required. 89

Table 5.4 Main absorption edge position of PEO_n:$ZnBr_2$. 92

Table 5.5 EXAFS results of zinc model compounds. 94

Table 5.6 EXAFS results of PEO_n:$ZnBr_2$ (n = 1000, 2000, 3000, 4000 and 5000) 95

Table 5.7 Ionic Conductivities of the zinc ultra-dilute samples at different temperatures. 101

Table 6.1 Amount of $FeBr_2$ and $FeBr_3$ needed in the various compositions studied. 118

Table 6.2 Peak positions in the XANES studies on the iron systems. 125

Table 6.3 Peak positions in the heat treatment studies on PEO_8:$FeBr_x$ (x = 2 and 3). 127

Table 6.4a EXAFS results of the iron(II) systems studied. 130

Table 6.4b Literature Data of Fe_2O_3. 130

Table 6.5 EXAFS results of the iron(III) systems studied. 131

Table 6.6 EXAFS results of the heat treatment studies on PEO_8:$FeBr_x$ (x = 2 and 3). 131

Table 6.7 Conductivity values of PEO_n:$FeBr_2$ at different temperatures. 132

Table 6.8 Conductivity values of PEO_n:$FeBr_3$ at different temperatures. 132

Table 6.9 Positions (^{o}C) of the phases observed in the iron samples. 133

Table 6.10 EXAFS results of PEO_8:$FeBr_3$ at various temperatures. 134

Table 6.11 Conductivity values of $PE0_n$:$FeBr_2$ at different temperatures. 148

Table 6.12 Conductivity values of $PE0_n$:$FeBr_3$ at different temperatures. 149

Table 6.13 Positions (^{o}C) of the phases observed in the iron samples. 155

1.0 Aims and Objectives

Portable and powerful is a technological catch phrase for new equipment in the post twentieth century. This applies especially to the power sources used to run equipment. As equipment is being miniaturised through the use of the integrated circuits, the search for a similar scale power source escalates. One such power source is an all-solid-state battery employing a solid polymer electrolyte. Solid polymer electrolytes posses a number of critical attributes required for optimal functioning of a solid state battery including: adequate ionic conductivity, good mechanical properties, good internal interfacial contacts and ease of processing. The most important attribute of all is the ionic conductivity. The idea of using a solid polymer as an electrolyte in lithium batteries was proposed by Armand and co-workers (Armand *et al.*, 1978) after Wright and co-workers (Fenton *et al.*, 1973) measured the conductivities of Na and K salts complexes of poly(ethylene oxide), PEO. Since then substantial effort has been invested in the quest for the right polymer electrolyte.

In PEO-salt systems the metal cation and the oxygen atoms in the ether groups form complexes in which the oxygen atoms form a cage around the cation, leading to dissociation of the anion-cation pair. The complexation is reversible, resulting in ionic conductivity (Yang *et al.*, 1986). Therefore, studying the complexation is crucial for the

understanding of ionic conductivity. However, the relationship between ionic conductivity and the microscopic structure of polymer-salt complexes is not well understood. Originally, it was suggested that ionic conduction in PEO was due to cation hopping within the helical PEO crystal structure (Armand *et al.*, 1979). However, later work showed that in the polymer complex, which consists of crystalline and amorphous phases, the ionic conductivity is associated with the amorphous phase (Sorenson *et al.*, 1983; Berthier *et al.*, 1983), and not the crystalline phase. This implies that the conduction mechanism for this polymer complex is quite different from that for inorganic materials.

It is the objective of this work to try to extend the understanding of the relationship between conductivity and structure in polymer electrolytes. It is not a primary objective to search for a highly conducting system but new polymer electrolyte systems have been prepared and studied in order to elucidate the structure-conductivity relationship. In the effort to establish this relationship divalent and trivalent cations have been chosen to complex with PEO. The group at De Montfort University (formerly Leicester Polytechnic) have put quite an effort into divalent polymer electrolytes studies (Patrick, A.J. 1986; Schlindwein, W.S. 1990; Pynenburg, R.A.J, 1994 and Hagan *et al.*, 1994). In this work four systems were chosen in the quest for better understanding of structure-conductivity relationships:

1. X-ray Absorption Near Edge Structure (XANES) studies of nickel polymer electrolytes systems.

2. The ultra-dilute systems where zinc is the cation as in $PEO_n:ZnBr_2$ (n = 1000, 2000, 3000, 4000 and 5000).
3. The divalent and trivalent iron as cation as in $PEO_n:FeBr_x$ (n = 8, 20, 50, 2000 and 5000; x = 2 and 3); preparation involved casting under dry glove box conditions, hereafter referred to "dry ".
4. The divalent and trivalent iron as cation as in $PEO_n:FeBr_x$ (n = 8, 10, 15, 30, 50 and 100; x = 2 and 3); preparation involved casting in a fume cupboard, hereafter referred to "air cast".

In the nickel systems ($P_8:NiBr_2$; P = PEO, PEG, PPM and PPM) the focus was on structural elucidation based on the XANES features in the X-ray absorption spectra obtained from complexes prepared previously. The zinc system was chosen to study the conductivity behaviour in ultra-dilute systems. In the iron systems studied, the concentrations chosen were that of a high (n=8), medium (n=20), low (n=50) and very low (2000, 5000) configuration. From these systems it is hoped that the charge carriers and the transport mechanism could be proposed.

1.1 Research Methodology

All the studies started with the preparation of the complexes except for the nickel complexes. Apart from the ultra dilute and air cast samples, all the preparative procedures were the same. Conductivity studies were carried out on all the samples, except the nickel

systems, employing the alternating current (AC) impedance technique. The absence of long range order in the amorphous phase responsible for conductivity has ruled out the use of conventional x-ray diffraction in investigations of the microscopic structure. There is a relatively simple and direct means of obtaining information on the local atomic arrangement around a selected atom in complex or disordered systems such as polymer electrolytes. This determination of the local atomic environment of the excited atom is through XAFS studies (X-ray Absorption Fine Structures). XAFS studies constitute the Extended X-ray Absorption Fine Structures (EXAFS) and X-ray Absorption Near Edge Structures (XANES). The thermal behaviour of the complexes were also studied via differential scanning calorimetry (DSC) and variable temperature polarising microscopy (VTPM).

1.2 The Host Polymer

Poly(ethylene) oxide is obtained from the ring-opening polymerization of ethylene oxide. For high molecular weight products, anionic catalysts like calcium amide are required. Polymers with a relative molar mass up to 5×10^6 are commercially available. Poly(ethylene) oxide is a linear polymer and the regularity of the unit allows a high degree of crystallinity involving about 70 - 85% of the polymer. Pure PEO adopts a helical configuration with seven monomer units and a thread of 1.93 nm per unit quadratic cell as shown in Figure 1.1 (Takahashi *et al.*, 1973).

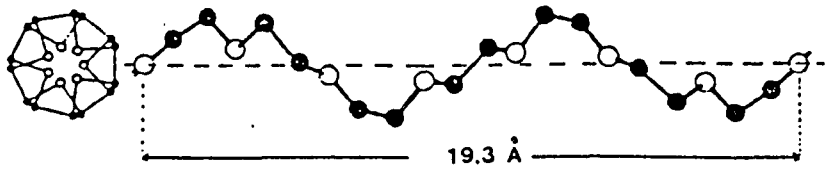

Figure 1.1 The helical structure of PEO from Takahashi *et al.*, 1973.

The melting point of the crystalline phase is 65°C and the glass transition temperature of the amorphous phase is about -60°C. The low glass transition temperature is indicative of good chain flexibility due to unhindered rotation between backbone atoms (Glasse *et al.*, 1987). The polymer is quite stable chemically since it contains only strong unstrained CO, CC and CH bonds. In air, after exposure for several months, peroxide formation and UV (ultraviolet) chain cleavage are responsible for a slow molecular mass decrease.

PEO is an exceptional non-aqueous solvent which dissolves high concentrations of a wide variety of ionic salts to form electrolytes that resemble both solids and liquids. In the context of coordination chemistry PEO can be classified as a member of the "glyme" (glycol methyl ether) series of complexing solvents. These ligands are powerful in two respects. First, the Lewis base strength due to the oxygen is relatively high. Second, the glymes are multidentate, thereby showing a chelate effect. It is then not surprising to find that PEO is sterically favourable for complexation, as compared with other polyethers. PEO tends to form crystalline complexes with a helical structure wrapped around the guest

cations (Parker et al., 1981). The helix repeat distance is considerably reduced from that of the unsalted polymer, showing a strong attraction between the cations and the oxygen on the helix.

Armand (1979) postulated that a helical PEO chain surrounds cations so as to provide a specific pathway for cation transport, while anions are separated from the cations by the polymer chain. Papke and coworkers (Papke, 1981; Papke et al., 1982), from infra-red and Raman spectroscopic studies on the Na and K salt complexes, proposed that PEO chains have a helical conformation with the cation placed inside the helix being coordinated by four polymer oxygen atoms. Wright and coworkers (Parker et al., 1982) reported that PEO chains assume a double-stranded helix and the cations are again placed in the cavity in the KSCN and NaSCN complexes. However, in 1983 Hibma (Hibma, 1983) reported that both cations and anions were found outside deformed helices.

The helical arrangement of the PEO chain in crystalline complexes of lithium trifluoromethanesulphonate with the oxygen to lithium mole ratio of 3:1 has been studied by several groups (Chatani and Okamura, 1987; Chatani et al., 1990 and Lightfoot et al., 1992). They found a significant difference in the inorganic portion of the structure reflecting the effect of the different size of the cation and anion. Li^+ ions were found to be located within the PEO chain. The coordination was described as trigonal bipyrimidal, with the three PEO oxygens being almost coplanar. There is little interchain interaction.

1.3 Poly(ethylene oxide)-based Polymer Electrolytes

Poly(ethylene oxide)-based complexes were the first solvent-free polymer electrolytes to have been reported. Polymer electrolytes are ion conducting polymers, which are solutions of ionic salts such as lithium trifluoromethanesulphonate, more commonly known as lithium triflate ($LiCF_3SO_3$) in "immobile solvents" such as poly(ethylene oxide) (PEO). The ions are deliberately introduced into the polymer structure in a way designed to give a high mobility for ions. The interaction of PEO chains with salts had been recognised since 1951 (Doscher, 1951). The quest for the understanding of the properties of the polymer-salt solutions were soon followed in the 1960's by, for example, Blumberg et al (Blumberg, 1964), Lundberg *et al.*. (Lundberg, 1966), Binks *et al.*. (Binks, 1968) and Yokoyama *et al.*. (Yokoyama, 1969). These studies revealed that the ether oxygen atoms interacted directly with the cations. Although extensive studies had been carried out to recognise the interaction between the polymer and the ionic salts, it was not until the 1970's that a very important physical property that revolutionised the concept of polymer-salt solutions was identified - the ionic conductivity.

The complexes which have received most attention in view of their applicability in practical electrochemical cells are those based on lithium salts such as lithium perchlorate, $LiClO_4$, or lithium trifluoromethanesulphonate, $LiCF_3SO_3$ and PEO. Effectively, both PEO_n:$LiClO_4$ and PEO_n:$LiCF_3SO_3$ complexes, with n around 8, appear suitable for practical applications since they are characterised by an acceptably high level of conductivity which is mostly ionic in nature. The sodium and potassium PEO complexes

were studied by Fenton *et al.* (Fenton *et al.*, 1973) in their pioneering conductivity studies of polymer electrolytes. Armand and co-workers (Armand *et al.*, 1978) have systematically investigated the five alkali metals (Li to Cs) as complexes with PEO. They found that the structural parameters and the interaction energies are determined by the size of the coordinating cation and the type of transformation and the consequent changes in conductivity are dependent on the cation size. The larger, non polarizing Cs^+ leads to a highly conducting amorphous state at room temperature. Rubidium and caesium salt complexes have been studied by Shriver and co-workers (Shriver *et al.*, 1983) and they were reported to be amorphous on account of the large size of the rubidium ion compared with the helix radius. In the studies undertaken by Ito and co-workers (Ito *et al.*, 1986) on $LiCF_3SO_3$ in PEO prepared by an evaporation method, the molecular mass of PEO decreases from 5×10^6 to 200 - 2000 and were partially composed of a disordered structure such as that observed in the molten PEO. They considered that a structure region, different from that of PEO, coexists and attributed the conductivity enhancement to the molten state structure regions. Bouridah and coworkers (Bouridah *et al.*, 1986) suggested a liquid-like behaviour at the microscopic scale in PEO:$LiClO_4$ and PEO:LiI, and the presence of "complex" species.

The effort of relating the observed properties of PEO electrolytes to a structural model (Papke *et al.*, 1982) came from Shriver's group after studying vibrational spectroscopy (Papke *et al.*, 1981), conductivity, thermal characteristics of lithium and sodium electrolytes (Shriver *et al.*, 1981; Papke *et al.*, 1982) and other data (Wong *et al.*, 1981; Dupon *et al.*, 1981 and Dupon *et al.*, 1982). It was deduced that the cations are situated in

a tetrahedral cage of oxygens which are provided by four repeat units of the helical chain in the crystalline region. In the amorphous and interlamellar regions, the four fold situation is retained, but the oxygens may come from other chains.

Since the first proposal by Armand of the technological importance of lithium polymer electrolyte in solid state batteries most of the work on polymer electrolytes centred on the alkali metals especially lithium. It is only ten years later that some attention was given to divalent cations to act as charge carriers in PEO electrolytes. Initially this was on the same pretext of using the electrolyte in solid state batteries. The cation of interest was magnesium as it was seen to be similar in many respects to lithium because of the Li/Mg diagonal relationship in the periodic table, especially for the ionic radii. The lithium/magnesium polymer electrolyte comparison was discussed in detail by Patrick (Patrick, 1986). Complexes of divalent salts and PEO and related polymers had been known for thirty years, the first of which was reported by Blumberg and co-workers (Blumberg *et al.*, 1964). Wissburn and co-workers (Wissburn *et al.*, 1975) found that poly(methyl acrylate) and poly(methyl methacrylate) form complexes with $Ca(NO_3)_2$, $Cd(NO_3)_2$, $Cu(NO_3)_2$ and $Zn(NO_3)_2$. James and coworkers (James *et al.*, 1979) found that divalent halides of Zn, Co, Fe and Cu form single phase amorphous complexes with poly(propylene oxide), PPO. None of these authors reported any studies of ion transport. Studies on calcium and barium were carried out by Fontanella and co-workers (Fontanella *et al.*, 1985) and they found that PEO complexes with $Ca(SCN)_2$ and $Ba(SCN)_2$, giving complexes with high glass transition temperatures and low ionic conductivities. Moryoussef and coworkers (Moryoussef *et al.*, 1985) studied PEO complexes of Ca^{2+} and

found that the ionic conductivities (PEO_{20}:$Ca(CF_3SO_3)_2$ and PEO_{17}:CaI_2) were sufficiently high for application in potentiometric cells. Yang and co-workers (Yang *et al.*, 1986) studied PEO complexes of $MgCl_2$ and $PbBr_2$ and found that some of the complexes exhibit rather high conductivities. For example, the conductivity of PEO_{16}:$MgCl_2$ is comparable to that of PEO_9:$LiCF_3SO_3$ from 80° to 150°C and PEO_8:$PbBr_2$ has a high ionic conductivity at 150°C. Abrantes and co-workers (Abrantes *et al.*, 1986) studied the PEO complexes of $Cu(ClO_4)_2$ and $ZnCl_2$ and found that PEO_8: $Cu(ClO_4)_2$ and PEO_8:$ZnCl_2$ had the highest ionic conductivity of their corresponding series. In 1988 Farrington's group (Huq *et al.*, 1988) reported a variety of PEO electrolytes containing divalent cations, including Cd^{2+}, Ni^{2+}, Co^{2+}, Zn^{2+} and Pb^{2+}. They concluded that divalent cation PEO electrolytes can be categorised into three groups:

1. Compositions that are essentially pure anion conductors which include compositions with small, highly polarizable cations, such as Mg^{2+} and Ca^{2+}, and they are apparently trapped in strong electrostatic bonds with the ether linkages on the polymer chains.
2. Compositions having significant cation transport numbers formed by larger, more polarizable cations such as Pb^{2+} and Cd^{2+}. They form much weaker associations with the polymer chains and are predominantly cation conductors above about 130°C.
3. Electrolytes in which the cation transport numbers appears to be activated by controlled hydration/dehydration. The only example given was PEO_n:$NiBr_2$ which is essentially a pure anion conductor at 120°C but the Ni^{2+} transport number increases at the same temperature after the electrolyte has been purposedly hydrated and dehydrated. This phenomenon was further studied (Huq *et al.*, 1989) using UV-visible absorption

spectroscopy which showed that hydration of PEO_8:$NiBr_2$ results in the formation of $[Ni(H_2O)_6]^{2+}$ ions, and that the complexation of Ni^{2+} by H_2O is much stronger than by PEO.

Bandara and co-workers (Bandara *et al.*, 1995) carried out further studies on PEO_8:$NiBr_2$ and found that the brown dry film obtained after casting the solution in a dry condition contains $NiBr_2$ clusters and uncomplexed PEO rather than PEO_8:$NiBr_2$.

1.4 Interionic and Ion-polymer Interaction in Polymer Electrolytes

The field of polymer electrolytes has advanced both experimentally and conceptually in the past twenty years which has facilitated the development of more specific host structures which give high conductivity along with electrochemical and mechanical stability. Despite these many advances, there is still no well-defined standard model for a polymer electrolyte. Furthermore, there is an incomplete understanding of the role of interionic and ion-polymer interactions, the correlation of motion of the polymer host and ionic species, and the identification of mobile species. A number of techniques have been employed to probe the nature of the environment and transporting species in polymer electrolytes. These include EXAFS (Andrews *et al.*, 1988; Latham *et al.*, 1993), nuclear magnetic resonance (NMR) (Chadwick *et al.*, 1987; Spindler *et al.*, 1988), steady state direct current (dc) polarization techniques (Bruce *et al.*, 1989), conductivity-concentration measurements (MacCallum *et al.*, 1986; Gray 1990) and infrared(IR) and Raman spectroscopy (Papke *et*

al., 1981,1982; Frech *et al.*, 1988; Kakihana *et al.*, 1990, Petersen *et al.*, 1992, Schantz *et al.*, 1988, 1991, 1993).

In polymer electrolytes, the "solvent" is a macromolecular array of Lewis bases of low polarity. These are commonly based on the oxygen atoms of a polyether. Only two types of force are considered to contribute significantly to ion solvation in such systems (MacCallum *et al.*, 1987):

1. general electrostatic interaction, principally the ion-dipole, ion-quadrupole and dipole-dipole forces, and
2. non-electrostatic interactions, including van der Waals' dispersion forces and the energy associated with the formation of strained conformations in the polymer backbone caused by main chain rotations required to accomodate the coordinating groups around the ions.

The term which dominates the energetics of solvation in polymer electrolytes arises from the solvation of the cation. It can occur by simple electrostatic interaction between the positive charge on the ion and the negative end of the solvent dipole, or a partial sharing of a lone pair of electrons leading to the formation of a coordinate bond. Armand (Armand, 1987) identified three parameters that are important for the control of salt/neutral molecule interactions:

a) electron pair donicity, which measures the ability of the solvent to donate electrons to solvate the cation,

b) acceptor number, which quantifies the possibility for anion solvation, and

c) entropy term, which depends on the optimal spatial disposition of the solvating units.

PEO like other ethers are quite strong donors but are very poor acceptors, as they lack hydrogen bonding for anion solvation. PEO has the most favorable spacing, with the CH_2-CH_2-O unit. The formation of a complex corresponds to the competition between solvation energy and lattice energy of the salt. The overall entropy of solution of salts in polymers would generally be positive. In addition to the above Bruce and Vincent (Bruce *et al.*, 1993) considered the distance between coordinating centres also to be important.

1.5 Morphology of Polymer Electrolytes

Polymer electrolytes may be amorphous, crystalline (stoichiometric salt-polymer complexes) or amorphous-crystalline mixtures (crystallisation of the pure polymer host). In the crystalline complexes the cations are always coordinated by a number of the heteroatoms in the polymer chain, whereas the anions themselves have only weak interactions with the polymer. Lightfoot and co-workers (Lightfoot *et al.*, 1992, 1993) in using powder X-ray data succeeded in elucidating the crystal structure of the complex formed between PEO and $NaClO_4$ and $LiCF_3SO_3$ in which the ratio of ether oxygen to salt was 3 : 1 as shown in Figure 1.2.

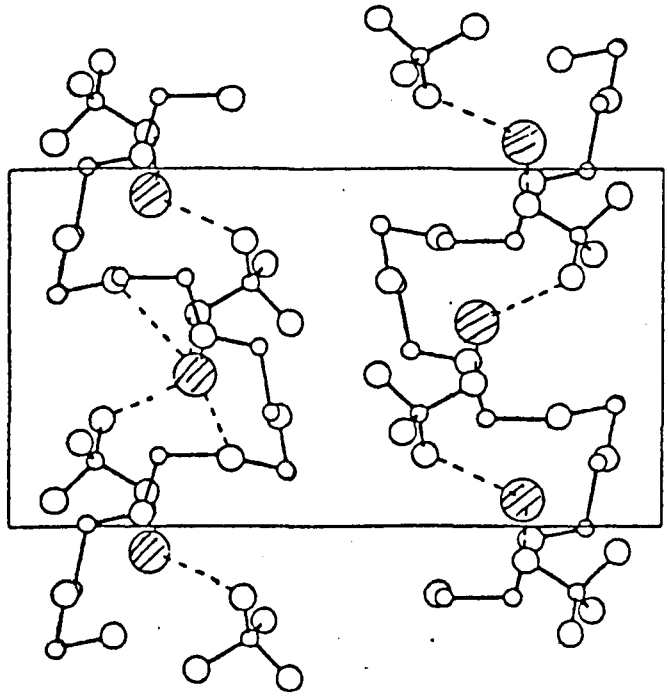

Figure 1.2 Structure of crystalline PEO_3:$NaClO_4$ from Lightfoot et al., 1993. The Na^+ ions (shaded circles) are located within the helices.

Crystallisation of polymer-salt systems is common for PEO electrolytes. Crystallisation takes place by the formation of spherulites (Neat *et al.*, 1986). Spherulites take the form of fibrils which radiate from the centre, branching to fill most of the available space as shown in Figure 1.3.

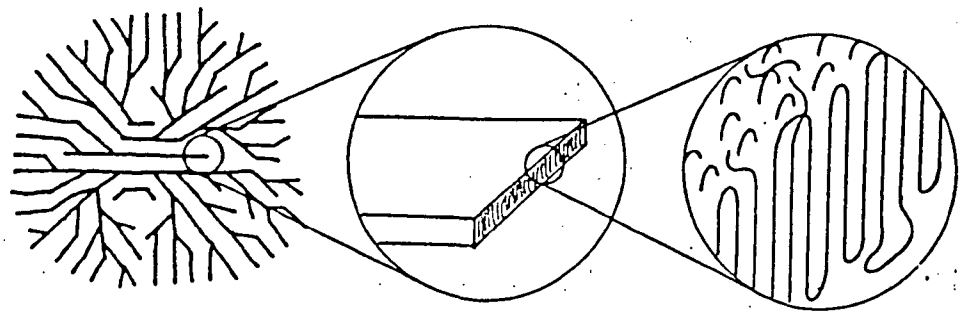

Figure 1.3 Arrangement of polymer chains in a spherulite from Glasse et al., (1987).

Each of the fibrils consists of chains of the polymer backbone arranged in a regular folding manner. Defects in the folding results in misalignment which in turn contribute to amorphicity. Since folding of the long polymer chains cannot form a close packing arrangement, the spaces that result form the amorphous region in addition to the regions in between each spherulites in three dimensions. Although the crystalline component is not important in conductivity terms, it provides sufficient rigidity for these materials to be classified as "solid" electrolytes.

1.6 Ionic Conductivity of Polymer Electrolytes

Since the discovery of solid polymer electrolytes in the 1970's efforts have been concentrated on increasing the bulk ionic conductivity and understanding the mechanism of ion transport across electrolyte films. The earliest mechanism proposed for lithium ion transport in PEO was in fact a standard solid-state vacancy mechanism with lithium ions occupying sites in a regular PEO helix (Armand *et al.*, 1978). A key advance in the understanding of polymer electrolytes was made when it was recognised that significant ionic conductivity was the property of amorphous elastomeric polymer electrolyte phases (Stainer *et al.*, 1982; Berthier *et al.*, 1983). Above the glass transition temperature (T_g) in such phases, polymer molecules have fast internal modes in which bond rotations can produce segmental motion. Ionic mobility is closely associated with these local structural relaxations. The exact relationship between ionic motion and local matrix motion is still not entirely clear, but evidence (Bruce *et al.*, 1993) suggests that for certain charge carriers, the structural relaxations simply provide time dependent pathways or opportunities for ions to move between suitable low-energy sites, whereas for others a mechanism involving short-range transport of ions temporarily attached to the polymer chain is important.

In the case of monovalent cations, the cation-polymer interaction is sufficiently weak or the bond is so labile that such cations are always mobile in polyethers. The strength of a cation-polymer bond may be classified according to the principle of hard and soft acids and bases (Pearson, 1963). Hard bases such as the ethers which have donor atoms with high electronegativity but low polarisability. Cations which act as hard acids usually are small

and not easily polarised, having no unshared electron pairs in their valence shells. In general, the most stable complexes are formed by hard cations coordinated by soft bases. Soft cations such as Hg^{2+} and Pb^{2+} are highly mobile when coordinated to the hard base, PEO (Bruce *et al.*, 1988). Although both cations and anions may be mobile, the conductivities of multivalent cation salts in polymer electrolytes are generally lower than those based on monovalent salts. Thus, while PEO:$Hg(ClO_4)_2$ is the most highly conducting polymer electrolyte based on a divalent cation so far reported (Bruce *et al.*, 1988) this electrolyte exhibits a lower conductivity than that based on $LiClO_4$ at the same molar concentration, despite having a higher charge on the cation and double the concentration of ClO_4^- anions. This suggests that the strength of the ion-ion interactions plays a significant role in lowering the conductivity of a divalent salt compared with a monovalent equivalent (Bruce *et al.*, 1993).

For polymer electrolytes the ionic conductivity is dependent on a number of parameters that influence the concentration and the mobility of the charge carriers such as the molecular mass of the polymer, concentration of added salt and ionic sizes, valency and polarizability of the added anions and cations. A PEO-based polymer electrolyte can be visualised as a polyether-type solvent, containing ethylene oxide units in its backbone in which a salt is dissolved. The important characteristic is that there are ether oxygens in the polymer. The salt dissociates and a "free" ion solvates by coordinating with some, often about four ether oxygen atoms. Polyethers have been shown to be good solvents which contain "free" ions, contact ion pairs and triplets as seen from Raman scattering studies (Stevens *et al.*, 1991). Ion association is an important factor in determining the number

and type of charge carriers taking part in the ionic transport. Many authors have stressed the importance of ion associations for explaining the conductivity behaviour in polymer electrolytes, especially the decrease in conductivity at high salt concentrations (Bannister *et al.*, 1984; Killis *et al.*, 1984; Gorecki *et al.*, 1986). Interchain coordination by an ion might act as a "transient crosslink", shown in Figure 1.4, reducing the overall segmental motion of the polymer host.

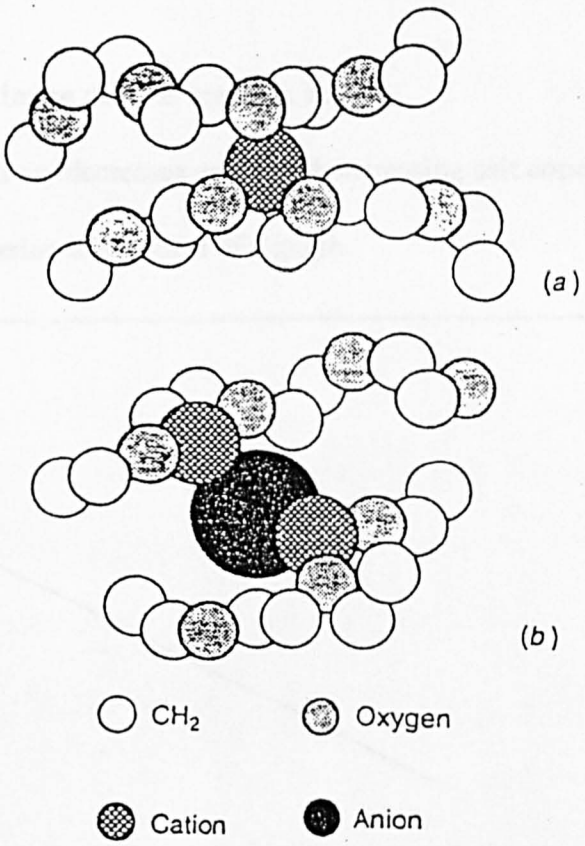

Figure 1.4 Formation of transient crosslinks through (a) a cation and (b) a triple ion (Bruce *et al.*, 1993)

Studies done by Albinsson and co-workers (Albinsson *et al.*, 1992) found that the increase in the ionic conductivity cannot be simply explained by the increasing number of ions that are inserted into the material. Solvent-separated ion pairs, contact ion pairs, triple ions and higher ionic clusters are expected to form as the salt concentration is raised (Bruce *et al.*, 1990,1991). Three regions of conductivity against concentration have been identified:

a) at low salt concentration ion-pairing takes place contributing to the low conductivity values,

b) in the second region a maximum value is reached, and

c) in region three the conductivity decreases again with increasing salt concentration.

Figure 1.5 shows the phenomenon in the form of a graph.

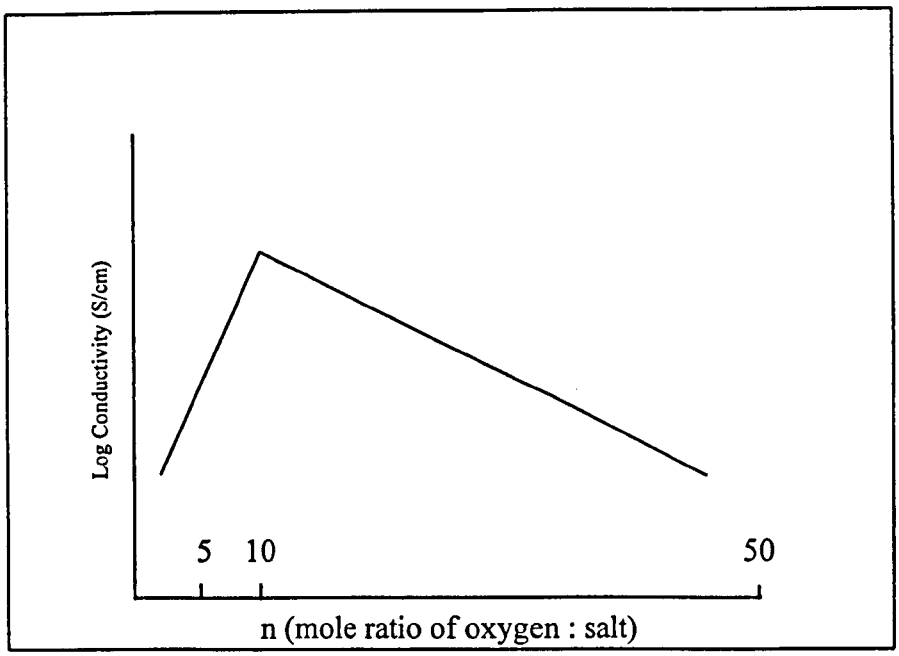

Figure 1.5 The three regions of conductivity in polymer electrolytes.

Two views have been presented to account for the increase in conductivity.

I. Fouss and Kraus (Fouss *et al.*, 1933) suggested that triple ions are formed in region two and this causes the increase in molar conductivity.

II. An alternative interpretation is that redissociation occurs in region two, i.e., the fraction of "free" charge carriers increases with concentration.

Both these views are agreed upon by Cameron and co-workers (Cameron *et al.*, 1988), Gray (Gray, 1991), MacCullum and co-workers (MacCallum *et al.*, 1986), Schantz (Schantz, 1991) and Albinsson and co-workers (Albinsson *et al.*, 1992). However, results from Raman scattering measurements show that redissociation occurs in region two and that the number of triplets is low except at very high salt concentration (Jacobsson *et al.*, 1992).

Most of the research on ion association phenomena in polymer electrolytes has been performed in systems with relatively high contents of salt. Some conductivity data have been obtained for low salt concentrations (below ~ 0.1 mol dm^{-3} or above O:M ~ 80, where O:M is the monomer, i.e, oxygen, repeat unit to salt ratio) and they have been interpreted in terms of triple ion theory (Hall *et al.*, 1986). Thus, the low conductivity observed at very low concentrations has been attributed to the formation of ion pairs and triple ion aggregates.

The Raman spectra of PPO complexed with $LiClO_4$ and $NaCF_3SO_3$ studied by Schantz (Schantz, 1991) revealed the presence of both ion pairs and solvated ions and suggested that single ions rather than charge multiplets are responsible for the conduction at O:M < 20. Raman studies of $LiClO_4$ in PEO by the same group indicated that "free" ions dominate at intermediate concentration O:M ~ 30 (Schantz *et al.*, 1988).

Important questions relating to the conduction mechanism in ionically conducting polymers refer to the type of charge carriers responsible for conduction. Are the dominating carriers single ions, triplets or even higher degrees of multiplets and how are these species affected by parameters such as concentration and temperature? Complexes of MEEP with triflate salts of simple monopositive cations exhibited higher ionic conductivities than the complexes with the salts having dipositive ions and a further reduction of the ionic conductivity is observed for complexes of tripositive metal salts (Blonsky *et al.*, 1986).

The mechanism of ion transport in polymer electrolyte is thought to involve conformation fluctuations of the polymers (Armand *et al.*, 1979; Shriver *et al.*, 1981). This type of transport is reproduced by either a free volume (Armand *et al.*, 1979; Arai *et al.*, 1980) or excess entropy model (Papke *et al.*, 1982) rather than the Arrhenius law. Curvature in the Arrhenius plots interpreted in terms of "association" of the ions with the chains or with each other. In addition, equilibration of a multiphase system must also be considered (Fontanella *et al.*, 1983).

In conductivity studies focus has been given on the temperature dependence of the conductivity. To interpret the variation of the conductivity as a function of temperature, a transport theory based on the free volume Vogel-Tamman-Fulcher (VTF) equation is employed. It can be expressed as the equation below (Armand *et al.*, 1979);

$$\sigma = AT^{-1/2} \exp [-E_a/(T-T_o)] \qquad (1.1)$$

In this equation T_o represents the glass transition temperature, A is proportional to the concentration of charge carriers and to the geometric factor and E_a is an apparent activation energy.

In this model, suitable for concentrated liquid solutions, fused salts and amorphous PEO alkali metal complex salts (Lampreia *et al.*, 1976; Angell, 1964), the diffusion of ions depends on disordered local movements in the material. The glass transition temperature of the polymer and polymer-salt complexes are a function of reorientational mobility of the backbone and side-groups.

The VTF equation can be derived from the viscoelastic properties of the amorphous phase of the polymer electrolytes. The viscosity properties of supercooled liquids could be described by an empirical relationship for the viscosity in the form

$$\eta = C \exp [+B/(T-T_o)] \qquad (1.2)$$

Applying the Stokes-Einstein relationship for diffusion

$$D = kT/6\pi r_i\eta \tag{1.3}$$

where k is the Boltzmann's constant and r_i is the radius for diffusion.

$$D = (kT/6\pi r_i) \times (1/C \exp[+B/(T-T_o)]) \tag{1.4}$$

Now, using the Nernst-Einstein relationship for conductivity

$$\sigma = nq^2D/kT \tag{1.5}$$

where n is the carrier concentration and q the carrier charge.

$$\sigma = (nq^2/6\pi r_i) \times (1/C \exp[+B/(T-T_o)]) \tag{1.6}$$

$$= (nq^2/6\pi r_iC) \exp[-B/(T-T_o)]$$

$$= \sigma_o \exp[-B/(T-T_o)] \tag{1.7}$$

where $\sigma_o = nq^2/6\pi r_iC$ and C is proportional to $T^{1/2}$.

2.0 Introduction

This chapter discusses the underlying principles of the techniques involved in the studies. The techniques employed in this study are impedance spectroscopy (IS), X-ray absorption spectroscopy (extended X-ray absorption fine structure, EXAFS, and X-ray absorption near edge structure, XANES), differential scanning calorimetry (DSC) and variable temperature polarising microscopy (VTPM).

2.1 Alternating Current (AC) Impedance Spectroscopy

Impedance spectroscopy (IS) is a powerful method of characterising many of the electrical properties of materials and their interfaces with electronically conducting electrodes. It was first applied to analyse the response of solid electrochemical cells to sinusoidal perturbation by Bauerle (1969). IS is characterised by the measurement and analysis of some of impedance-related functions Z (impedance), Y (admittance), M (modulus) and ε (permitivity) and plotting of these functions in the complex plane. It is becoming a popular analytical tool in materials research and development because it involves a relatively simple electrical measurement that can readily be automated and whose results may often be correlated with many complex materials variables; from mass transport, rates of

chemical reactions, corrosion, and dielectric properties, to defects, microstructure, and compositional influences on the conductance of solids. It may be used to investigate the dynamics of bound or mobile charge in the bulk or interfacial regions of any kind of solid or liquid material.

2.1.1 The Essence of Impedance Spectroscopy

Generally, in an IS experiment an electrical stimulus is applied to the electrodes and the response, the resulting current or voltage, is observed. A multitude of fundamental microscopic processes take place throughout the cell when it is electrically stimulated leading to the overall electrical response, including the transport of electrons through the electronic conductors, the transfer of electrons at the electrode-electrolyte interfaces to or from charged or uncharged atomic species which originate from the cell materials and its atmospheric environment, and the flow of charged ions or charged clusters via defects in the electrolytes. The flowrate of charged particles depends on the ohmic resistance of the electrodes and the electrolyte and on the reaction rates at the electrode-electrolyte interfaces and may be further impeded by band structure anomalies at any grain boundaries present and by point defects in the bulk of all materials (MacDonald, J.R. and Johnson, W.B., 1987).

The most common and standard approach is to measure directly in the frequency domain by applying a single-frequency voltage to the interface and measuring the phase shift and

amplitude (real and imaginary parts) of the resulting current at that frequency. Any intrinsic property that influences the conductivity of an electrode materials system can be studied by IS. The parameters derived from an IS spectrum can fall into one of two general categories:

a) techniques related only to the material itself, such as conductivity, mobilities of charges and dielectric constant; and
b) techniques pertinent to an electrode-material interface, such as adsorption-reaction rate constants and diffusion coefficient of the neutral species in the electrode itself.

Experimentally obtained impedance data for a given electrode-materials system may be analysed by using an exact mathematical model based on a plausible physical theory that predicts theoretical impedance or by a relatively empirical equivalent circuit. In either case the parameters can be estimated and the experimental data compared to the theoretical impedance or to the predicted equivalent circuit impedance. An analysis of the charge transport processes likely to be present in an experimental cell will often suggest an equivalent circuit of ideal resistors and capacitors and may account adequately for the observed IS response.

2.1.2 Principles of Impedance Spectra

The most popular approach to the determination of the electrical properties of polymer electrolyte is the alternating current (a.c) method. The popularity is because:

1. the cell assembly incorporating either inert blocking electrodes or non-blocking electrodes is simple, and
2. the data carry information not only about the long-range migration of ions but also about polarisation phenomenon occurring within the cell.

In an a.c experiment a sinusoidal voltage is applied to a cell and the sinusoidal current passing through the cell as a result of this perturbation is determined. Two parameters are required to relate the current flowing to the applied potential. One represents the opposition to the flow of charge and is equal to the ratio of the voltage and current maxima, V_{max}/I_{max}, and is analogous to the resistance in direct current (d.c) measurements. The other parameter is the phase shift, ϕ, of the voltage and current. The combination of these parameters represents the impedance, Z, of the cell. For an electrochemical cell, both the magnitude of the impedance, Z, and its phase angle, ϕ, are functions of the applied frequency. The impedance contains four main contributions; these are from resistance, capacitance, constant phase elements (cpe) and inductance. Inductance is unimportant for polymer electrolytes (Linford, 1989). In a.c theory the voltage, V, varies sinusoidally. At any given time, t, this is related to the amplitude of the voltage, V_o, by

$$V = V_o(\cos[\omega t] + \sin[\omega t])$$

For a pure resistor obeying Ohm's law the current is in phase with the voltage. For a pure capacitor the current leads the voltage by 90^{o} and for an inductor the current lags behind the voltage by 90^{o}. The cpe is a hybrid somewhere between a resistor and a capacitor.

The a.c method of interest involves measuring the impedance as a function of the frequency of the applied signal over a wide frequency range. Since impedance is a vector quantity it may be represented as a point on a vector diagram. The impedance for each frequency measured is represented by a separate point on a vector diagram. The distance of the point from the origin corresponds to the magnitude of the impedance and the angle formed with the x-axis corresponds to the phase difference between the voltage and current. The impedance may be represented in terms of the real and imaginary parts of a complex number $Z^* = Z' - jZ''$ where j represents the complex number operator $\sqrt{-1}$.

The problem in an a.c experiment is to interpret the complex impedance plot in terms of the electrical processes occurring in the cell. In general, the response of a cell to an a.c signal can be represented by an equivalent electrical circuit consisting of components, such as resistors and capacitors, which individually represent charge migration and polarisation occurring within the cell. Interpreting the results of an a.c. experiment relies on finding the equivalent circuit which models the impedance data and extracting values for the individual components which may then be related to the fundamental electrical properties of the cell. Equivalent circuits are always an approximation but of great value.

The resistor and capacitor are the most common components required for the modelling of electrochemical cells. If a resistor and a capacitor is connected in series as in Figure 2.1a, the total impedance is

$$Z^*_{tot} = R - j/\omega C$$

In the complex impedance plane this defines a vertical spike displaced a distance R along the real axis. As the frequency is increased the impedance of the capacitor is reduced and hence the contribution of the imaginary component to the impedance falls.

When the components are connected in parallel, the total impedance is

$$Z^*_{tot} = (1/R + j\omega C)^{-1}$$

$$= \frac{R - j\omega CR^2}{1 + (\omega CR)^2}$$

$$= R[1/(1 + (\omega CR)^2)] - jR[(\omega RC)/(1 + (\omega RC)^2]$$

This defines a semicircle in the complex impedance plane with a diameter R extending along the real axis from the origin as in Figure 2.1b.

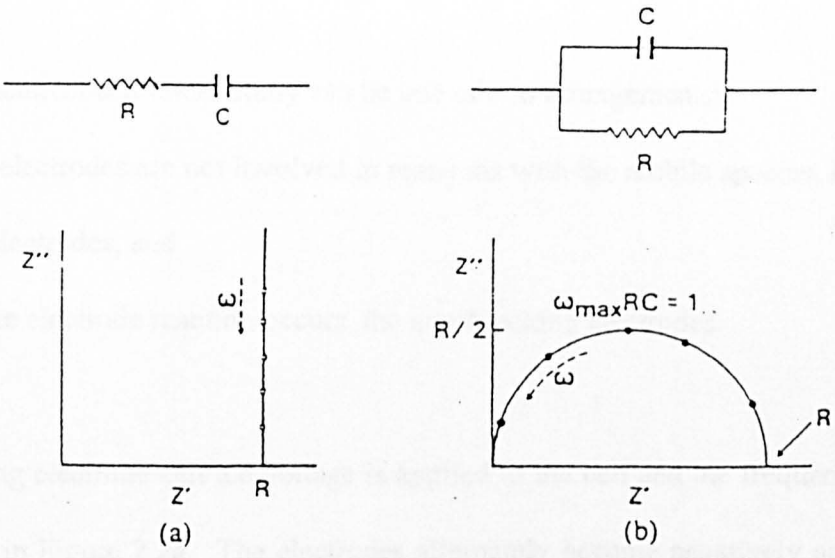

Figure 2.1 Complex impedance plots for a combination of a resistor, *R*, and capacitor, *C*, (a) in series and (b) in parallel.

At the frequency corresponding to the maximum of the semicircle, ω_{max}, the magnitude of the impedance of the resistor and capacitor are equal;

$$R = 1/\omega_{max} C$$

Thus, $\omega_{max} CR = 1$

The position of any such semicircle in the frequency spectrum depends therefore on the *RC* product for the circuit. By following the same rules the electrical response of any network of components may be obtained.

2.1.3 The A.C Response of Cells Containing Polymer Electrolytes

The electrochemical cell under study can be one of two arrangements;

1. where the electrodes are not involved in reactions with the mobile species, known as the blocking electrodes, and
2. where finite electrode reaction occurs, the non-blocking electrodes.

In the blocking electrode cell a.c voltage is applied to the cell and the frequency is varied, as illustrated in Figure 2.2a. The electrodes alternately become negatively and positively charged and the alternating field across the electrolyte causes the ions to migrate back and forth in phase with the voltage. The migration of the ions is represented by the resistor R_b in Figure 2.2b. At the same time the immobile polymer chains become polarised in the alternating field and this dielectric polarisation may be represented by a capacitor C_b.

As the ions move in the alternating field they are alternately accumulated and depleted at each electrode. On each half-cycle, ionic charge builds up within the electrolyte near the electrodes. These charges being balanced by an equal and opposite electronic charge on the electrodes themselves. Each electrode is somewhat similar to a parallel plate capacitor and may be represented by capacitance C_e. The electrode/electrolyte interface can be represented as a double-layer capacitance.

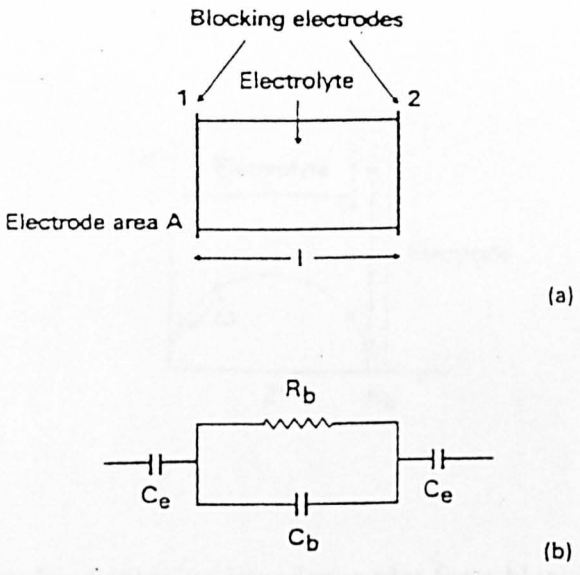

Figure 2.2 Schematic representation of (a) a blocking electrode cell and (b) the equivalent circuit.

The bulk polarisation and ionic migration are physically in parallel and their representative components, R_b and C_b, are connected in parallel; both are in series with the electrode capacitance, C_e. The equivalent circuit constructed, C_e in series with the parallel combination of R_b and C_b, gives a total impedance of

$$Z^*_{tot} = R_b\,[1/(1 + (\omega C_b R_b)^2)] - j(R_b\,[(\omega R_b C_b)/(1 + (\omega R_b C_b)^2] + 2/\omega C_e)$$

This equation predicts a complex impedance plot as shown in Figure 2.3.

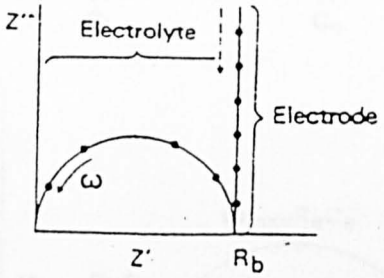

Figure 2.3 Simulated complex impedance plot for a blocking electrode cell.

At high frequencies when the impedance of the bulk resistance and capacitance are of the same magnitude, both the bulk resistance and capacitance contribute significantly to the overall impedance whereas the impedance of the electrode capacitance is insignificant. Thus at high frequencies the equivalent circuit reduces to a parallel R_bC_b combination giving rise to a semicircle in the complex impedance plane. At low frequencies C_b makes a negligible contribution to the impedance and the equivalent circuit thus reduces to a series combination of R_b and C_e appearing as a vertical spike displaced at distance R_b along the real axis.

In non-blocking electrode arrangement finite electrode reaction takes. The appropriate equivalent circuit is illustrated in Figure 2.4.

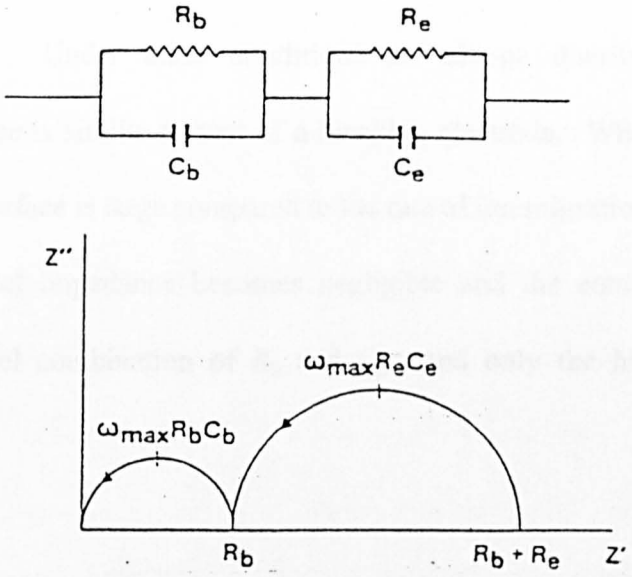

Figure 2.4 Equivalent circuit and complex impedance plot for electrolyte having one mobile ion with non-blocking electrode.

In electrolytes where the cation is the only mobile charge carrier the a.c response is represented by a parallel combination of the bulk resistance and capacitance, R_b and C_b. This gives rise to the high-frequency semicircle in the complex impedance plane. The a.c response of the electrode/electrolyte interface is represented by the parallel combination of R_e and C_e, C_e represents charging and discharging of the double layer, in this case by those ions which do not react at the interface on each half-cycle. R_e represents the electrode reaction at the interface.

The finite rate of the electrode reaction is reflected in the magnitude of R_e ; if R_e is larger (slow electrode reaction) then only a small proportion of the ions at the electrode take part in the electrode reaction. Under these conditions the charge distribution at the electrode/electrolyte interface is similar to that of a blocking electrode. When the rate of ion migration across the interface is large compared to the rate of ion migration to and from it; then the entire interfacial impedance becomes negligible and the equivalent circuit reduces to that of a parallel combination of R_b and C_b , and only the high-frequency semicircle remains.

In the case where there are more than one mobile ions which are non-blocking, generally three approximately semicircular regions may be anticipated as illustrated in Figure 2.5.

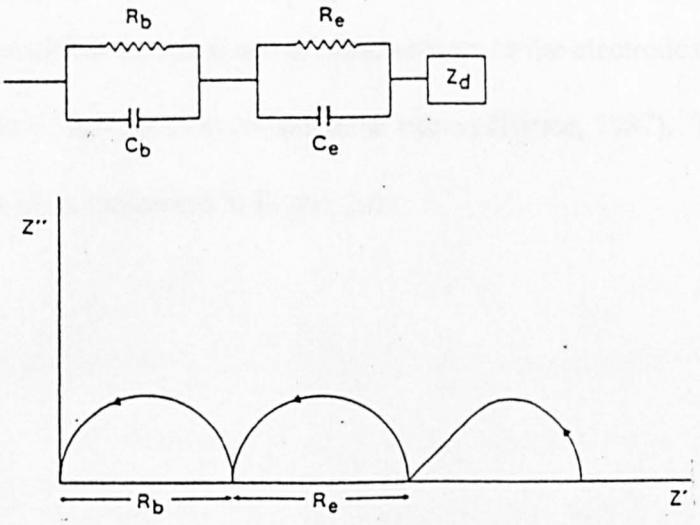

Figure 2.5 Equivalent and complex impedance plot for electrolyte having more than one mobile ions with electrode which is non-blocking to cation only.

The low-frequency semicircle is skewed, exhibiting a linear region at high frequencies which is inclined at an angle of 45° to the real axis. All three features may not be observed in every case. The high-frequency semicircle is associated with the bulk electrolyte response just as in the case of a blocking electrode cell. This semicircle corresponds to the parallel combination, R_bC_b , in the equivalent circuit. The second semicircle at the intermediate frequencies, corresponds to the parallel combination, R_eC_e , in the equivalent circuit; C_e associated with the charging and discharging of the electrode/electrolyte interface, whereas R_e arises from the reaction of the electroactive ions. The lowest-frequency semicircle has been attributed to diffusion arising from the presence of concentration gradients within the electrolyte. It is represented by Z_d in the equivalent circuit, and is called a Warburg impedance.

Similar diffusion-controlled impedance can arise if an ionically conducting polymer contains more than one mobile species, one of which reacts at the electrodes while at least one of the other inert ionic species is in considerable excess (Bruce, 1987). The equivalent circuit for such a situation is illustrated in Figure 2.6

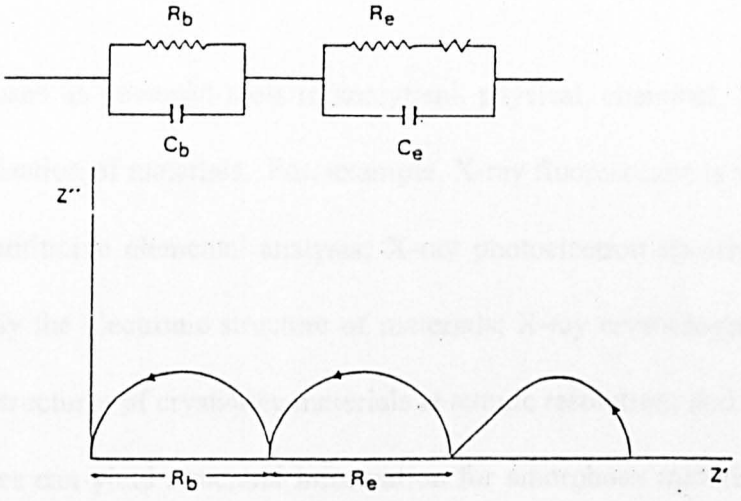

Figure 2.6 Equivalent circuit and complex impedance plane plot for a polymer electrolyte cell exhibiting diffusion-controlled migration of an electoactive ion.

The electroactive ions in this case are transported to and from the electrodes by diffusion with no assistance from the electric field. The diffusion of the electroactive ions is represented by the Warburg element, *W*. The Warburg impedance gives rise to a straight line inclined at an angle of 45° to the real axis. Warburg impedances can only arise when there is diffusion-controlled transport of the electroactive species either within the electrolyte or within the electrode.

2.2 X-ray Absorption Fine Structures (XAFS)

2.2.1 X-rays

X-rays have been used as powerful tools in analytical, physical, chemical, biological and structural characterisation of materials. For, example, X-ray fluorescence is widely used in qualitative and quantitative elemental analysis; X-ray photoelectron spectroscopy (XPS) can be used to study the electronic structure of materials; X-ray crystallography provides three dimensional structures of crystalline materials at atomic resolution; and various X-ray scattering techniques can yield structural information for amorphous materials at varying degrees of resolution.

X-rays are electromagnetic radiation characterised by the relatively short wavelengths of 0.01 Å to 100 Å (1 Å = 1 x 10^{-10}m), with hard X-rays on one end and soft X-rays on the other. They are conventionally produced by either the conversion of the kinetic energy of charged particles into radiation which produces a continuous spectrum or the excitation of atoms in a target upon which fast moving electrons impinge producing characteristic lines of monochromatic X-rays. Discrete characteristic lines are widely used in X-ray diffraction studies while continuous X-ray spectra may be utilised in EXAFS measurements. The continuous radiation suffers from being a thousand times weaker in intensity than the characteristic lines.

For EXAFS measurement purposes synchrotron radiation needs to be employed to provide the required intensity. It is emitted when charged particles such as electrons travel with a speed approaching that of light in curved paths in a magnetic field. The advantages of synchrotron radiation are (Winick, 1980):

- high intensity
- tunability
- high collimation
- small source-spot size
- broad spectral range

An absorption spectrum is obtained when the electron in an occupied level is excited to an occupied bound state by absorption of a photon. If the electron is excited from a core state to continuum, an X-ray absorption edge results. The minimum photon energy required to eject an electron out of a particular atomic state is called the threshold energy, E_o, which is equal to the value of the binding energy of the electron. In the notation of Sommerfeld, the absorption edges are labelled, in the order of increasing energy, by K, L_I, L_{II}, L_{III}, etc., corresponding to the excitation of an electron from the 1s ($^2S_{1/2}$), 2s ($^2S_{1/2}$), 2p ($^2P_{1/2}$), 2p ($^2P_{3/2}$), orbitals (states), respectively.

X-rays interact with matter in a number of distinctly different ways. The interactions involve excitation of, or scattering by, the medium. In the case of X-ray photoionization, a photoelectron is ejected from a core level after absorbing a photon. The excited electron can then relax through several mechanisms giving rise to fluorescence X-rays or non-radiative electrons. The process are depicted schematically in Figure 2.7.

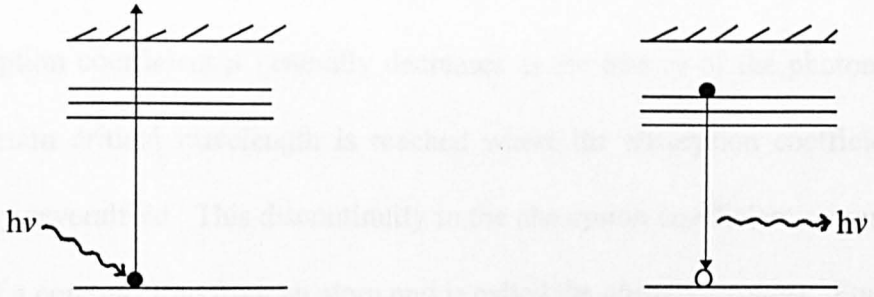

Figure 2.7. Interactions of photons with the core levels of an atom emitting fluorescent photons.

When a collimated beam of monochromatic X-rays travels through matter, it loses its intensity via interaction with the material. The loss in intensity, I, is proportional to the original intensity and the thickness x:

$$dI = -\mu I dx \qquad (2.1)$$

with the proportionality constant μ being the linear absorption coefficient. On integration equation (2.1) gives rise to

$$I/I_o = e^{-\mu x} \qquad (2.2)$$

where I_o and I are the incident and the transmitted X-ray intensities and x is the thickness of the sample.

The absorption coefficient μ generally decreases as the energy of the photon is increased until a certain critical wavelength is reached where the absorption coefficient increases abruptly by severalfold. This discontinuity in the absorption coefficient corresponds to the ejection of a core electron from an atom and is called the *absorption edge*. Further increase in energy causes a similar decrease in μ, but at a somewhat different rate, until another absorption edge is reached.

Transmission is just one of several modes of XAFS measurements. The fluorescence technique involves the measurement of the fluorescence radiation at right angles to the incident beam. For dilute systems, this method removes the 'background' absorption due to other constituents, thereby improving the sensitivity by orders of magnitude. In the transmission or fluorescence mode, XAFS spectroscopy involves only X-ray measurements.

2.2.2 Extended X-ray Absorption Fine Structures (EXAFS)

EXAFS refers to the oscillatory variation of the X-ray absorption as a function of photon energy beyond an absorption edge. The absorption, normally expressed in terms of absorption coefficient (μ), can be determined from a measurement of the attenuation of X-rays upon their passage through a material. When the X-ray photon energy is tuned to the binding energy of some core level of an atom in the material, an abrupt increase in the absorption coefficient, the absorption edge, occurs. For atoms, either in a molecule or embedded in a condensed phase, the variation of absorption coefficient at energies above the absorption edge displays a fine structure called EXAFS. Such fine structures may extend up to 1000 eV above the absorption edge. EXAFS spectra generally refer to the region 40 - 1000 eV above the absorption edge.

Although the fine structure has been known for a long time (Kronig, 1931, 1932), its structural content was not fully recognised until the work of Stern, Sayers and Lytle (1974, 1975). In addition, the availability of synchrotron radiation has resulted in the establishment of EXAFS as a practical structural tool particularly through the work of Eisenberger and Kincaid, (1975). This technique is especially valuable for structural analyses of chemical (e.g., Steel *et al.*, 1985; Barrett *et al.*, 1989 and Pizzini *et al.*, 1993) or biological systems (e.g., Harries *et al.*, 1986 and Abrahams *et al.*, 1986) where conventional methods are not applicable.

2.2.2.1 Theory

EXAFS is a final state interference effect involving scattering of the outgoing photoelectron from the neighbouring atoms. The probability that an X-ray photon will be absorbed by a core electron depends on both the initial and the final states of the electron. The initial state is the localised core level corresponding to the absorption edge. The final state is that of the ejected photoelectron which can be represented as an outgoing spherical wave originating from the X-ray absorbing atom. If the absorbing atom has a neighbouring atom, the outgoing photoelectron wave will be backscattered by the neighbouring atom, producing an incoming electron wave. The final state is then the sum of the outgoing and all the incoming waves, one from each neighbouring atom. It is the interference between the outgoing and the incoming waves that gives rise to the sinusoidal variation of μ versus E known as EXAFS. This phenomenon is conveyed pictorially in Figure 2.8.

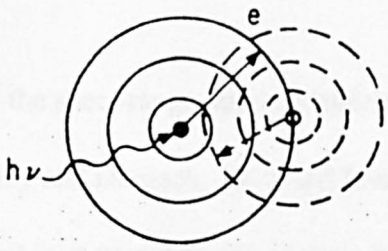

Figure 2.8 Qualitative rationalisation of EXAFS in a one neighbour environment.

A photoelectron ejected by absorption of an X-ray photon will travel as a spherical wave with a wavelength of

$$\lambda = 2\pi/k$$

where k is the photoelectron wavevector defined as

$$k = [2m/h^2 (E - E_o)]^{1/2} \qquad (2.3)$$

where E is the incident photon energy and E_o is the threshold energy of that particular absorption edge. The outgoing photoelectron can be backscattered from the neighbouring atoms producing an incoming wave which can interfere either constructively or destructively with the outgoing wave near the origin, resulting in the oscillatory behaviour of the absorption rate. The amplitude and frequency of this sinusoidal modulation of μ versus E depends on the type of the neighbouring atoms and their distances away from the absorber.

This view has been formulated into the short-range single scattering theory (Stern, 1974; Stern, Sayers and Lytle, 1975; Ashley and Doniach, 1975 and Lee and Pendry, 1975). For reasonably high energy (> 50eV) and moderate thermal or static disorders, the modulation of the absorption rate in EXAFS, normalised to the background (μ_0) is given by

$$\chi(E) = \frac{\mu(E) - \mu_0(E)}{\mu_0(E)} \qquad (2.4)$$

In order to relate $\chi(E)$ to structural parameters it is necessary to convert the energy E into the photoelectron wavevector k via equation (2.3). This transformation of $\chi(E)$ in E space gives rise to $\chi(k)$ in k space where

$$\chi(k) = \sum_j N_j S_i(k) F_j(k) \exp(-2\sigma j^2 k^2) \exp(-2r_j/\nu_j(k)) \frac{\sin(2kr_j + \phi_{ij}(k))}{kr_j^2} \qquad (2.5)$$

Equation (2.5) shows the structural basis of EXAFS in that $\chi(k)$ is dependent on the number of scattering atoms N_j, the location of the scattering atoms r_j and on the type of scattering atom through the characteristic energy dependence of the backscattering amplitude function F_j.

ν is the elastic mean free path of the photoelectron and it is the damping term ($\exp(-2r_j/\nu_j(k))$ which limits the backscattering contribution to approximately 4Å from the absorber ion. This is in part responsible for the short-range description of the EXAFS phenomenon.

$S_i(k)$ is the amplitude reduction factor due to many-body effects at the central atom i.

The Debye-Waller term, $\exp(-2\sigma_j^2 k^2)$, is a measure of the thermal and static displacements within each shell where σ_j, the Debye-Waller factor, is defined as the variance in distance between the atoms in shell j and the excited atom. It has the dimensions of area. Photoionisation takes place on a time scale that is very short relative to atomic motions. Thus, the effects of thermal vibration and static disorder, which will have the effect of reducing the EXAFS amplitude, has to be considered. In general, failure to consider the

effects of thermal vibration and static disorder can result in large errors in the determination of coordination numbers and interatomic distances (Eisenberger *et al.*, 1979; Hayes *et al.* 1978).

The last term is the sinusoidal oscillation which is a function of interatomic distances between the absorber and scatterer ($2kr_j$) and the phase shift between the outgoing and backscattered waves ($\phi_{ij}(k)$). The sinusoidal EXAFS oscillation is caused by the interference sin ($2kr$) term with a frequency $2r$ in k space. The larger the distance r, the more rapid will be the oscillation, the higher the frequency. Distance r also reduces the EXAFS amplitude by $1/r^2$ which implies that the larger the distance, the weaker will be the EXAFS signal.

Structural determination via EXAFS depends on the feasibility of resolving the data into individual waves corresponding to the different types of neighbours of the absorbing atom. This can be accomplished by the Fourier transform technique. It provides a photoelectron scattering profile as a function of the radial distance for the absorber. In such a radial distribution function, the positions of the peaks are related to the distance between the absorber and the neighbouring atoms while the sizes of the peaks are related to the numbers and types of the neighbouring atoms.

The single-electron single-scattering theory of EXAFS makes use of the fact that in most cases multiple scattering is not important. This assumption is generally valid; it considers that multiple scattering processes can be accounted for by adding all scattering paths that

originate and terminate at the central atom. The rapidly oscillatory waves that resulted tend to cancel out.

2.2.2.2 Data Analysis

The purpose of analysing EXAFS data is to be able to extract information related to interatomic distances, numbers and types of backscattering neighbours. There are a number of steps involved in the data analysis. These include:

1. Background subtraction and normalisation
2. Conversion to wave-vector form
3. k weighting
4. Fourier transforming
5. Fitting for phase
6. Fitting for amplitude

1. Background Subtraction and Normalisation

The first step in the analysis is the background subtraction. This consists of separating the modulation in the absorption coefficient from the smooth atom-like absorption. It is usually assumed that the smooth part of μ (E) at energies well beyond the absorption edge

is a good approximation to μ_0 (E). The observed EXAFS oscillations are normalised by normalising the data to the edge jump intensity.

2. Conversion to Wave-Vector Form

The EXAFS must be expressed in terms of wave vector k in order to extract structural information. This requires a value for the threshold energy, E_o. The choice is important because of its effect on the phase of the EXAFS oscillations.

3. k Weighting

Once the data has been transformed to wave-vector form, it is multiplied by some power of k; typically k^3 . Such a factor cancels the $1/k$ factor in equation (2.5) as well as the $1/k^2$ dependence of the backscattering amplitude at large values of k. k weighing is important because it prevents the large amplitude oscillations (typically present at low k) from dominating over the small ones (typically at high k). This is critical since the determination of interatomic distances depends on the frequency and not the amplitude of the oscillations.

4. Fourier Transforming

EXAFS formulation in wave vector form consists of a sum of oscillations with phase and amplitude. A Fourier transform of the EXAFS from wave vector form yields a function

that is similar to a radial distribution function which exhibits peaks that correspond to interatomic distances between the central atom and the individual coordination shells.

5. Phase Fitting

Accurate distance determinations depend critically on the accurate determination of phase shifts. The more commonly employed approach is based on the use of model compounds and the concept of phase transferability. This approach consists of employing a compound of known structure that has the same absorber/backscatterer combination as that of the material of interest. The EXAFS spectrum of the known compound is obtained and the oscillatory part of the EXAFS is fitted. Since r is known in this case, the phase shift can be determined. This phase shift, from the phase transferability concept (Abruna, 1990), can be transferred to any compound with the same combination of atoms without regard to chemical effects such as ionicity or covalency of the bonds involved. This was conclusively demonstrated by Citrin and co-workers (Citrin *et al.*, 1976) in a study of germanium compounds. With good quality data and appropriately determined phase shifts, distances determined by EXAFS are typically good to ± 0.01 Å.

6. Amplitude Fitting

Fitting for amplitude is employed in order to determine the types and numbers of backscattering atoms around a given absorber. The amplitude of the EXAFS of an unknown material has to be compared to that of a compound of known coordination

number and structure. Since there are differences in the structure and coordination between the model compound and the unknown material, the approximation is not as accurate as the phase fitting and as a result, determination of coordination numbers is usually no better than ± 20 %.

2.2.3 X-ray Absorption Near Edge Structure (XANES)

The near edge structure in an absorption spectrum covers the range between the threshold and the point at which the EXAFS begins. Its limits are in principle different for each system, but it is normally considered that XANES extends to an energy of the order of 50 eV above the edge. Bianconi (1980) suggested that the energy dividing the XANES and the EXAFS is roughly that at which the wavelength of the excited electron is equal to the distance between the absorbing atom and its nearest neighbours. The general features of the edge region are the existence of one or more distinct absorption lines in the range -20 eV to 0 eV, corresponding to the electronic transitions from the inner occupied orbitals to outer unoccupied orbitals and the continuum. These peaks are closely spaced which are typically only a few eV apart. The energies and intensities of these transitions are sensitive to the coordination state of the probed atom. It is then followed by a discontinuous rise in cross-section at the continuum edge, followed by a series of fairly narrow resonant peaks in the range 0 to 30 eV as depicted schematically in Figure 2.9.

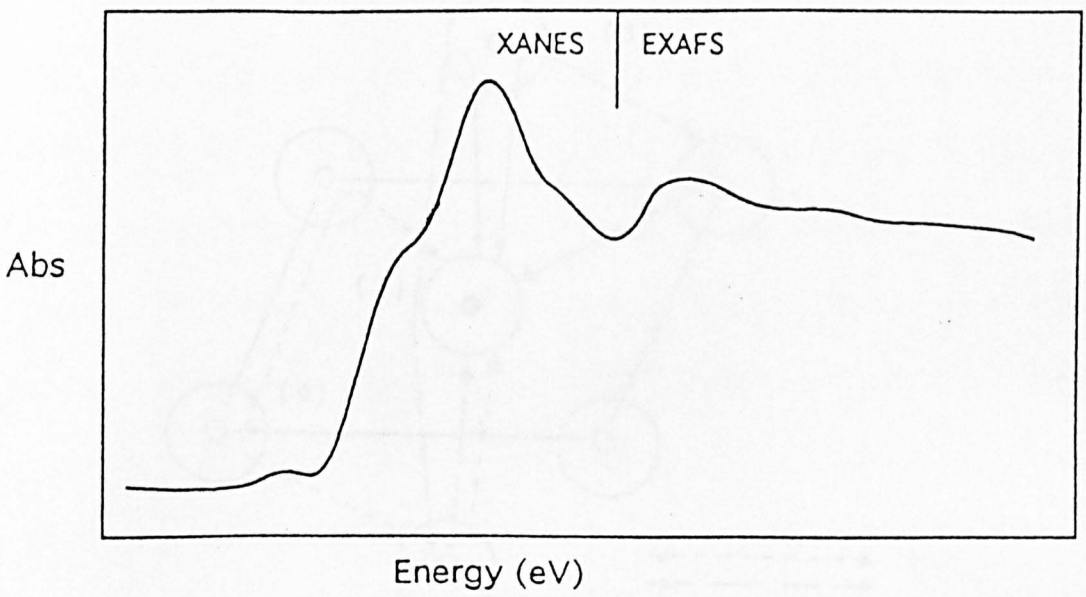

Figure 2.9. The near edge structure window of the absorption spectra.

XANES is determined by the atomic geometrical arrangements in a local cluster around the absorbing atom via the multiple scattering of the excited photoelectron. Multiple scattering in XANES gives the higher order atomic correlation functions while the single scattering in EXAFS gives only the first order pair correlation function. In the photoionization process

the low kinetic energy (10 - 40 eV) excited photoelectron is strongly backscattered by neighbouring atoms, generating multiple scattering processes as shown in Figure 2.10.

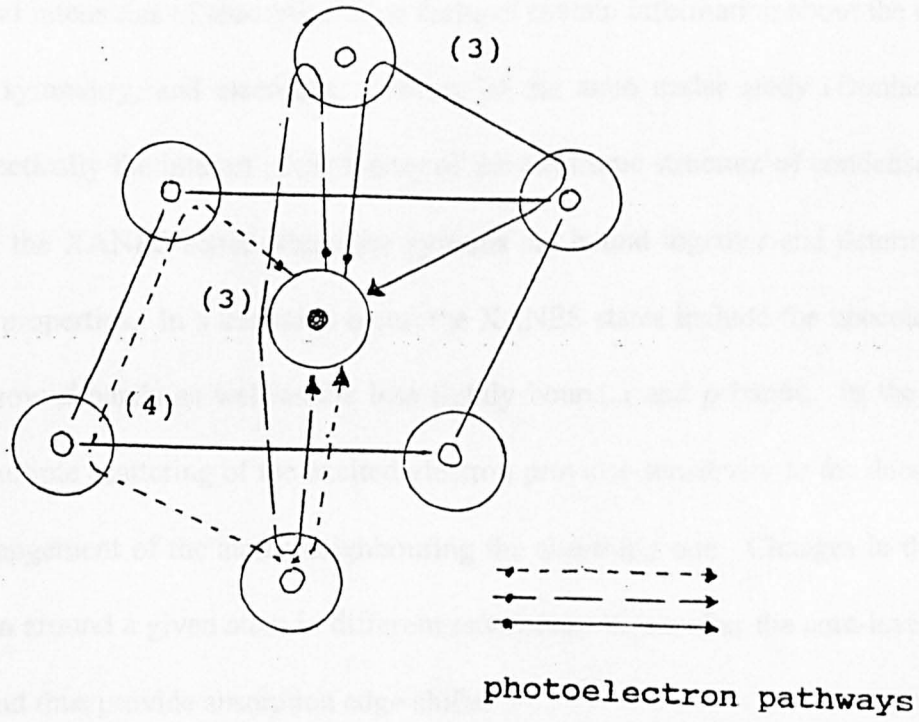

Figure 2.10. Pictorial view of photoelectron scattering processes in the multiple scattering regime of XANES.

It is because of this multiple scattering involving several atoms that XANES is informative about the relative positions of the neighbouring atoms. The multiple scattering pathways can be classified according to the number of scattering events (*n*). Moreover *n* indicates

the order of correlation functions probed by the absorption. However, because of inelastic scattering the contribution of the longest pathways is reduced.

XANES contains information such as the relationship between the shift of the core-level binding energies in different chemical environments (Williams and Lang, 1978). The position and intensities of absorption edge features contain information about the oxidation state, site symmetry, and electronic structure of the atom under study (Doniach *et al.*, 1980). Practically the interest in the theory of the electronic structure of condensed matter centres on the XANES states where the systems are bound together and determine their electronic properties. In a transition metal the XANES states include the unoccupied part of the narrow *d* bands as well as the less tightly bound *s* and *p* bands. In the XANES regime, multiple scattering of the excited electron provides sensitivity to the details of the spatial arrangement of the atoms neighbouring the absorbing one. Changes in the charge distribution around a given atom in different environments can alter the core-level binding energies and thus provide absorption edge shifts.

In the region of the absorption edge, fine structure with inner shell transitions which correspond to electronic transitions from inner occupied orbitals to outer unoccupied orbitals is often seen, e.g. a pre edge due to $1s$ -----> $3d$ transitions, a shoulder at the edge which may be due to $1s$ -----> $4s$ and the main peak due to the $1s$ -----> $4p$ (West, 1984). These peaks are closely spaced which are typically only a few eV apart. The exact peak positions and intensities depend on details of oxidation state, site symmetry, surrounding ligands and the nature of the bonding.

XANES is normally referred to the detailed structure of the absorbance within about 50 eV beyond the edge. It involves transitions both to the unoccupied levels and the continuum. The resulting photoelectron, which has low energy, can undergo multiple scattering events by the surrounding atoms. The shape of the edge is thus highly sensitive to both the valency and coordination of the absorbing atom. The XANES is then very useful for valence state and site symmetry determinations. However, the complexity of the process involved makes a full theoretical treatment rather difficult and due to this the technique generally used is a 'fingerprint' technique where edges of a number of model compounds of known valency and coordination are compared with the unknown.

There are two approaches in interpreting XANES data.

1. *Shift of the main absorption edge.*

If the main edge is structureless, then its position can provide some charge information. It is well known that on oxidation the edge position shifts to higher energies which is known as the chemical shift. This has been demonstrated by Pt L-edge, XAS data (Robinson *et al.*, 1992), Cr K-edge (Bardwell *et al.*, 1992) and Fe K-edge (Morrel *et al.* 1987) studies that the higher the charge the greater will be the shift. In the studies done by Cramer and co-workers (Cramer *et al.*, 1976) on several Mo compounds a shift of approximately 10 eV for a charge variation of five was noted. Absorption edge differences between oxidised and reduced forms of a metalloprotein has been studied by Chan and co-workers (Chan *et*

al., 1978) and they found that the edge of the oxidised protein is about 2 eV above that of the reduced form.

Apart from valency the coordination numbers also contribute to edge shifts. This phenomenon was illuminated by Nabavi and co-workers (Nabavi *et al.*, 1990) in their studies on V-O compounds where they noticed a decrease in coordination number from five to four leads to a shift of the XANES pre peak towards lower energy together with a decrease of its intensity and a broadening of the linewidth. The shift has also been related to a shortening of the mean V-O distance.

It has been concluded by Pandey and Chetal (Pandey and Chetal, 1992) in their studies of K-edge shift in some Cu(II) systems that this approach is able to provide information on the changes in valency, coordination number, electronegativity and bond length; although the main governing factors are the effective charge and the bond length.

2. *Assignment of specific transitions.*

If structure within the edge is present, then the absorption peaks may be assigned to specific transitions. When bonding is ionic the spectral assignment is straightforward, with $1s$ -----> $3d$, $1s$ ----->$4s$, $1s$ -----> $4p$ appears at increasing energies; noting that $1s$ -----> $3d$ is very weak. The resulting ($3d$ -----> $4s$), ($4s$ -----> $4p$) and ($3d$ -----> $4p$) energy separation are comparable to the isoelectronic ion. When the bonding is strongly covalent

peak assignments are more difficult to make. Figure 2.11 shows schematically a typical X-ray absorption spectrum of a transition metal with the spectral assignment described above.

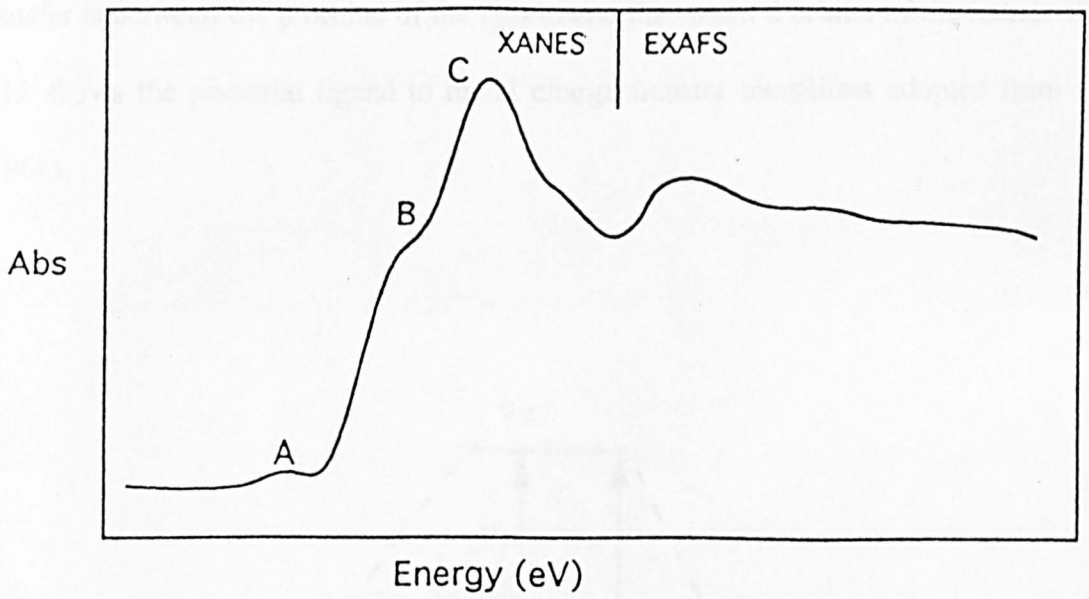

Figure 2.11 Schematic representation of a typical X-ray absorption spectra of a transition metal with A as 1*s* -----> 3*d*, B as 1*s* ----->4*s* and C as 1*s* -----> 4*p*.

In general, peaks A and C have been attributed to the transitions 1*s* -----> n*d* and 1*s* -----> (n+1)*p* respectively but the origin of peak B remains unexplained. Although transition 1*s* -

----> n*d* is dipole forbidden, Shulman and co-workers (Shulman *et al.*, 1976) have suggested that the vibronic mixing of the orbitals *s*, *p* and *d*-characters makes this transition allowed. Such a mixing is also caused by covalent interactions between metal and ligands. Peak B has been assigned to 1*s* -----> (n+1)*s* transition but Bair and Goddard (1980) have shown that the 1*s* -----> 4*s* monopole transition strength is far too weak to be observed and the peak appears at a wrong energy to fit the shoulder peak data. They suggest that the shoulder is due to 1*s* -----> 4*p* plus a ligand to metal charge transfer transition. The charge transfer is between the p orbital of the ligand and the vacant d orbital of the metal. Figure 2.12 shows the potential ligand to metal charge transfer transitions adopted from Lever (1968).

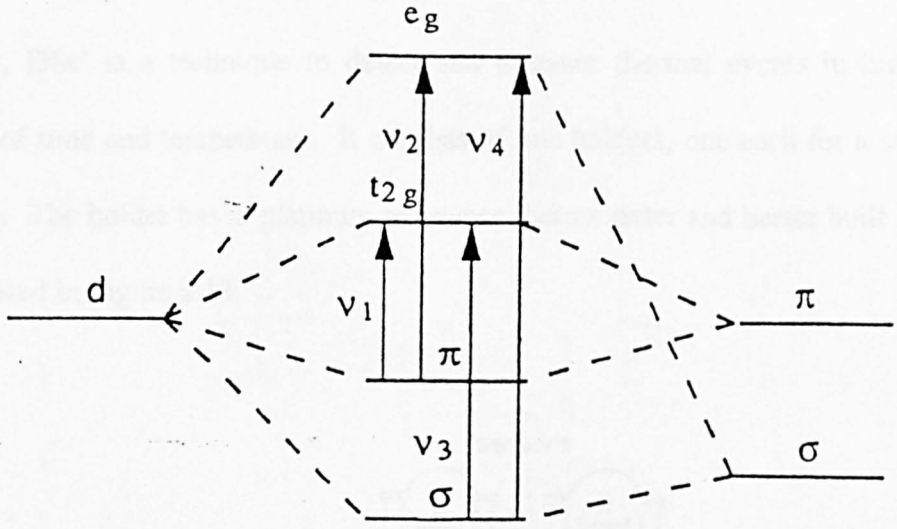

Figure 2.12 A simplified molecular orbital diagram illustrating the potential ligand to metal charge transfer transitions.

Four basic types of transitions may be expected, in order of increasing energy:

1. $\nu_1\ \pi L \longrightarrow M\ t_{2g}(\pi^*)$
2. $\nu_2\ \pi L \longrightarrow M\ e_g(\sigma^*)$
3. $\nu_3\ \sigma L \longrightarrow M\ t_{2g}(\pi^*)$
4. $\nu_4\ \sigma L \longrightarrow M\ e_g(\sigma^*)$

The effect of the ligand to metal wave function mixing is to increase the percentage of *p*-like symmetry components of these valence states. The increase of the intensity of these transitions at K-edges will be a probe of the wave function mixing (covalency).

2.3 Differential Scanning Calorimetry (DSC)

Basically, DSC is a technique to detect and measure thermal events in materials as a function of time and temperature. It consists of two holders, one each for a sample and a reference. The holder has a platinum resistance thermometer and heater built into its base as illustrated in Figure 2.13.

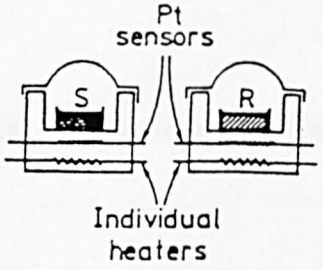

Figure 2.13 Illustration of the representation of a DSC system.

In this technique, a few milligrams of the sample and a reference material (e.g. γ-Al_2O_3) are separately heated, usually in hermetically sealed containers, in such a way that the sample and reference are always maintained at the same temperature. Temperature and power are monitored and supplied by the identical platinum resistance thermometers and heaters. Instrumental output, differential power as a function of time, is normally transmitted to a pen recorder with power as ordinate and the time abscissa transformed to temperature as that shown in Figure 2.14.

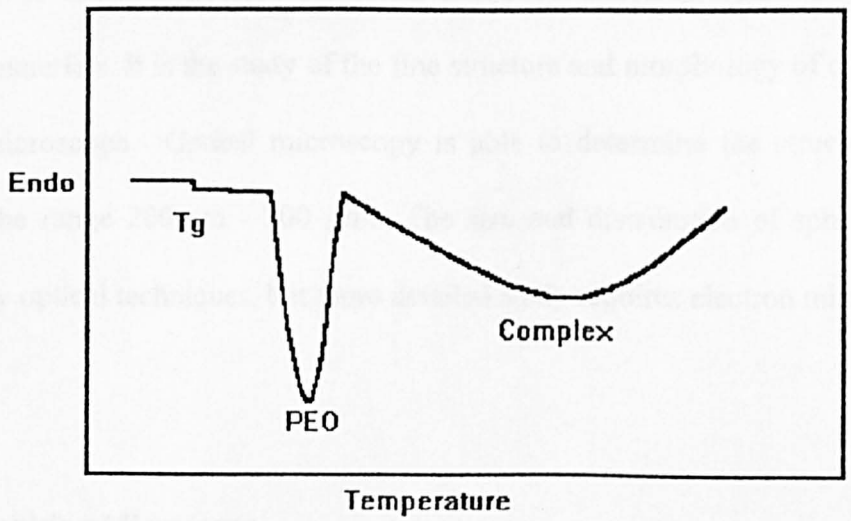

Figure 2.14 A typical DSC curve of a polymer electrolyte.

First order phase transitions which involve a 'latent heat' produce peaks on a DSC trace. For example, if some or all of a sample melts on heating an endothermic peak is seen, and

if a sample recrystallises on cooling an exothermic peak is produced. Higher order transitions which involve changes in heat capacity or on other thermal properties show up as steps or as changes in slope; for example, the glass transition appears as a step. For a semi-crystalline polymer electrolyte containing several regions or phases, DSC can provide a range of useful information.

2.4 Variable Temperature Polarising Microscopy (VTPM)

Microscopy is a physical characterisation technique which involves the formation of images of materials. It is the study of the fine structure and morphology of objects with the use of a microscope. Optical microscopy is able to determine the structure of a local region in the range 200 nm - 200 μm. The size and distribution of spherulites can be observed by optical techniques, but more detailed study requires electron microscopy.

2.4.1 Polarising Microscopy

Polarised light microscopy is an optical technique that enhances contrast in crystalline materials. It involves the interaction of materials which have anisotropic optical properties with polarised light.

Polarising microscopy uses plane polarised light to analyse structures that are birefringent. Birefringent structures have two refractive indices at right angles to one another (Rawlins, 1992). When plane polarised light hit a birefringent structure, it will be split into two rays which will then oscillate in planes parallel to the two directions of refractive index as illustrated in Figure 2.15.

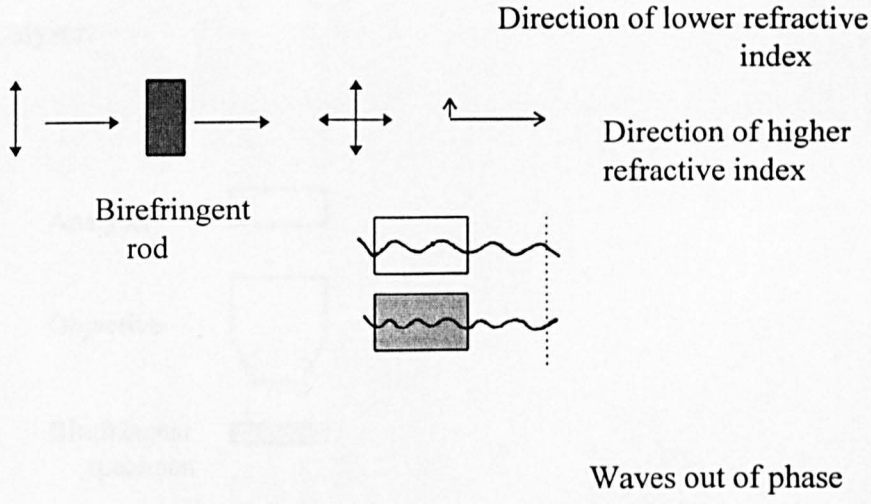

Figure 2.15 Plane polarised light hitting a birefringent object is split into two rays parallel to each of the directions of refractive index, resulting in different phase retardation for each set of rays.

Light passing through a material with a greater refractive index than air is slowed down or retarded. The two rays will be retarded to different extents because there are two refractive indices. The ray oscillating parallel to the direction of higher refractive index will be retarded more than the other. This means that there will be phase difference between the two rays.

In order to see the effect a birefringent structure has on plane polarised light, another polar placed behind it is crossed relative to the first. A diagram of this arrangement, a polarised light microscope, is shown in Figure 2.16. The first polar is usually called the polariser and the second is the analyser.

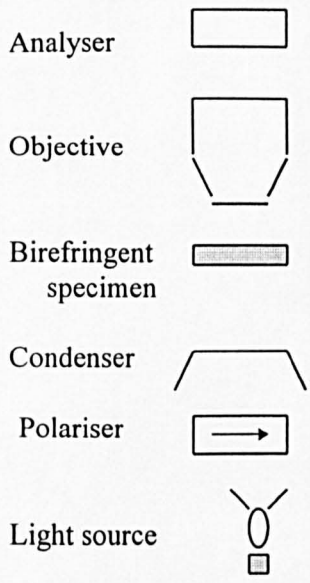

Figure 2.16 The components of a polarising microscope.

Increasing the phase difference between the two rays will make the image appear brighter and brighter, with a maximum at $\lambda/2$. Thereafter, the reverse situation happens and the image gets darker and darker.

2.4.2 Variable Temperature

A hot-stage on the microscope permits potentially valuable studies. By varying the temperature the changes in the polymer structure, particularly melting point and thermal behaviour, can be observed. This can be compared to other properties, such as, conductivity and in this way the understanding of the structure - conductivity can be enhanced.

3.0 Introduction

This chapter presents the experimental methods for the characterisation techniques carried out on all the samples studied. The techniques involved in all the samples prepared were X-ray absorption fine structure studies (EXAFS and XANES), a.c impedance spectroscopy, DSC and VTPM.

3.1 X-ray Absorption Fine Structures (XAFS)

XAFS were carried out at Daresbury Laboratory using synchrotron radiation. The experimental configuration is shown schematically in Figure 3.1.

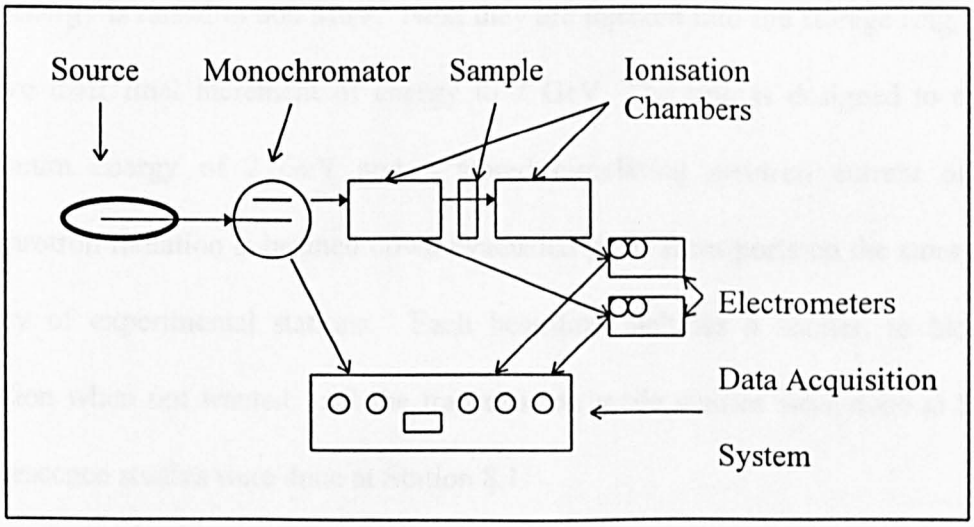

Figure 3.1 Schematic representation of the XAFS experimental set up.

The apparatus consists of five essential components:

- X-ray source
- Monochcromator
- Detectors
- Sample
- Data acquisition system

3.1.1 Instrumentation

The important criterion of the X-ray source is that it must provide a continuous spectrum of radiation. The synchrotron radiation source(SRS) at Daresbury is designed to provide intense beams of electromagnetic radiation. Electrons emitted from a hot cathode are first accelerated to 12 MeV in a linear accelerator, then pass to the booster synchrotron where their energy is raised to 600 MeV. Next they are injected into the storage ring, where they receive their final increment of energy to 2 GeV. The ring is designed to operate at a maximum energy of 2 GeV and a stored circulating electron current of 370 mA. Synchrotron radiation is beamed down evacuated pipes from ports on the storage ring to a variety of experimental stations. Each beamline includes a shutter, to block off the radiation when not wanted. All the transmission mode studies were done at Station 7.1. Fluorescence studies were done at Station 8.1.

For concentrated samples a transmission experiment is both the simplest and most effective. It involves measuring both the incident X-ray intensity and that of the transmitted through a thin and uniform film of the material of interest. Since in transmission experiments, a law analogous to Beer-Lambert's law applies, the data are usually plotted as *ln (I/Io)* versus *E*. The X-ray intensities are typically measured using ionisation chambers in conjunction with high-gain electrometers. Figure 3.2 depicts a typical transmission experimental set-up.

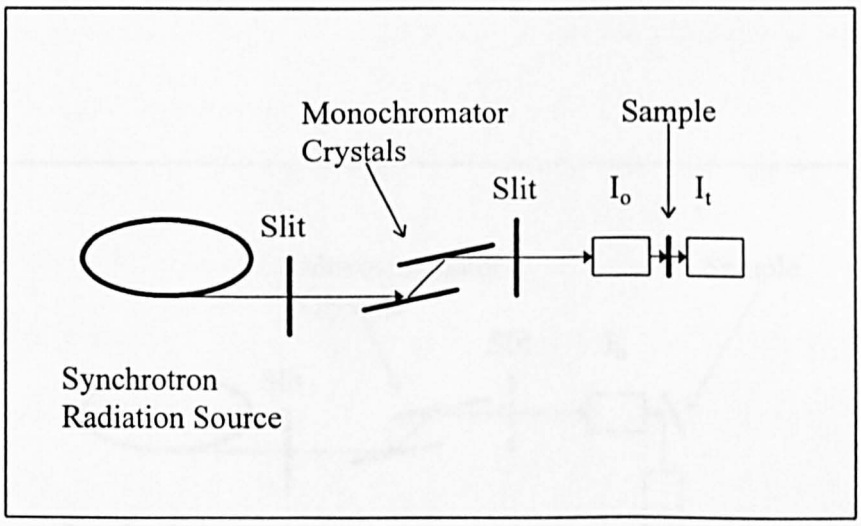

Figure 3.2 Schematic diagram of a transmission EXAFS experimental set-up.

For dilute samples, where absorption of the X-ray beam by the element of interest would be very low, a transmission geometry cannot be employed. Instead fluorescence can be employed as a detection method because the characteristic X-ray fluorescence intensity depends on the number of core holes generated, which in turn depends on the absorption coefficient. Fluorescence detection is much more sensitive than transmission because the signals are measured over an essentially constant and typically low background. In general, the incident and fluorescent beams impinge and leave the surface at 45 degrees to the X-ray beam and the detector being at 90 degrees. The detector in this case is a solid-state detector with a 12-channel analyser. The experimental configuration is depicted in Figure 3.3.

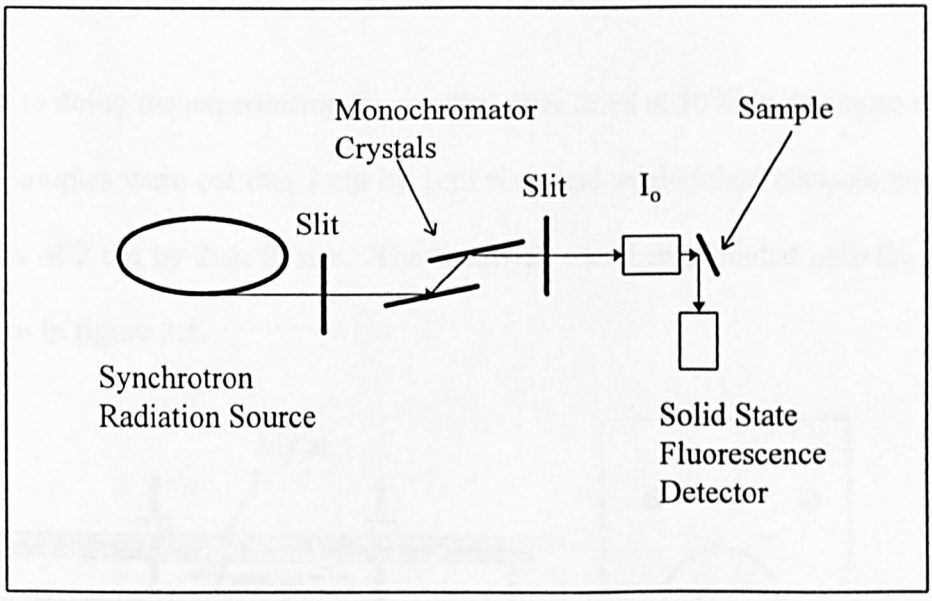

Figure 3.3 Schematic configuration of a fluorescence EXAFS experiment.

3.1.2 Sampling

The important criteria that the samples must posses are homogeneity, the right concentration and thickness. The samples must be homogeneous, if not the result will not be representative of the sample. There must be no pinholes as these will affect the absorption coefficient. The thickness of the sample must be optimised because if the sample is too thick then this will affect the attenuation of the signal and if it is too thin the signal to noise ratio is too weak for good deconvolution later in the data analysis. For the polymer electrolyte samples prepared, the thickness are well suited for the transmission experiments, 100 -150 μm thick. For powdered samples, such as the model compounds, they have to be diluted with the aid of boron nitride (a highly transmitting diluent) in order to achieve a good resolution.

Prior to doing the experiments the samples were dried at 50°C in a vacuum oven overnight. The samples were cut into 1 cm by 1cm sizes and sandwiched between transparent mylar sheets of 2 cm by 2cm in size. The sandwich was then mounted onto the sample holder, shown in figure 3.4.

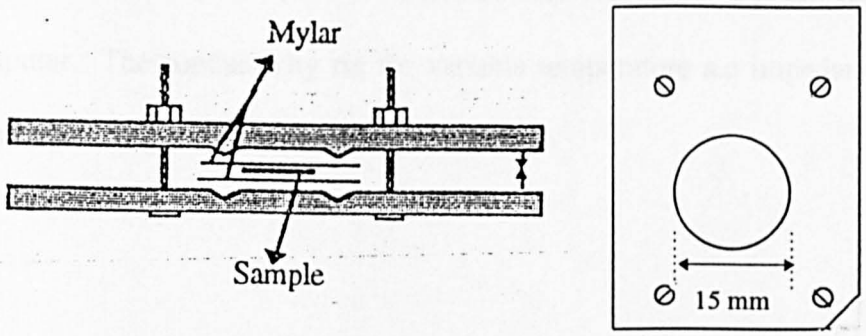

Figure 3.4 EXAFS sample holder used in the experiment.

There is a knife-edge configuration in the holder so as to keep the sample sealed. The samples were ensured dry by leaving in a vacuum oven overnight before placing in sealed sample bags in a desiccator to be transported to Daresbury.

3.1.3 Data Acquisition

The data of the spectra collected were stored in computer at the station and then transferred to the mainframe computer which can be retrieved whenever required for analysis.

3.2 A.C Impedance Spectroscopy

A.c impedance spectra of the samples studied were obtained employing a Hewlett Packard Impedance Analyzer model 4192A which can scan in the frequency range of 5 Hz to 13 MHz. Temperature dependence studies are accomplished by incorporating heaters in the sample housing of the conductivity rig which is connected to the impedance analyser. The data collection and temperature control was monitored by an IBM PC compatible computer. The conductivity rig for variable temperature a.c impedance measurements is illustrated in Figure 3.5.

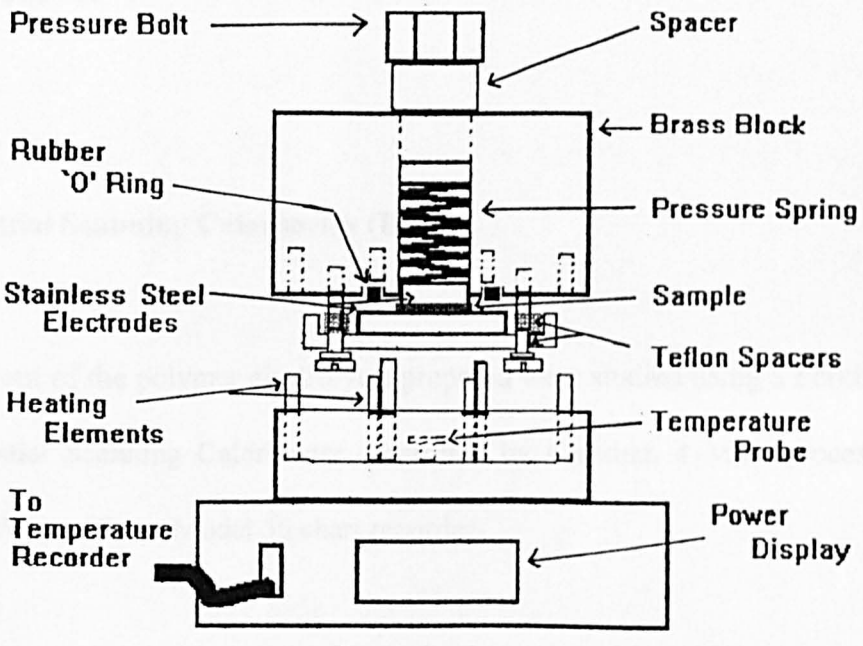

Figure 3.5 Conductivity rig for variable temperature ac impedance measurements.

A 1.5 by 1.5 cm section of the electrolyte film was cut and its thickness determined by a digital micrometer. The sample was then placed between stainless steel electrodes. This sandwich was placed in brass housing which can be heated at a controlled rate via heaters inserted into the block. Good contact was maintained by employing a spring loaded arrangement. Resistances of the samples at various temperatures can be extrapolated from the spectra obtained which are then used to evaluate the conductivity using the formula as mentioned in section 2..

3.3 Differential Scanning Calorimetry (DSC)

Thermal behaviour of the polymer electrolytes prepared were studied using a Perkin-Elmer DSC-4 Differential Scanning Calorimeter controlled by a system 4 Microprocessor and connected to a Perkin-Elmer Model 56 chart recorder.

The samples were studied over a temperature range of 20°C to 250°C. The samples were loaded into aluminium cans and hermetically sealed using a Perkin-Elmer crimper. The average sample mass used was 6 mg. The sample can was placed in the left hand sample holder and a reference can containing the same mass of Al_2O_3 on the right hand holder. The heating rate used was 10°C per minute and the heat flow rate was set at 5 mcal per second.

3.4 Variable Temperature Polarising Microscopy (VTPM)

The morphology of the polymer films prepared were studied using VTPM. The studies were done with the aid of an optical microscope (Olympus Model BH2). An Olympus Photomicrographic System Model PM-10ADS is attached to the microscope. The main components of the system are an automatic exposure body Model PM-PBSP and an automatic exposure control unit Model PM-CBSP which controls a 35 mm Olympus camera Model C-35AD. Variable temperature studies were made possible by attaching a heating block onto the microscope stage. The heaters were controlled by a computer via an interface.

All the samples were studied as cast. An aliquot of the size 4 mm by 4 mm of the sample was placed in the cavity of a single concave cavity slide. The sample was kept away from moisture by a cover slip glued over the cavity. The prepared slide was mounted on the hot stage and the images of the sample viewed and captured as required.

4.0 Introduction

This chapter presents the X-ray absorption near edge structures (XANES) studies carried out on some nickel systems to elucidate the structural differences in a series of different polymer matrices.

4.1 The Samples

The samples involved in the study were PEO_8:$NiBr_2$, PEG_8:$NiBr_2$, PPM_8:$NiBr_2$, and PPG_8:$NiBr_2$. PEG is poly(ethylene glycol), relative molar mass of 400, PPG is PEO plasticised with 50% PEG and PPM is PEO plasticised with the dimethyl rather than dihydroxy end-capped PEG.

PEO_8:$NiBr_2$ was formed by a two solvent technique where PEO and $NiBr_2$ were dissolved separately in acetonitrile and ethanol respectively. The two solutions were then mixed and stirred for 48 hours. The solvents were evaporated and the film were dried at 140°C under vacuum for 24 hours. PEG_8:$NiBr_2$ and PPM_8:$NiBr_2$ were prepared by dissolving the salt in PEG or PPM with the addition of a small amount of methanol and heating to 65°C. PPG samples were prepared by adding PEG to the casting solution prior to solvent evaporation.

4.2 Experimental of XAFS Studies

The samples were mounted in the EXAFS sample holder as described in section 3.1.2. Nickel K-edge spectra were obtained in transmission mode with 50% harmonic rejection at Station 7.1. The stored beam had an energy of 1.99 GeV and an average current of 100 mA.

4.3 Results

Figure 4.1 shows X-ray absorption as a function of energy in the region of the nickel K-edge in the nickel samples. Two sets of features could be observed from the shape of the spectra. The origin of the features will be discussed in the next section. Peaks that are common to all the spectra are the small pre-edge peak (labelled *A*) and a strong absorption peak (labelled *C*). The feature which differentiate the two sets is a shoulder (labelled *B*) which is easily discernible in PPM_8:$NiBr_2$ but less pronounced for PEO_8:$NiBr_2$, Figure 4.2.

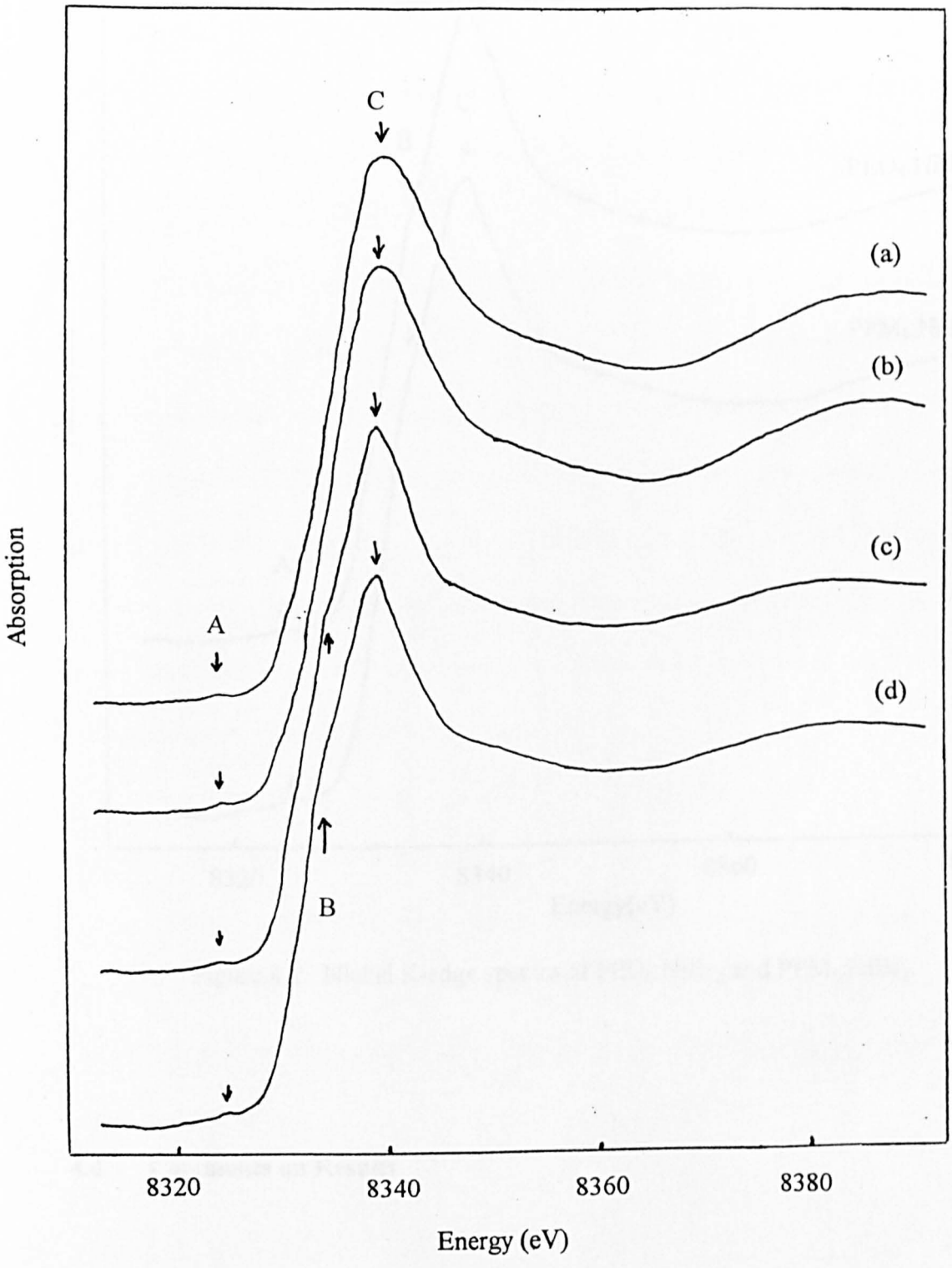

Figure 4.1 Nickel K-edge absorption spectra of (a) $PEG_8:NiBr_2$, (b) $PPG_8:NiBr_2$, (c) $PEO_8:NiBr_2$, and (d) $PPM_8:NiBr_2$

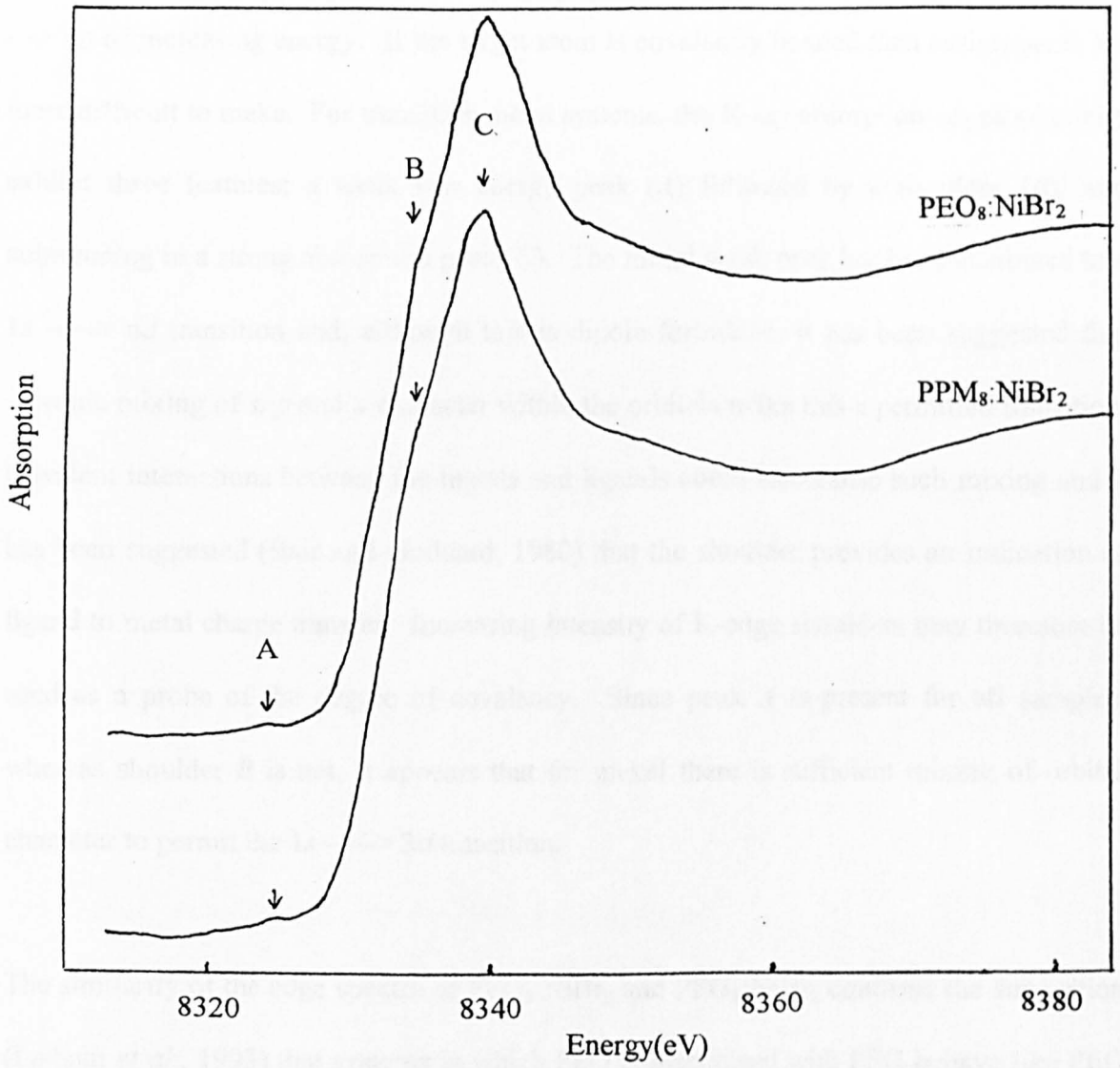

Figure 4.2 Nickel K-edge spectra of PEO_8:$NiBr_2$ and PPM_8:$NiBr_2$.

4.4 Comments on Results

Spectral features before or on the edge are normally assigned to internal electronic transitions within the target species. The spectral assignment is straightforward for

ionically bonded systems, and there is a set of transitions $1s$ -----> $3d$, $1s$ -----> $4s$ and $1s$ ----> $4p$ of increasing energy. If the target atom is covalently bonded then assignments are more difficult to make. For transition metal systems, the X-ray absorption edges generally exhibit three features; a weak low energy peak (*A*) followed by a shoulder (*B*); and culminating in a strong absorption peak (*C*). The initial weak peak has been attributed to a $1s$ -----> nd transition and, although this is dipole forbidden, it has been suggested that vibronic mixing of *s, p* and *d* character within the orbitals make this a permitted transition. Covalent interactions between the metals and ligands could also cause such mixing and it has been suggested (Bair and Goddard, 1980) that the shoulder provides an indication of ligand to metal charge transfer. Increasing intensity of K-edge shoulders may therefore be used as a probe of the degree of covalency. Since peak *A* is present for all samples, whereas shoulder *B* is not, it appears that for nickel there is sufficient mixing of orbital character to permit the $1s$ -----> $3d$ transition.

The similarity of the edge spectra of PEG_8:$NiBr_2$ and PPG_8:$NiBr_2$ confirms the suggestion (Latham *et al.*, 1993) that systems in which PEO is plasticised with PEG behave like PEG systems and not PEO systems. The shoulder for the PPM system is more pronounced than for the PEO system which might be due to the enhanced electron donating character of the methyl end-group.

5.0 Introduction

Two zinc systems were studied in the search for a better understanding of structure-conductivity relationships in PEO-based polymer electrolytes. The first system involved the measurement of the impedance before and after an X-ray absorption measurement of PEO_8:$ZnBr_2$ at different temperatures. The second was a set of structure-conductivity studies on zinc ultradilute systems in the form of PEO_n:$ZnBr_2$ (where n= 1000, 2000, 3000, 4000 and 5000).

5.1 Structure-conductivity Studies on PEO_8:$ZnBr_2$.

The objective of this study was to relate the XANES features at different temperatures to conductivity measured at the related temperatures.

5.1.1 Sample Preparation

The sample was prepared by a two solvent technique. In this technique the salt, 0.640 g of anhydrous $ZnBr_2$ (at 99.999% purity), was dissolved in 25 ml of anhydrous ethyl

alcohol (99% purity). The amount of salt to be used was determined by the following formula;

$$\text{amount of salt} = \frac{\text{relative molar mass of salt}}{44 \times n}$$

where, n is the mole ratio of polymer to salt and the figure '44' is the molecular mass of the repeat unit of PEO, $-CH_2-CH_2-O-$.

75 ml of anhydrous acetonitrile (99% purity) was then mixed with the salt solution. 1 g of the polymer, PEO, relative molar mass of 4×10^6 was sprinkled slowly in the salt solution. All the chemicals were supplied by Aldrich. The polymer was dried at 50°C under vacuum for 24 hours prior to preparation. The process of dissolution was done in a stoppered 250 ml *quick fit* conical flask containing a magnetic stirrer. The solution was left to stir for 48 hours. The whole process was conducted in an argon recirculating dry glove box.

The resulting solution was cast in a glass ring of 10 cm in diameter onto a teflon sheet supported by a glass plate. The casting process was conducted in a dry box for three to five days and the product was a white translucent 50 μm thick homogenous film which is flexible and quite strong. The film was then dried in a vacuum oven at 50°C for 24 hours and the dried film kept in sealed plastic sample bag in a desiccator.

A 1 cm by 1 cm piece of the sample was placed between two gold plated mylar sheets, with the plated side touching the sample forming a cell suitable for impedance

measurements. The sandwich was mounted onto the EXAFS holder. Good electrolyte - interface contact was ensured by heating the sample holder at 70°C, when the film softened and a small G-clamp was used to stick the electrolyte to the gold electrode. The sticking process of the electrolyte to the electrodes were done one week before the EXAFS and impedance measurements to ensure the melted PEO spherulites had enough time to recrystallise.

5.1.2 Experimental

The sample was placed between the incident and the transmitted ionisation chambers. Before the X-ray absorption run the impedance measurements were made manually scanning from 10 MHz to 1 kHz. The X-ray absorption run was made scanning from 120 eV before the edge to 120 eV after the edge. Just after the run another set of impedance measurements were made. This procedure was repeated at a temperature of 90°C. The required temperature is attained via a heater assembly which houses the sample holder. Another set of measurements were made when the heated sample was left to cool down for five hours.

5.1.3 Results of PEO_8:$ZnBr_2$ Systems

The raw X-ray absorption spectra of PEO_8:$ZnBr_2$ at the different conditions imposed are shown in Figure 5.1. The shape of the spectra of the polymer films are the same except for the shoulder after the main absorption peak which is more pronounced for the lower temperature spectrum. The positions of the observed peaks differ as shown in the expanded energy scale in Figure 5.2. The positions of the main absorption peaks of all the spectra are tabulated for comparison in Table 5.1.

Table 5.1 The positions of the main absorption peaks of PEO_8:$ZnBr_2$ at the various conditions.

Condition	*Main absorption peak position (eV)*
20°C(as cast)	9668.3
90°C	9670.3
20°C (after cooling from 90°C)	9669.3

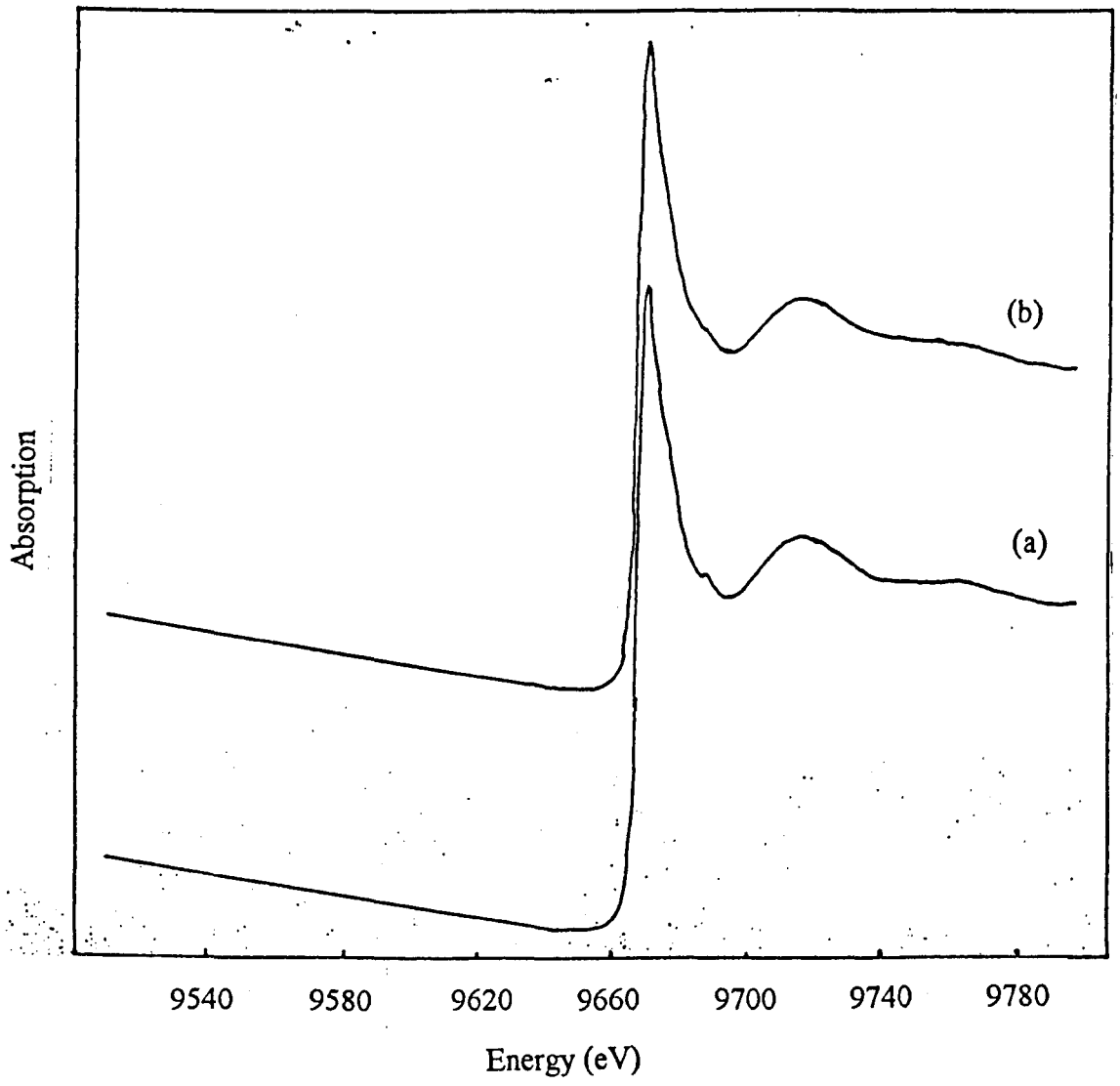

Figure 5.1 X-ray absorption spectra of PEO_8:$ZnBr_2$ at (a) room temperature and (b) 90°C.

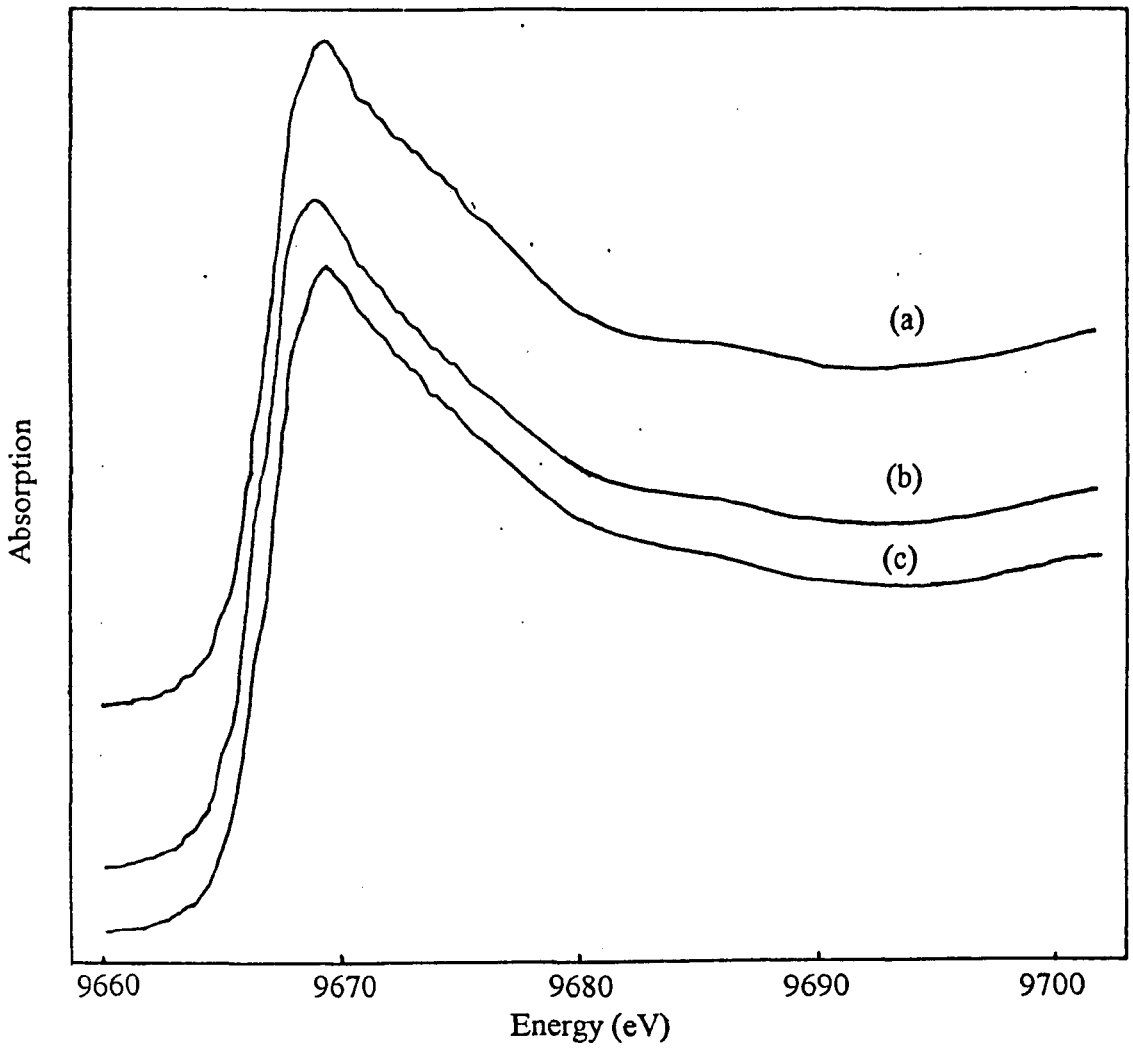

Figure 5.2 Expanded X-ray absorption spectra of PEO_8:$ZnBr_2$ at (a) room temperature, (b) 90°C and (c) room temperature after five hours heated at 90°C for one hour.

The impedance spectra of PEO_8:$ZnBr_2$ at the various conditions are shown in Figure 5.3. There is a slight difference in the shape of the two spectra. At 90°C the frequency window is more towards the spike regime, only half of the semicircle regime is shown, whereas at room temperature after the sample has cooled down the whole semicircle can be seen.

From the spectra the resistances were obtained at the intercept of the semicircle on the x-axis. The resistance at the higher temperature regime (1.4 x 10^3 Ω) is lower than the lower temperature regime (1.9 x 10^3 Ω).

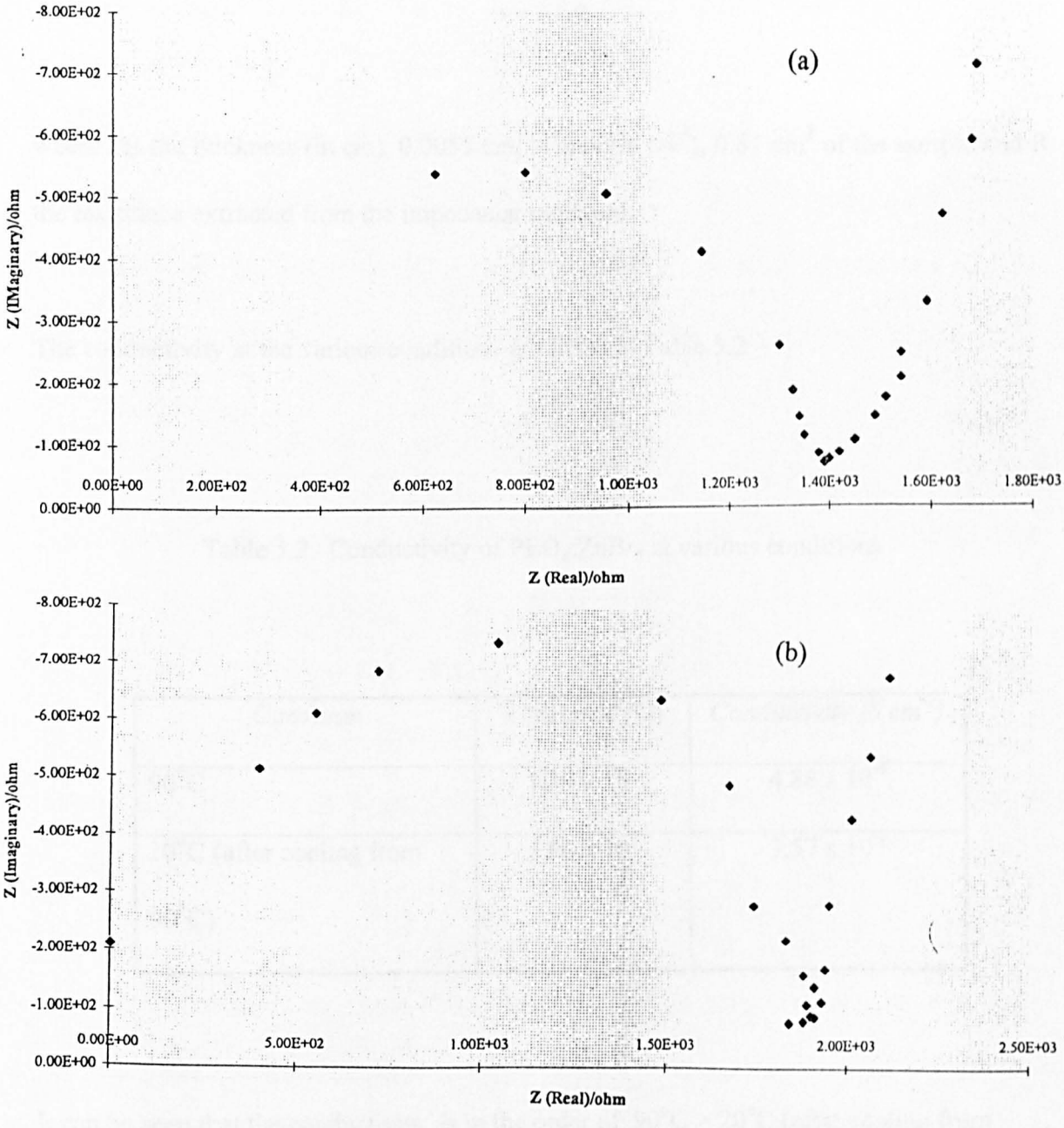

Figure 5.3 The impedance spectra of PEO_8:$ZnBr_2$ at (a) 90°C and (b) 20°C (after cooling from 90°C)

The resistances are used to evaluate the ionic conductivity of each sample using the equation

$$\sigma = l/AR$$

where l is the thickness (in cm), 0.0055 cm, A area (in cm^2), 0.81 cm^2 of the sample and R the resistance extracted from the impedance spectrum.

The conductivity at the various conditions are listed in Table 5.2

Table 5.2 Conductivity of PEO_8:$ZnBr_2$ at various conditions

Condition	*Resistance (Ω)*	*Conductivity (S cm^{-1})*
90°C	1.39×10^3	4.88×10^{-6}
20°C (after cooling from 90°C)	1.90×10^3	3.57×10^{-6}

It can be seen that the conductivity is in the order of 90°C > 20°C (after cooling from 90°C).

5.1.4 Comments on Results

The pre edge of the XANES of PEO_8:$ZnBr_2$ is devoid of structure. In such circumstances the position of the edge is useful in elucidating changes in structure of the systems under study. The edge position can provide certain information about the valence state. For example, shifts of 2 eV per charge number have been observed for molybdenum compounds by Cramer and coworkers (Cramer et al., 1976) and in metalloproteins by Chan and coworkers (Chan et al., 1978). In the present work the main absorption peak has been used to locate the shifts. The shifts are in the negative direction as the temperature of the system is increased.

The shifts of the absorption edge is not only due to change in valency of the target atom. Change in coordination numbers has also been reported to contribute to edge shifts (Nabavi et al., 1990). The shift has also been related to the change in mean bond length between the target atom and the coordinating species. It seems that the shifts is not simply due to the change in one of the factors discussed above. It could be due to the interplay of all the factors involved.

The slight difference in the shape of the shoulder above the main absorption edge might be due to a slight change in structural environment. The change might be in the form of a distortion with elongation of the Zn - ligand bond. The change in atomic distance can be seen by EXAFS but unfortunately the scanning window in the study was too narrow to include the EXAFS region.

Conductivity studies at different temperatures revealed the expected trend. The ionic conductivity increases with temperature as predicted by the Arrhenius relationship or more appropriately by the Vogel-Tamman-Fulcher (VTF) equation. At 90°C the low melting complexes and pure PEO have both melted and the film is in the metastable state, i.e. the film softens. In this state the amorphous proportion in the film is increased. Since the ionic conductivity is attributed to the amorphous state, an increase in the value is expected at this temperature.

The increase in conductivity is associated with an increase in the amount of the amorphous regime and a shift in the absorption edge to the negative direction. This suggests in the amorphous regime the valency of the target atom tends towards zero and an elongation of the Zn - ligand bond occurs.

An interesting feature observed in the present study is the ionic conductivity of the film at 20°C, five hours after being heated to 90°C for one hour. The value is about the same order of magnitude as the one at 90°C, about 25% lower. Usually the value at room temperature is about two orders of magnitude lower than that at 90°C. This is due to the slow recrystallisation rate of the spherulites. Even after five hours there is a sufficient amount of amorphous region still present to give such a high ionic conductivity. This is contrary to the results from studies carried out on PEO_8:$LiCF_3SO_3$ (Careem et al., 1993) in which recrystallisation is rapid. These observations can be substantiated by DSC studies on both systems by looking at the crash quenching cycle and reheating at a normal rate of 10 mcal/sec. Within one minute the same amount of spherulites could be seen melting at

the respective temperatures in the lithium system but none were present for the zinc system. In fact, even after an hour there was still no sign of spherulites appearing. The present study suggests that the heat treatment undergone suppresses the formation of spherulites, i.e. the crystalline region, thus enhancing the ionic conductivity of the system.

5.2 Structure - conductivity Studies on Zinc Ultradilute Systems

The aim of this part of the present study is to search for the conductivity relationships at ultradilute concentrations. The normal concentration range studied in solid polymer electrolytes is from n (PEO to salt mole ratio) equals to 4 to 100, where a composition is regarded as concentrated when n is less than 10; a medium concentration is between 10 and 30 and a dilute concentration is between 30 and 100. In the present study the compositions chosen are 1000, 2000, 3000, 4000 and 5000. These compositions can well be regarded as ultradilute. The system adopted for the study is PEO_n:$ZnBr_2$.

5.2.1 Sample Preparation

All preparative work was carried out under a dry argon atmosphere. PEO_n:$ZnBr_2$ samples were prepared using the two solvent technique. A stock solution of PEO_{10}:$ZnBr_2$ was first prepared by dissolving 0.512 g $ZnBr_2$ in 25 ml of ethanol in a 250 ml stoppered *quickfit* conical flask. 75 ml of acetonitrile was then added to the solution. 1.0 g of PEO (M.W =

$4x10^6$) was then dissolved gradually in the resulting solution. The mixture was left to stir for 48 hours.

PEO_{100}:$ZnBr_2$ was prepared from the stock solution by taking 10 ml PEO_{10}:$ZnBr_2$ and diluting with 90 ml of PEO solution. PEO_{1000}:$ZnBr_2$ was then prepared by diluting 10 ml PEO_{100}:$ZnBr_2$ with 90 ml of PEO solution. PEO_n:$ZnBr_2$ (n = 2000, 3000, 4000 and 5000) were prepared from the appropriate amount of PEO_{500}:$ZnBr_2$ and PEO solution (summarised in Table 5.3). PEO_{500}:$ZnBr_2$ was in turn prepared from PEO_{100}:$ZnBr_2$ by diluting 20 ml PEO_{100}:$ZnBr_2$ with 80 ml of PEO solution.

Table 5.3 Summary of the amount of PEO_{500}:$ZnBr_2$ required

Mole ratio of O:M (n)	Amount of PEO_{500}:$ZnBr_2$ (ml)	Amount of PEO solution (ml)
2000	25	75
3000	16.7	83.3
4000	12.5	87.5
5000	10	90

The mixtures were further left for 24 hours to stir before being cast in a glass ring of 10 cm in diameter onto a sheet of PTFE. The solvent was allow to evaporate in a non-circulating argon dry box for a further 48 hours. The resulting films of about 100 μm thick were dried

in a vacuum oven at 50°C for three days and stored in sealed plastic sample bags in a desiccator.

5.2.2 X-ray Absorption Fine Structure (XAFS) Studies

For XAFS studies the samples were mounted in the sample holder as described in chapter three. Because of the extreme dilution the samples were examined on station 8.1 at the SRS Daresbury, using fluorescence mode with 70% harmonic rejection for the K-edge spectra. The stored beam had an energy of 1.99 GeV and an average current of 150 mA.

5.2.2.1 XANES Studies

There are no significant differences in the XANES spectra for the PEO_n:$ZnBr_2$ polymer electrolytes other than small shifts in the position of the absorption edge. The edge are devoid of structures. The XANES window of the absorption spectra of the samples are shown in Figure 5.4.

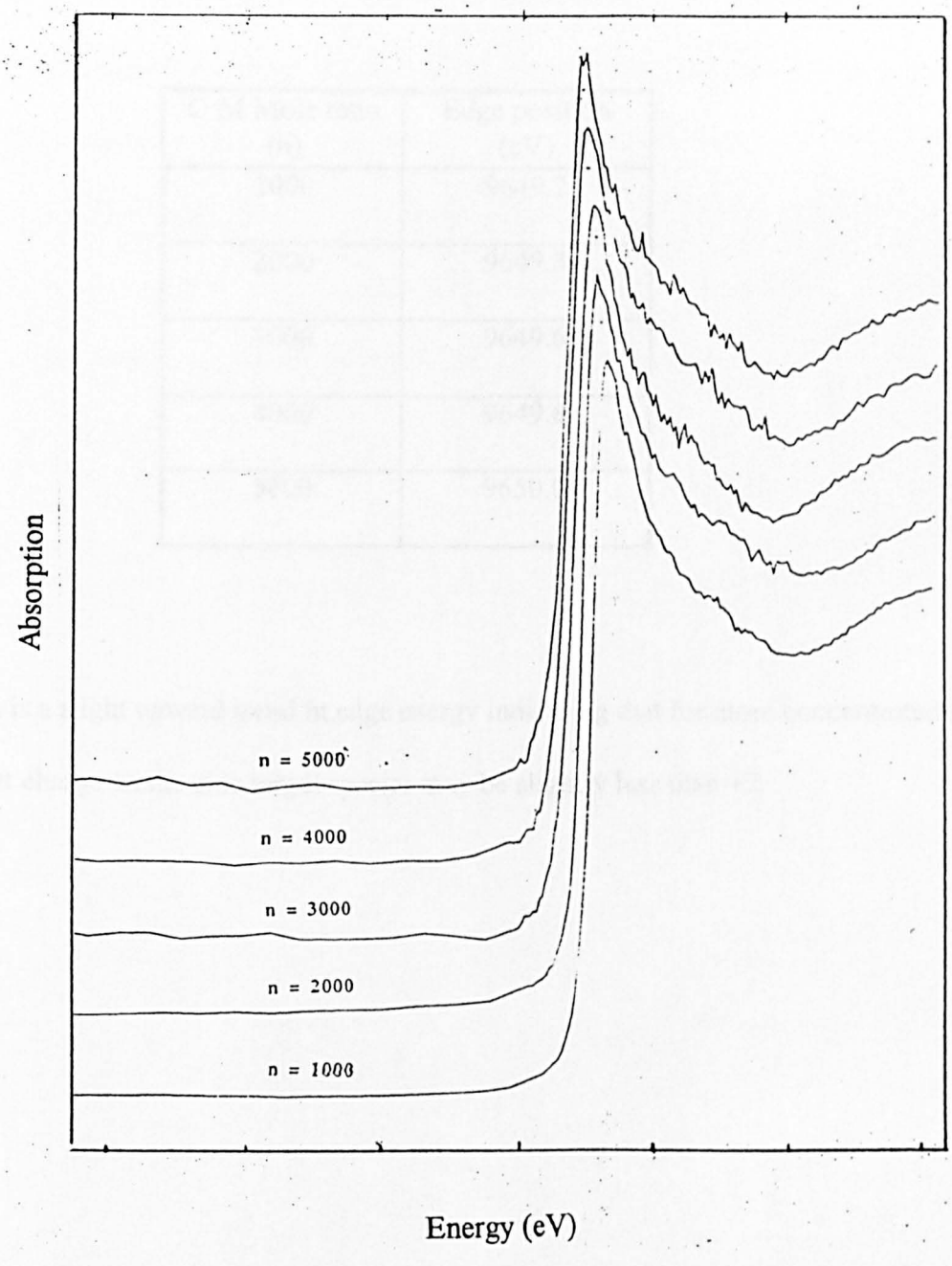

Figure 5.4 XANES window of the K-edge spectra of PEO_n:$ZnBr_2$

(Both the axes are not to scale, comparison plots only)

The edge energies are summarised in Table 5.4

Table 5.4 Main absorption edge position of PEO_n:$ZnBr_2$

O:M Mole ratio (n)	Edge position (eV)
1000	9649.2
2000	9649.3
3000	9649.6
4000	9649.8
5000	9650.0

There is a slight upward trend in edge energy indicating that for more concentrated systems the net charge on the zinc target species may be slightly less than +2.

5.2.2.2 EXAFS Studies

The process involved in EXAFS data analysis is discussed in section 2.2.2.2. The model compounds used in determining the phaseshifts, which were used in the fitting process of the ultradilute samples, were ZnO and $ZnBr_2$. Since the concentration of the zinc samples are ultradilute the fitting process is quite tricky. Figures 5.5 and 5.6 shows examples of the EXAFS in *k*-space and the fourier transform giving interatomic distance. The EXAFS results on the model compounds and the ultradilute zinc samples are tabulated in Tables 5.5 and 5.6.

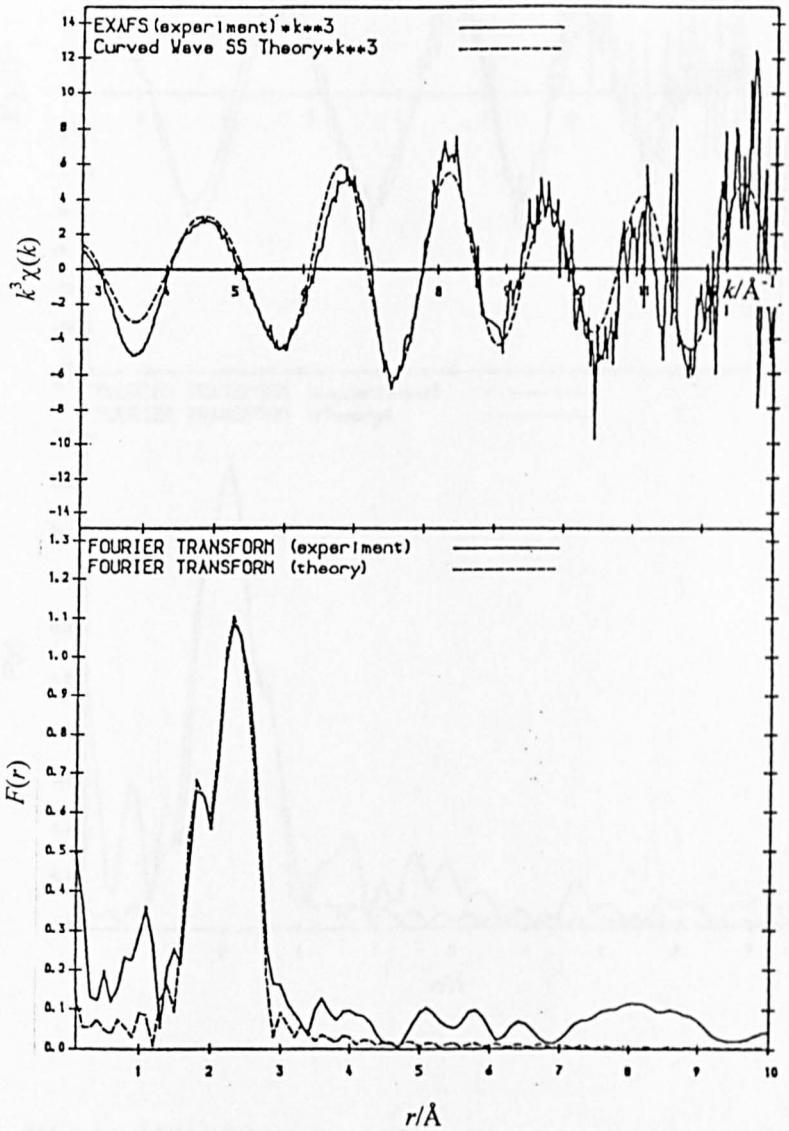

Figure 5.5 Weighted EXAFS spectra in *k*-space and the Fourier transforms of PEO_{1000}:$ZnBr_2$

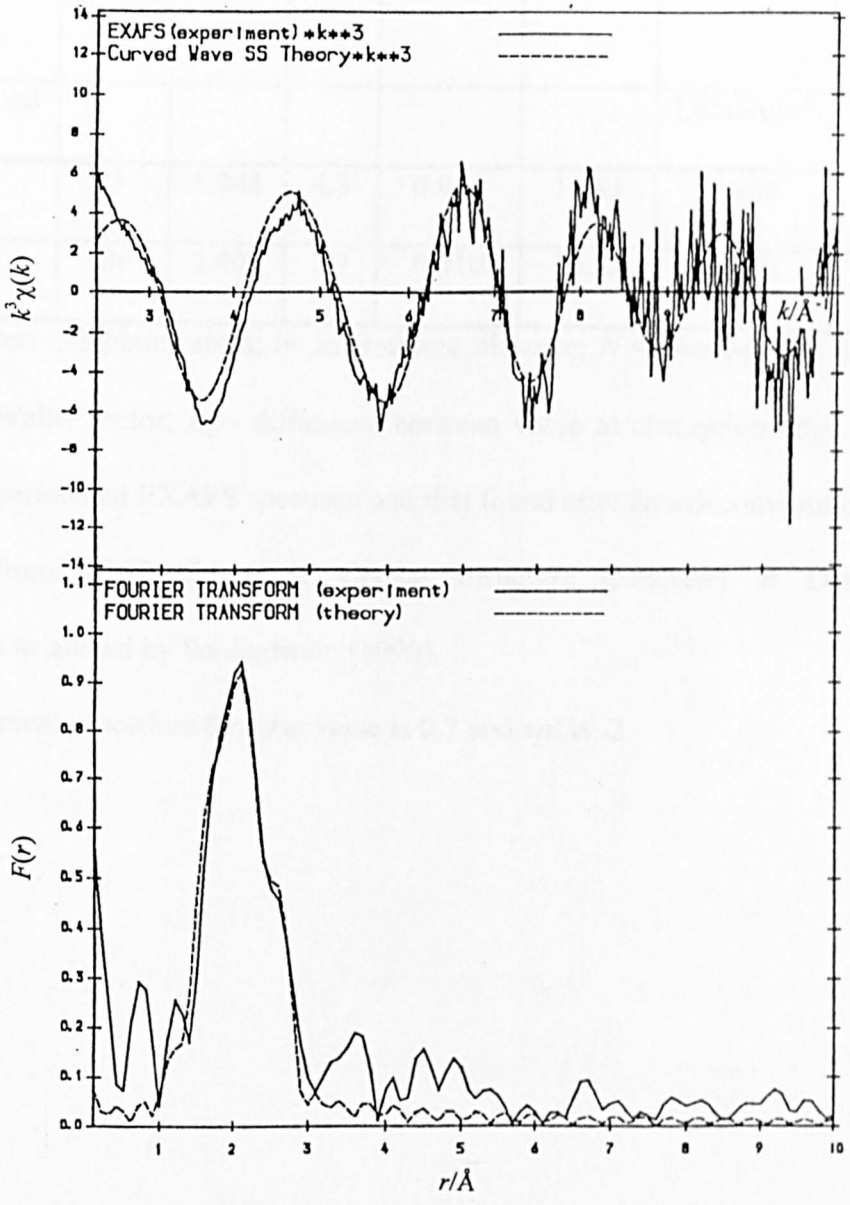

Figure 5.6 Weighted EXAFS spectra in *k*-space and the Fourier transforms of PEO_{3000}:$ZnBr_2$

Table 5.5 EXAFS results of zinc model compounds.

Compounds	NNA	r (Å)	N	σ^2 (Å^2)	$E_0(eV)$	r (Å)	N
Experimental						Literature*	
ZnO	O	1.944	4.3	0.011	13.83	1.950	4.0
ZnBr2	Br	2.402	3.7	0.010	13.32	2.415	4.0

NNA= nearest neighbour atom; r= interatomic distance; N = coordination number; σ^2=Debye-Waller factor; E_0= difference between value at absorption edge energy from the experimental EXAFS spectrum and that found after data deconvolution.

* Obtained from ICSD (Inorganic Crystal Structure Database) at Daresbury Laboratories as quoted by Schlindwein (1990).

In the refinement procedure the *afac* value is 0.7 and *vpi* is -2.

Table 5.6 EXAFS results of PEO_n:$ZnBr_2$ (n = 1000, 2000, 3000, 4000 and 5000)

Sample PEO_n:$ZnBr_2$	NNA	r (Å)	N	σ^2 (Å^2)	E_o(eV)
n = 1000	O	1.965	3.4	0.021	16.19
	Br	2.400	2.0	0.010	
n = 2000	O	1.952	2.2	0.030	13.40
	Br	2.402	2.0	0.009	
n = 3000	O	1.947	2.0	0.024	15.20
	Br	2.370	2.0	0.010	
n = 4000	O	1.936	3.3	0.025	15.52
	Br	2.351	1.2	0.009	
n = 5000	O	1.930	3.4	0.020	16.41
	Br	2.349	1.2	0.010	

NNA= nearest neighbour atom; r= interatomic distance; N = coordination number; σ^2=Debye-Waller factor; E_o= difference between value at absorption edge energy from the experimental EXAFS spectrum and that found after data deconvolution.

In the refinement procedure the *afac* value is 0.7 and *vpi* is -2.

From the results it could be seen that in PEO_{1000}:$ZnBr_2$ Zn is coordinated to only two oxygens whereas for the other, more dilute systems, Zn is coordinated to four oxygens.

The Zn coordination to Br is about 1.0 and is the same in all the systems. The Zn - O interatomic distance in PEO_{1000}:$ZnBr_2$ is much longer than the rest of the systems.

5.2.3 Conductivity Studies

Ionic conductivities of the ultradilute polymer electrolytes were evaluated using the a.c. impedance technique as described in section 3.2. Examples of the impedance spectra obtained are shown in Figure 5.7 and Figure 5.8.

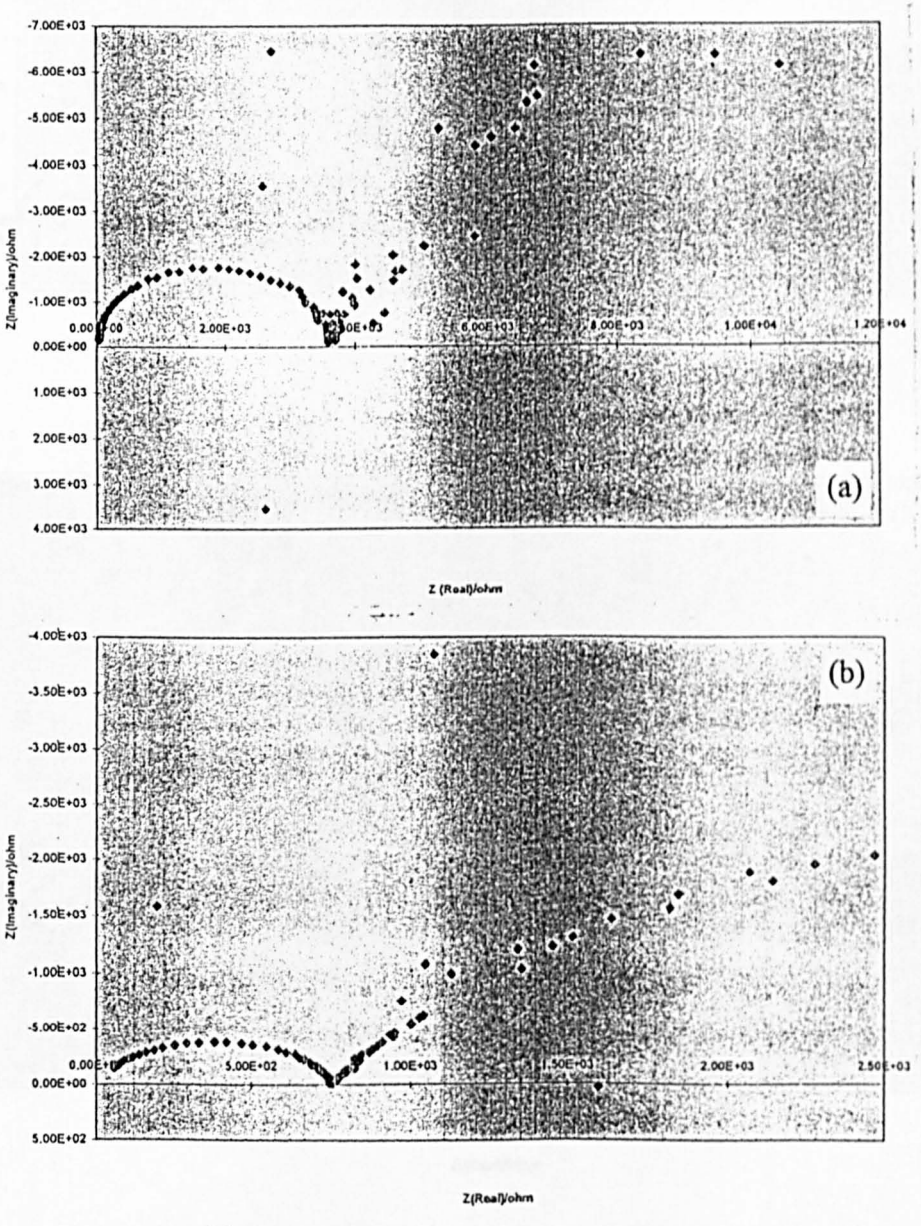

Figure 5.7 Impedance spectra of PEO_{1000}:$ZnBr_2$ at (a) 70°C and (b) 120°C

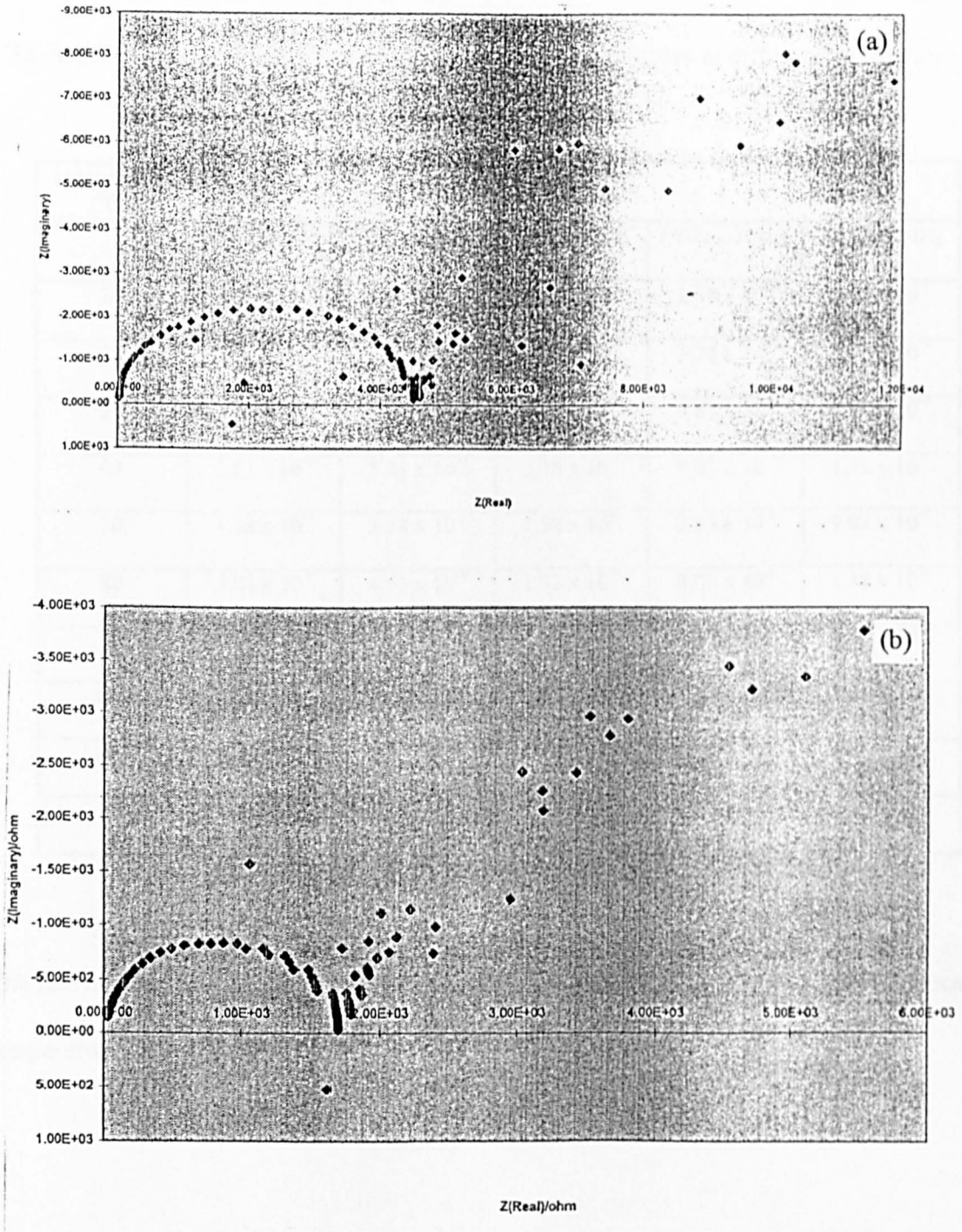

Figure 5.8 Impedance spectra of PEO_{3000}:$ZnBr_2$ at (a) 70°C and (b) 120°C

The conductivities evaluated at different temperatures for all the ultradilute samples are tabulated in Table 5.7.

Table 5.7 Ionic conductivities of the zinc ultradilute samples at different temperatures.

Temperature (°C)	Conductivity (S cm^{-1})				
	PEO_{1000}:$ZnBr_2$	PEO_{2000}:$ZnBr_2$	PEO_{3000}:$ZnBr_2$	PEO_{4000}:$ZnBr_2$	PEO_{5000}:$ZnBr_2$
30	1.88×10^{-8}	1.69×10^{-8}	1.35×10^{-8}	1.69×10^{-8}	5.64×10^{-9}
40	1.88×10^{-8}	3.38×10^{-8}	2.26×10^{-8}	3.38×10^{-8}	1.13×10^{-8}
50	2.51×10^{-8}	6.77×10^{-8}	6.77×10^{-8}	9.67×10^{-8}	2.26×10^{-8}
60	2.51×10^{-7}	5.21×10^{-7}	3.38×10^{-7}	9.02×10^{-7}	1.25×10^{-7}
70	1.88×10^{-6}	3.38×10^{-6}	1.50×10^{-6}	2.33×10^{-6}	9.02×10^{-7}
80	3.01×10^{-6}	4.51×10^{-6}	1.93×10^{-6}	3.08×10^{-6}	1.19×10^{-6}
90	4.18×10^{-6}	6.15×10^{-6}	2.51×10^{-6}	3.76×10^{-6}	1.50×10^{-6}
100	5.78×10^{-6}	7.52×10^{-6}	2.94×10^{-6}	4.51×10^{-6}	1.74×10^{-6}
110	8.35×10^{-6}	9.40×10^{-6}	3.56×10^{-6}	5.21×10^{-6}	1.88×10^{-6}
120	1.00×10^{-5}	1.13×10^{-5}	3.98×10^{-6}	6.15×10^{-6}	2.33×10^{-6}

The above data are used in the Arrhenius plot of log conductivity versus the reciprocal of temperature as in Figure 5.9.

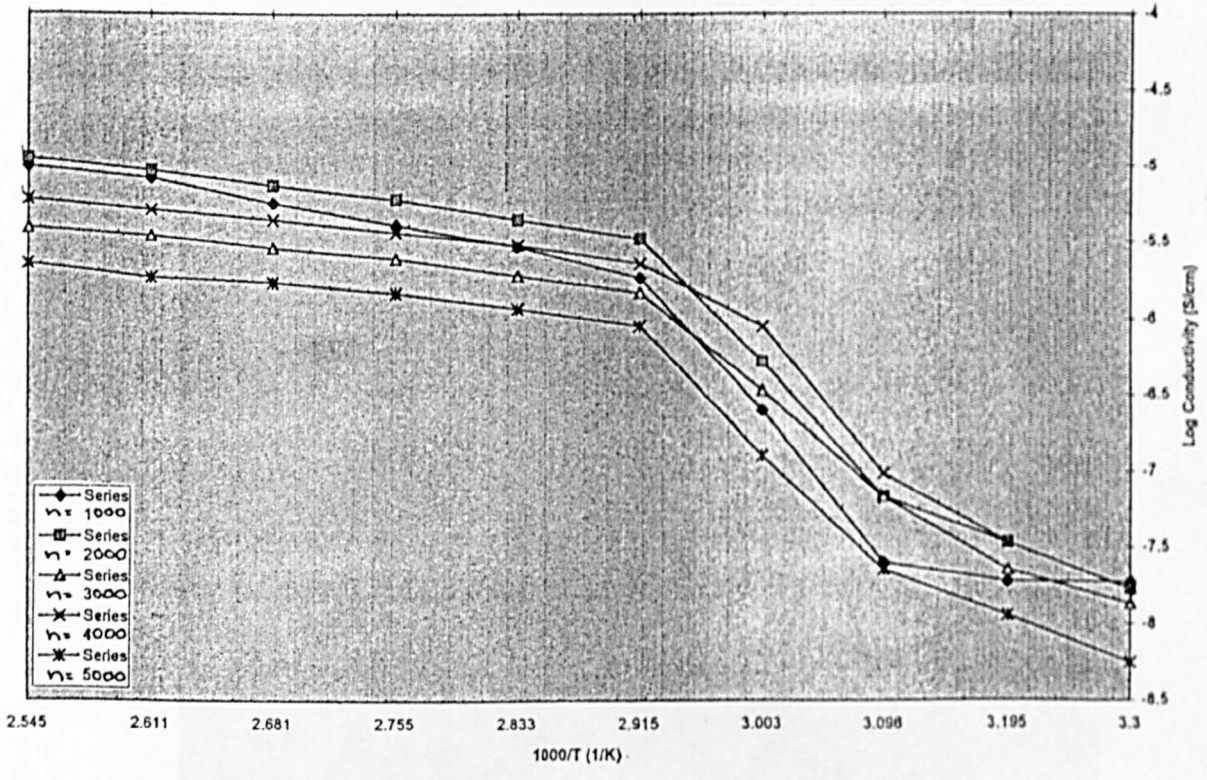

Figure 5.9 The log conductivity versus the reciprocal of temperature plot of PEO_n:$ZnBr_2$ (n = 1000, 2000, 3000, 4000 and 5000)

The shape of the plots are similar to other PEO-based polymer electrolytes, with a knee at the melting point of the PEO in the systems. At high temperatures the conductivity is in the order of PEO_{2000}:$ZnBr_2$ > PEO_{1000}:$ZnBr_2$ > PEO_{4000}:$ZnBr_2$ > PEO_{3000}:$ZnBr_2$ > PEO_{5000}:$ZnBr_2$. At low temperature (30°C) the conductivity is in the order of PEO_{1000}:$ZnBr_2$ > PEO_{2000}:$ZnBr_2$ > PEO_{4000}:$ZnBr_2$ > PEO_{3000}:$ZnBr_2$ > PEO_{5000}:$ZnBr_2$. The gradient of the PEO_{1000}:$ZnBr_2$ curve is steeper than the rest. Plots of molar conductivity versus concentration have also been done, as shown in Figure 5.10 and Figure 5.11.

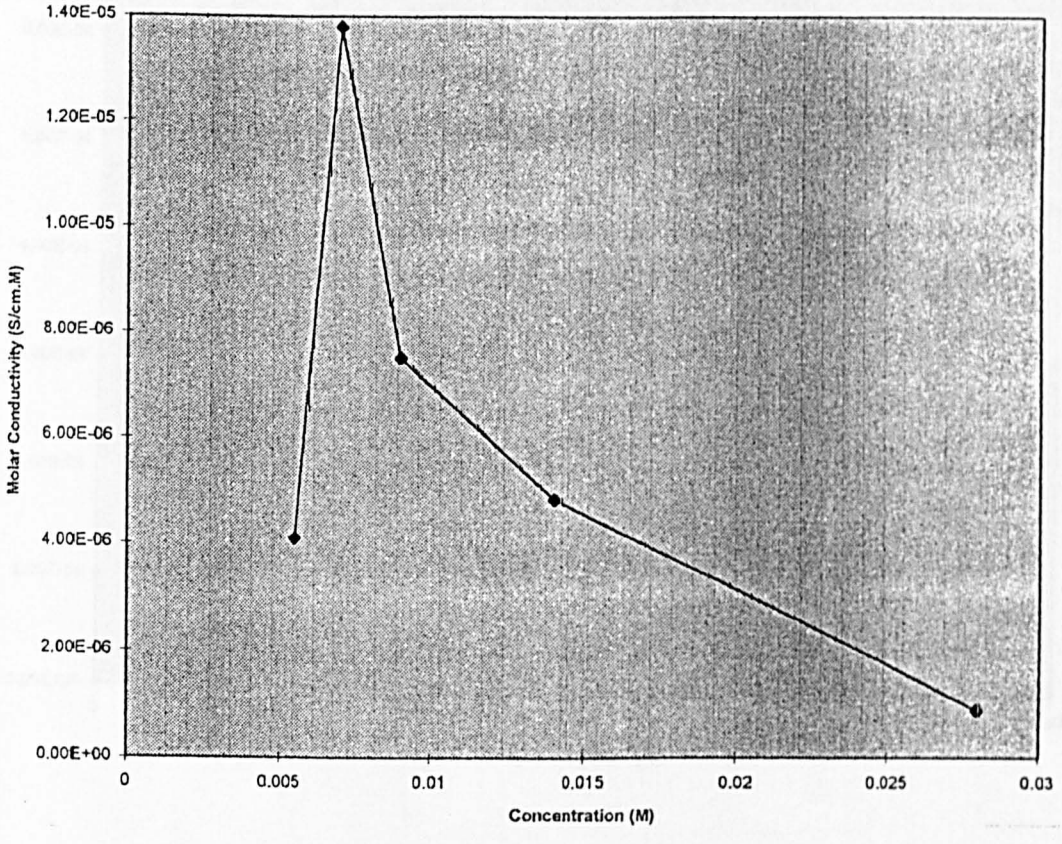

Figure 5.10 Molar conductivity versus concentration plot at 50°C.

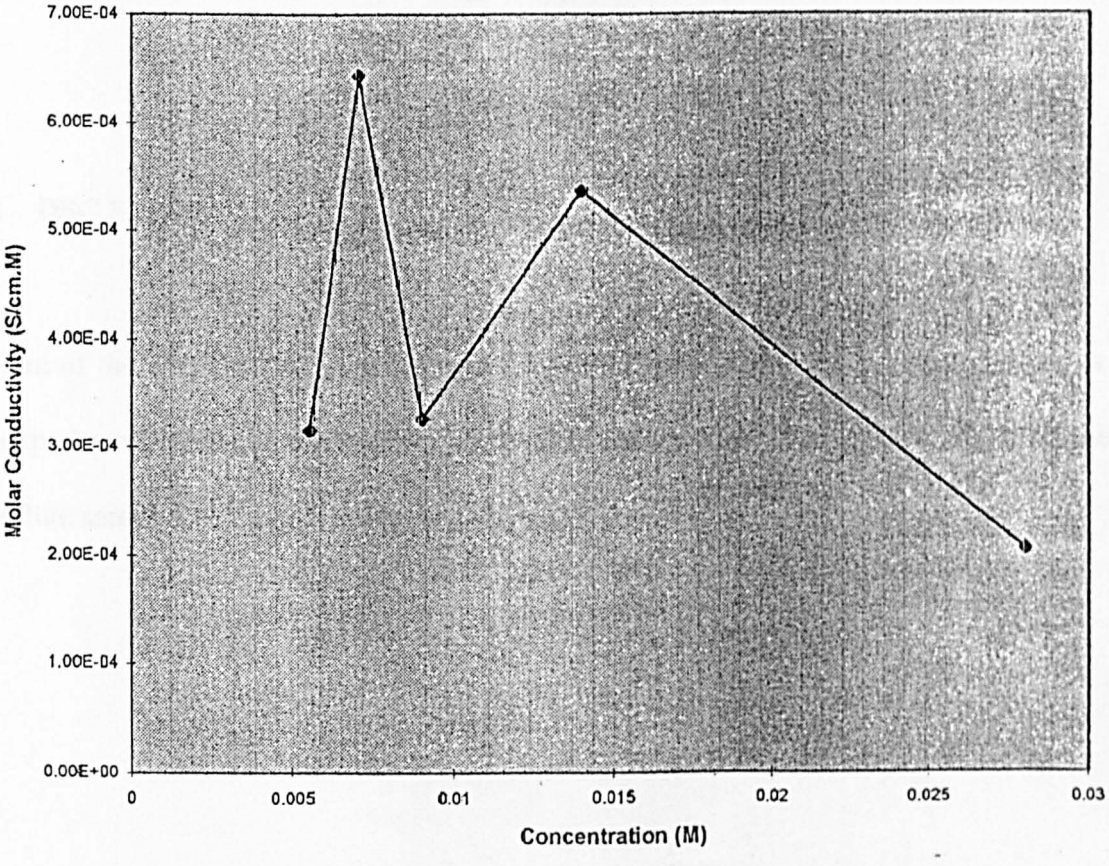

Figure 5.11 Molar conductivity versus concentration plot at 100°C.

The molar conductivity seems to decrease with concentration except for the most dilute system in the present studies. At both temperatures (50°C and 100°C) the molar conductivity of PEO_{4000}:$ZnBr_2$ is the highest in the concentration range studied. At the high temperature regime the molar conductivity increases with lower concentration and reach a maximum at PEO_{4000}:$ZnBr_2$ which then decreases drastically at PEO_{5000}:$ZnBr_2$. At the lower temperature regime the molar conductivity fluctuates; low at PEO_{1000}:$ZnBr_2$; larger at PEO_{2000}:$ZnBr_2$; down again at PEO_{3000}:$ZnBr_2$ and it reaches a maximum at PEO_{4000}:$ZnBr_2$ and drops again at PEO_{5000}:$ZnBr_2$.

5.2.4 DSC Studies

The aim of the DSC studies is to identify the phases present and the transition positions. The experimental technique is outlined in detail in section 3.3. The DSC traces of all the ultradilute samples are shown in Figure 5.12 and Figure 5.13.

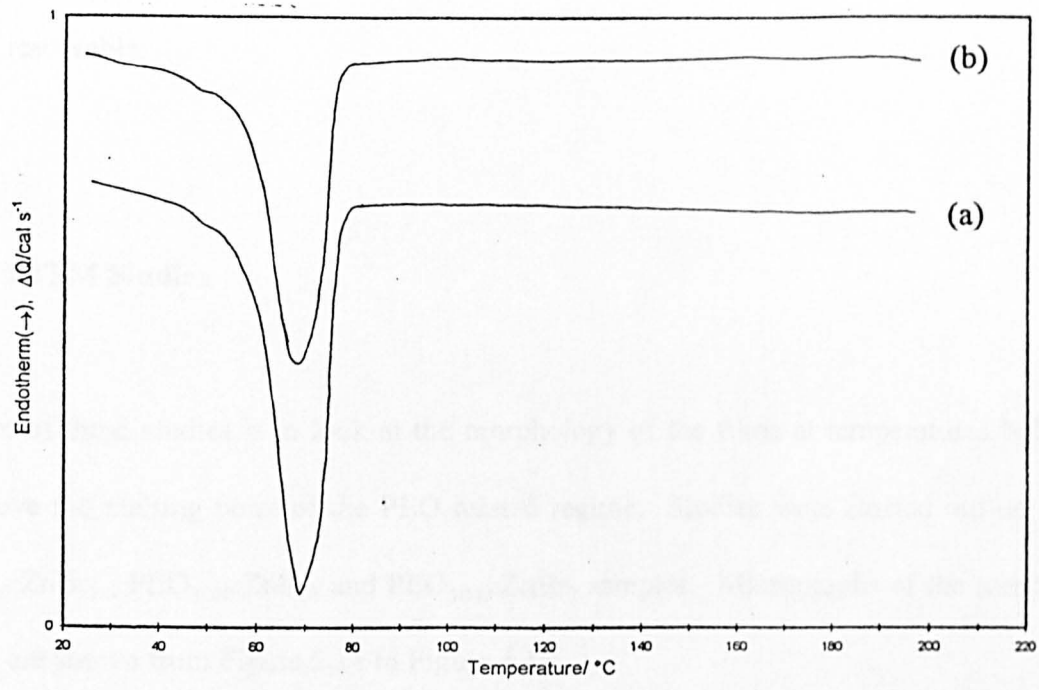

Figure 5.12 DSC traces of (a)PEO_{1000}:$ZnBr_2$ and (b) PEO_{2000}:$ZnBr_2$

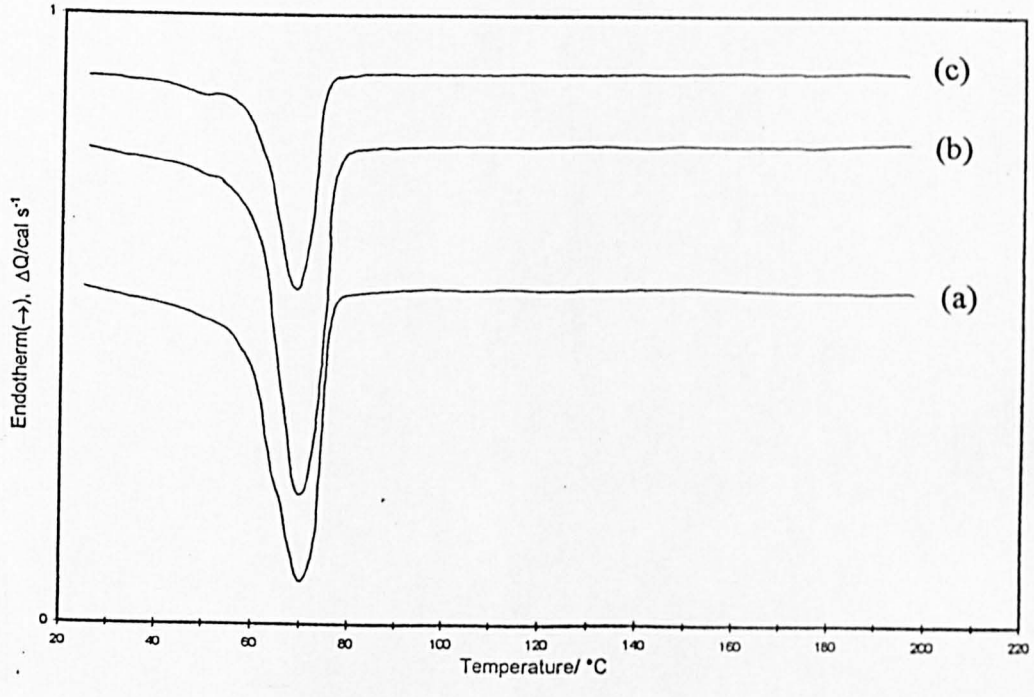

Figure 5.13 DSC traces of (a)PEO_{3000}:$ZnBr_2$, (b) PEO_{4000}:$ZnBr_2$ and (c) PEO_{5000}:$ZnBr_2$

All the traces show similar features, a PEO related peak at about 70°C. No high melting peak is resolvable.

5.2.5 VTPM Studies

The aim of these studies is to look at the morphology of the films at temperatures below and above the melting point of the PEO related regime. Studies were carried out on the PEO_{1000}:$ZnBr_2$, PEO_{3000}:$ZnBr_2$ and PEO_{5000}:$ZnBr_2$ samples. Micrographs of the samples studied are shown from Figure 5.14 to Figure 5.19.

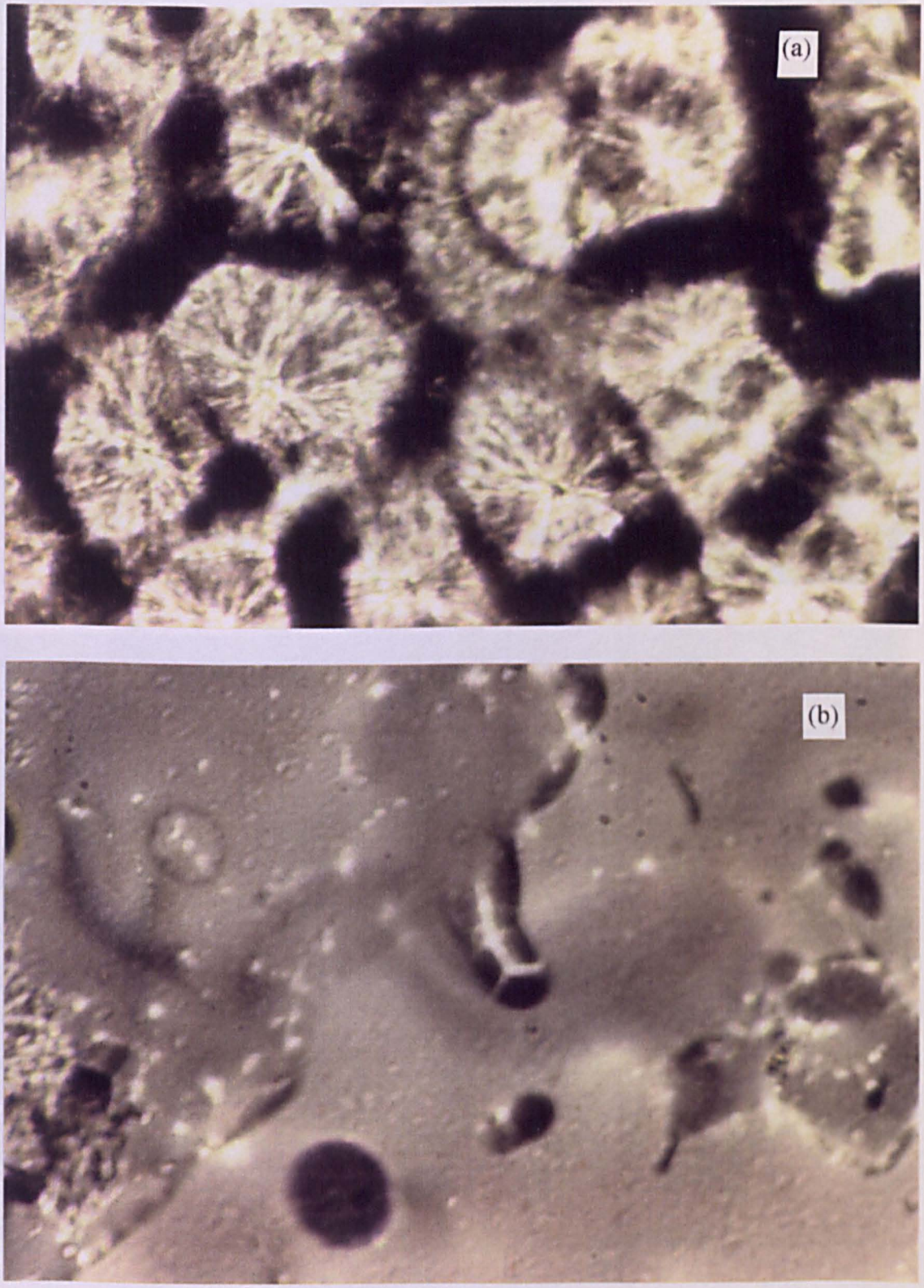

Figure 5.14 Micrographs of PEO_{1000}:$ZnBr_2$ at (a) 30°C and (b) 70°C

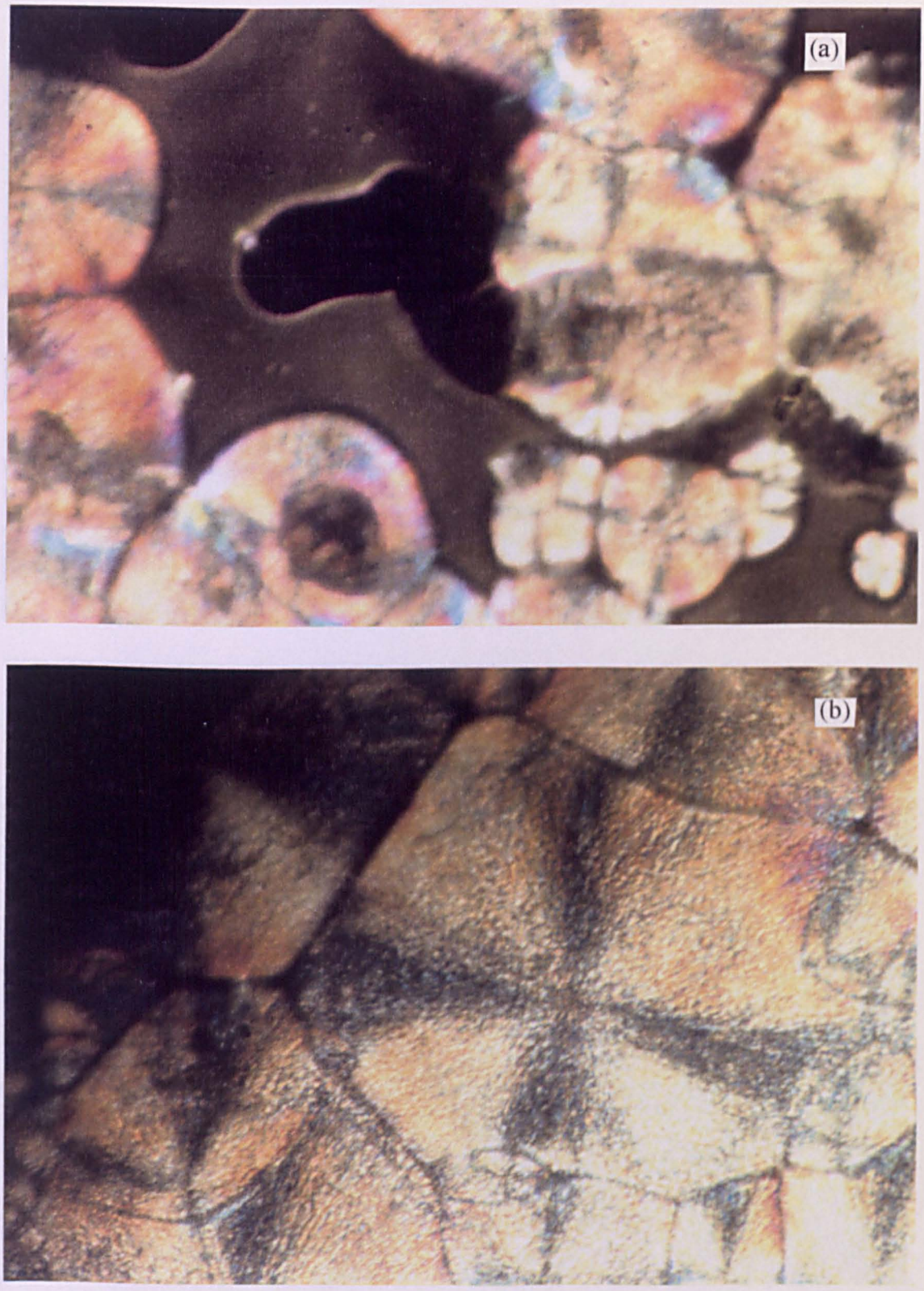

Figure 5.15 Micrographs of PEO_{1000}:$ZnBr_2$ crystallising at (a) 40°C and (b) 30°C

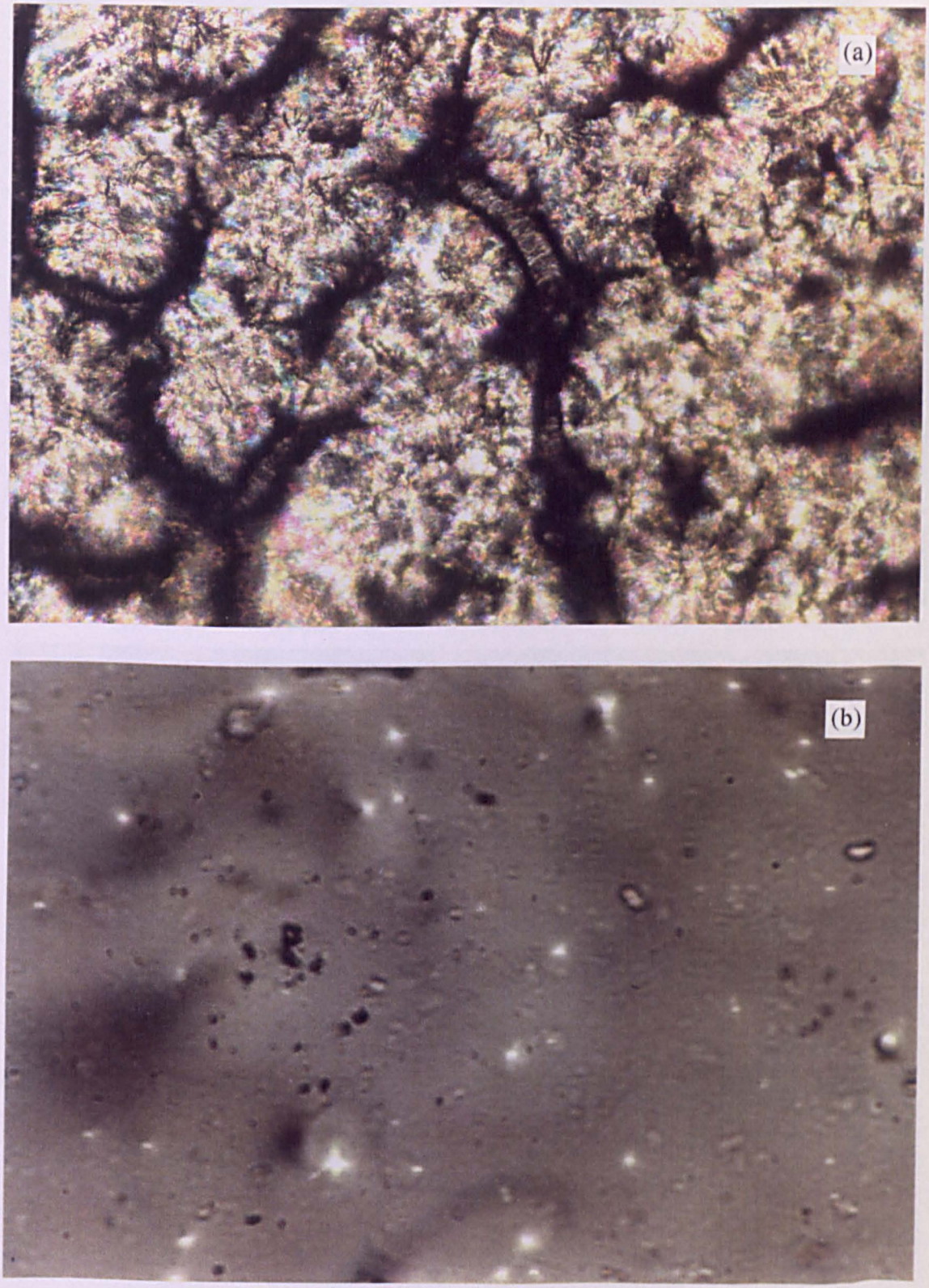

Figure 5.16 Micrographs of PEO_{3000}:$ZnBr_2$ at (a) 30°C and (b) 70°C

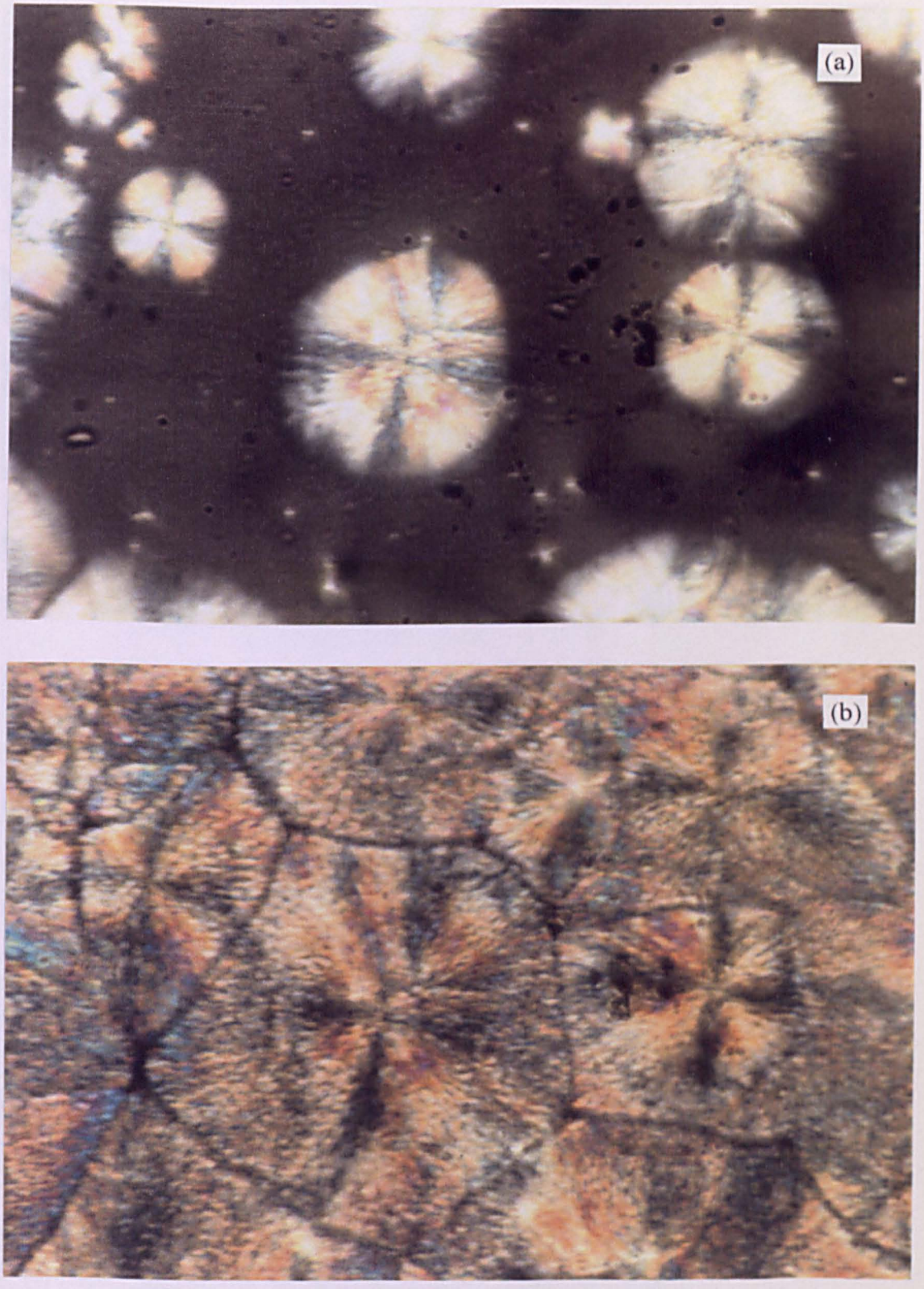

Figure 5.17 Micrographs of PEO_{3000}:$ZnBr_2$ crystallising at (a) 40°C and (b) 30°C

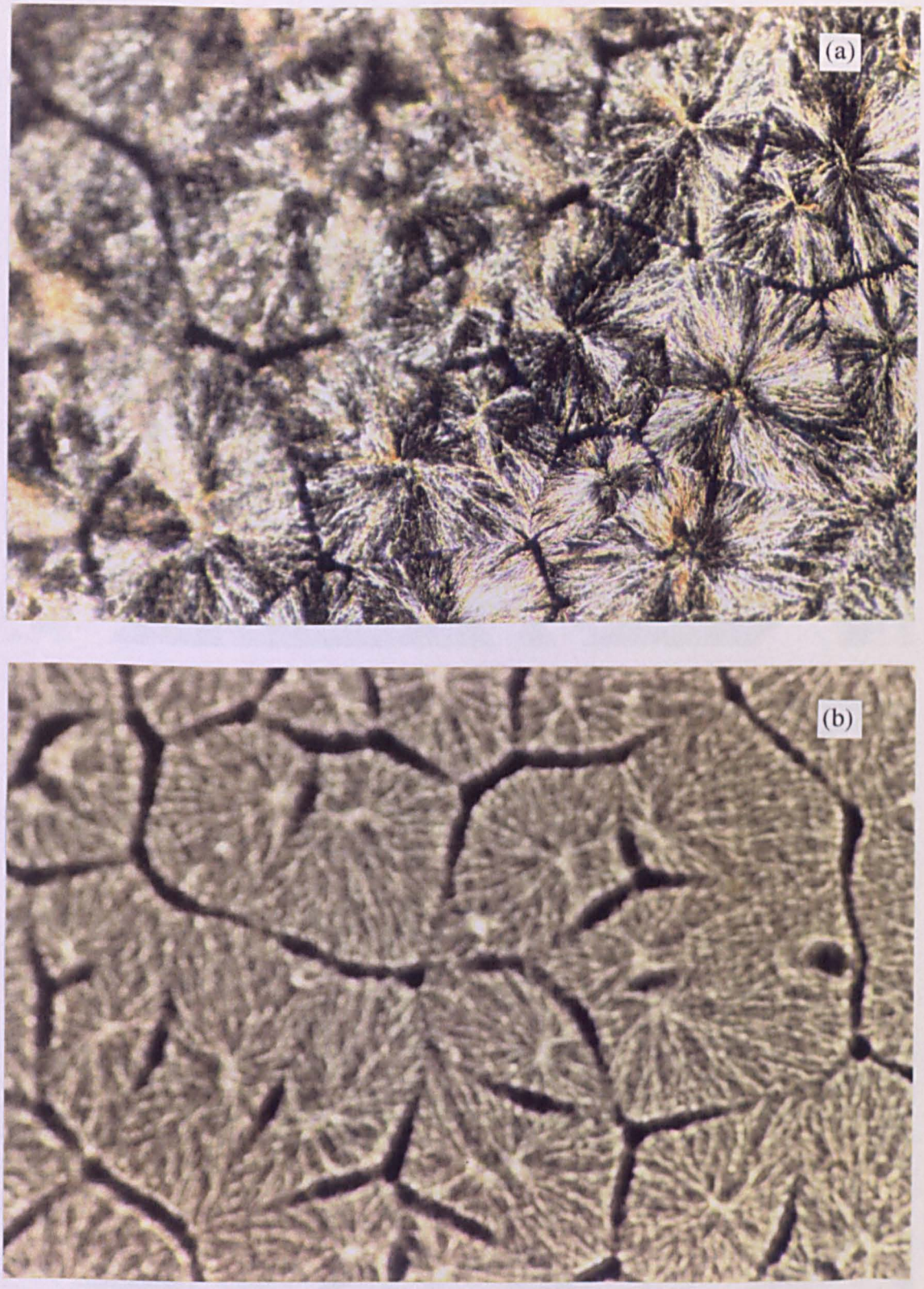

Figure 5.18 Micrographs of PEO_{5000}:$ZnBr_2$ at (a) 30°C and (b) 70°C

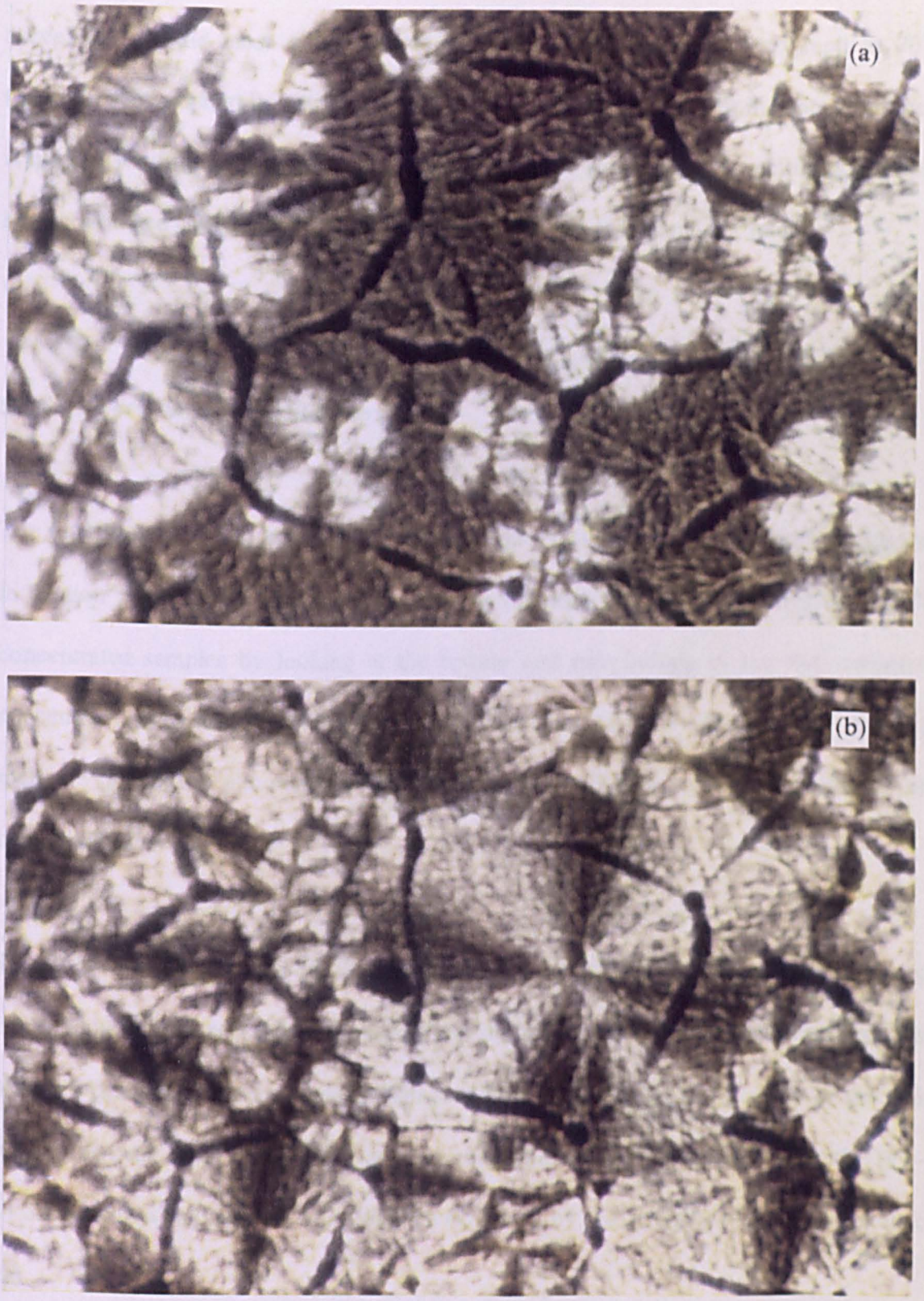

Figure 5.19 Micrographs of PEO_{5000}:$ZnBr_2$ crystallising at (a) 40°C and (b) 30°C

The micrographs of the samples studied show no evidence of high melting spherulites except for the the most dilute sample (n=5000). Although the micrograph at 70°C (n=5000) shows spherulitic structures but the d.s.c trace in Figure 5.13 indicated that there is no high melting spherulites. The presence might be due to the low melting spherulites have not melted completely at this temperature as indicated by the d.s.c. trace.

5.2.6 Overview of Ultradilute Systems

The ultradilute samples prepared appeared the same as the concentrated samples prepared in section 5.1. It is difficult to differentiate between the ultradilute samples and the concentrated samples by looking at the texture and morphology of the two ranges of concentrations. From the VTPM studies all the samples show both the low and high melting spherulites although in the DSC studies the high melting spherulites are unresolvable.

The XAFS studies carried out in the fluorescence mode for the concentration range prepared were quite succesful. They were less successful in looking at the intensities of the XANES peaks due to the relatively high background signals but slight shifts of the main absorption peak could still be detected. The absence of the pre-edge peak, due to the 1s ----> 3*d* transition, is obvious. This could be explained by the completely filled *d*-orbitals of Zn.

The EXAFS of the ultradilute samples is interesting in that there is a transition from the most concentrated sample in the ultradilute series, PEO_{1000}:$ZnBr_2$. The Zn - O interatomic distance is 1.965 Å with a coodination number of three. The rest of the samples in the series exhibit a shorter Zn - O interatomic distance decreasing with dilution, the shortest value noted is 1.930 Å. The oxygen coordination number for the rest of the series is 3 for the more dilute samples (n = 4000 and 5000) and 2 for the intermediate dilution (n = 2000 and 3000). The Br coordination is about 2.0 for the more concentrated samples (n = 1000, 2000 and 3000) and 1 for the more dilute samples (n = 4000 and 5000). The Zn-Br distance decreases with dilution, the longest interatomic distance is 2.40 Å and the shortest 2.35 Å. This suggests two different structural environments present in the series studied.

The Arrhenius plot is typical of semicrystalline polymer electrolytes where there is a change in gradient at the point where the polymer host melts; in the present studies this occurs at 68°C. The molar conductivity versus concentration plot is not quite the same as in liquid systems in that there is a maximum after which an abrupt fall follows. In liquid systems the molar conductivity increases with dilution and as the concentration gets very low the molar conductivity increases abruptly. This is due to ion association forming an ion atmosphere around the central ion, where the ion atmosphere has a net opposite charge to the central ion. It seems that in semi crystalline polymer electrolytes this phenomenon takes place only to a limited extent. Ion association occurs up to a certain limit such that the range is shorter than that in the liquid state.

The ionic conductivity of the most concentrated sample in the series, PEO_{1000}:$ZnBr_2$, is the highest in the series. It seems that there is a correlation between the local structure and the conductivity results in the present studies. The results suggest that the Zn - O coordination is the stronger determinant to conductivity than the Zn - Br coordination. It is suggested that the longer the Zn - O interatomic distance the more labile is the conducting species. This is supported further by the lower coordination number of the heteroatom on the polymer to the metal which increase the mobility of the conducting species. The influence of the length of the Zn - O interatomic distance on conductivity was also observed in the amorphous phase of the concentrated PEO_8:$ZnBr_2$ system, as discussed in section 5.1.

In the less concentrated samples in the series the metal to the polymer coordination is twice as that of the most concentrated sample. This high coordination suggests a lattice-type configuration rendering the conducting species less labile. The high Zn - O coordination also suggests the neutralising effect on the Zn resulting in a less positive centre. This might also be the reason for the single Br coordination.

6.0 Introduction

The iron systems were chosen in the present structure - conductivity studies due to the availabity of the two oxidation states of iron for comparative studies. The two oxidation states might also be useful in displaying the usefulness of XANES in the study of polymer electrolytes. The systems chosen in the studies are PEO_n:$FeBr_x$ (where n = 8, 20 and 50; and x = 2 and 3). In the low concentration, n = 50, and the concentrated samples, n = 8, air cast duplicates were also studied.

6.1 Materials and Preparation

The samples were prepared by the two solvent technique conducted in an argon recirculating dry box. The salts, anhydrous $FeBr_2$ and anhydrous $FeBr_3$ (both at 99.99% purity, supplied by Alfa Products), were dissolved separately in 25 ml of anhydrous ethyl alcohol (99% purity). The amount of salt needed for each composition was determined using the formula in section 5.1.1 is listed in table 6.1. These were then mixed with 75 ml of acetonitrile in 250 ml *quickfit* stoppered conical flasks with magnetic stirrers. 1 g of PEO was then slowly dissolved in each flask. The solutions were left to stir for 48 hours.

Table 6.1 Amount of $FeBr_2$ and $FeBr_3$ needed in the various compositions studied.

O:M Mole ratio	Mass of salt (gram)	
(n)	$FeBr_2$	$FeBr_3$
8	0.613	0.840
20	0.245	0.336
50	0.098	0.134

The polymer films were obtained by casting the resulting solutions in glass rings of 10 cm in diameter onto a sheet of PTFE. The solvent was allowed to evaporate in a dry box for a week. The resulting films were dried in a vacuum oven at 50°C for 48 hours and stored in sealed plastic sample bags in a desiccator.

There were a set of samples where the casting were done in air in the fume cupboard. The purpose of the study on this set is to see the effect of moisture at this stage of the preparation. The set comprised of PEO_8:$FeBr_x$, PEO_{20}:$FeBr_x$ and PEO_{50}:$FeBr_x$ (where x = 2 and 3). This set will be hereafter referred as 'air-cast' samples.

6.1.1 Results

The original salts were brown, the ferric salt being deeper in colour. On dissolution they give brown solutions of various shades, depending on the concentration. The colour ranges from reddish brown for the concentrated film to yellow for the ultradilute samples. The films after casting were quite brittle in texture. During drying at 50°C in the vacuum oven the films were soft and rubbery but after leaving in the desiccator for a while they became slightly brittle.

For the air-cast samples the same phenomenon took place but they were more brittle than the dry samples.

6.2 X-ray Absorption Fine Structure (XAFS) Studies

The samples chosen for XAFS studies were PEO_8:$FeBr_x$, PEO_{20}:$FeBr_x$ and PEO_{50}:$FeBr_x$ (x = 2 and 3) both for the air-cast and dry samples. For the PEO_8:$FeBr_x$ (x=2 and 3) dry samples, the effect of heat treatment was also studied. XAFS spectra were taken at room temperature (22°C), 70°C and again at room temperature after cooling from 70°C. The samples were mounted on the sample holders as described in section 3.1.2. The heating arrangement was the same as that with the zinc systems studied in section 5.1. Studies were done on station 7.1 at the SRS Daresbury, using the transmission mode with 50%

harmonic rejection for the K-edge spectra. The stored beam had an energy of 2.00 GeV and an average current of 190 mA.

6.2.1 XANES Results

In the XANES region of the present study there are three features worthy of attention; the pre-edge peak, the main absorption (white line) and a peak immediately after the main absorption peak (post-edge). The XANES spectra of the iron(II) systems are shown in Figure 6.1and 6.2, and the iron(III) systems in Figure 6.3 and 6.4.

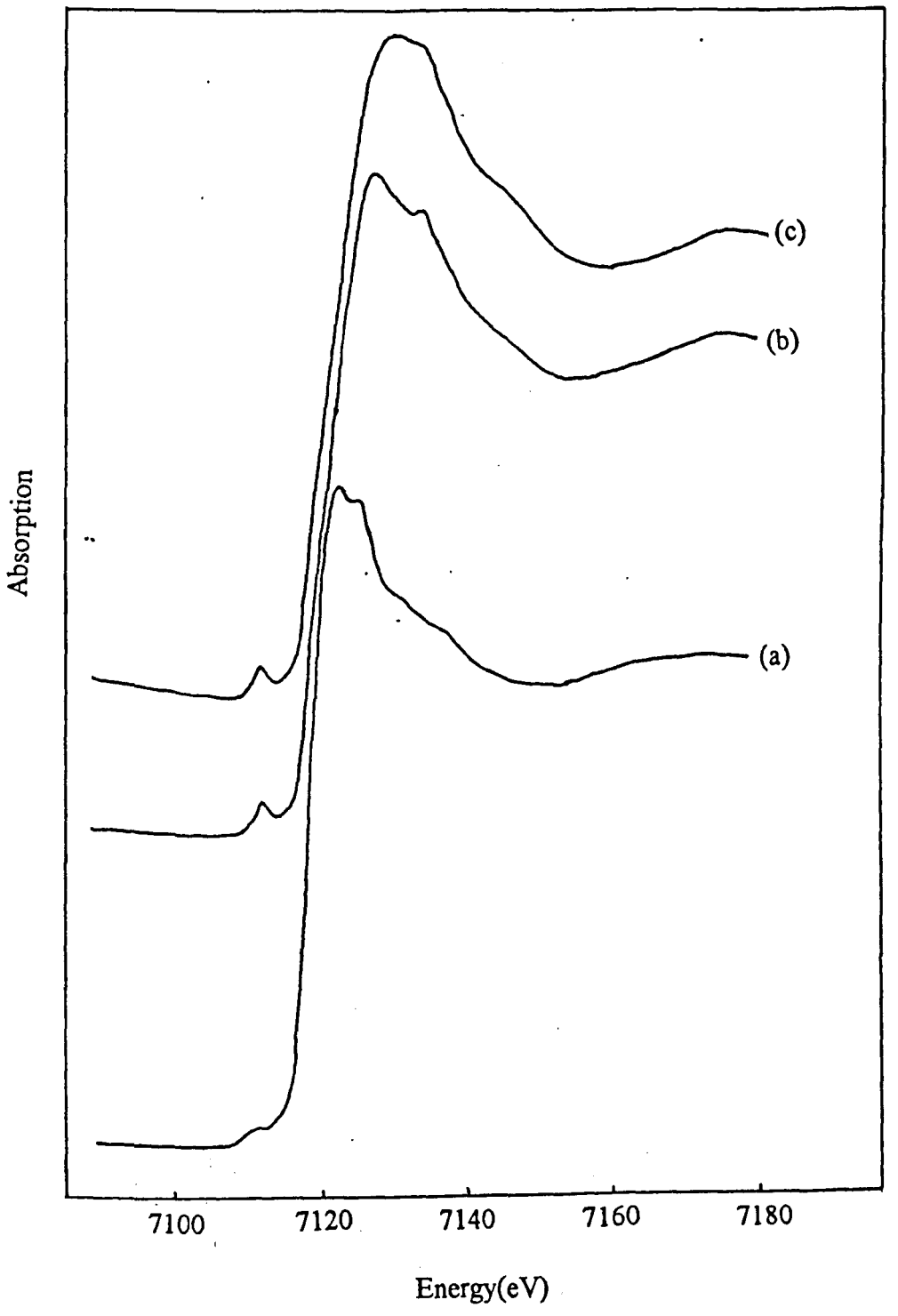

Figure 6.1 XANES of (a) $FeBr_2$, (b) PEO_8:$FeBr_2$ (air-cast), and (c) PEO_{50}:$FeBr_2$ (air-cast).

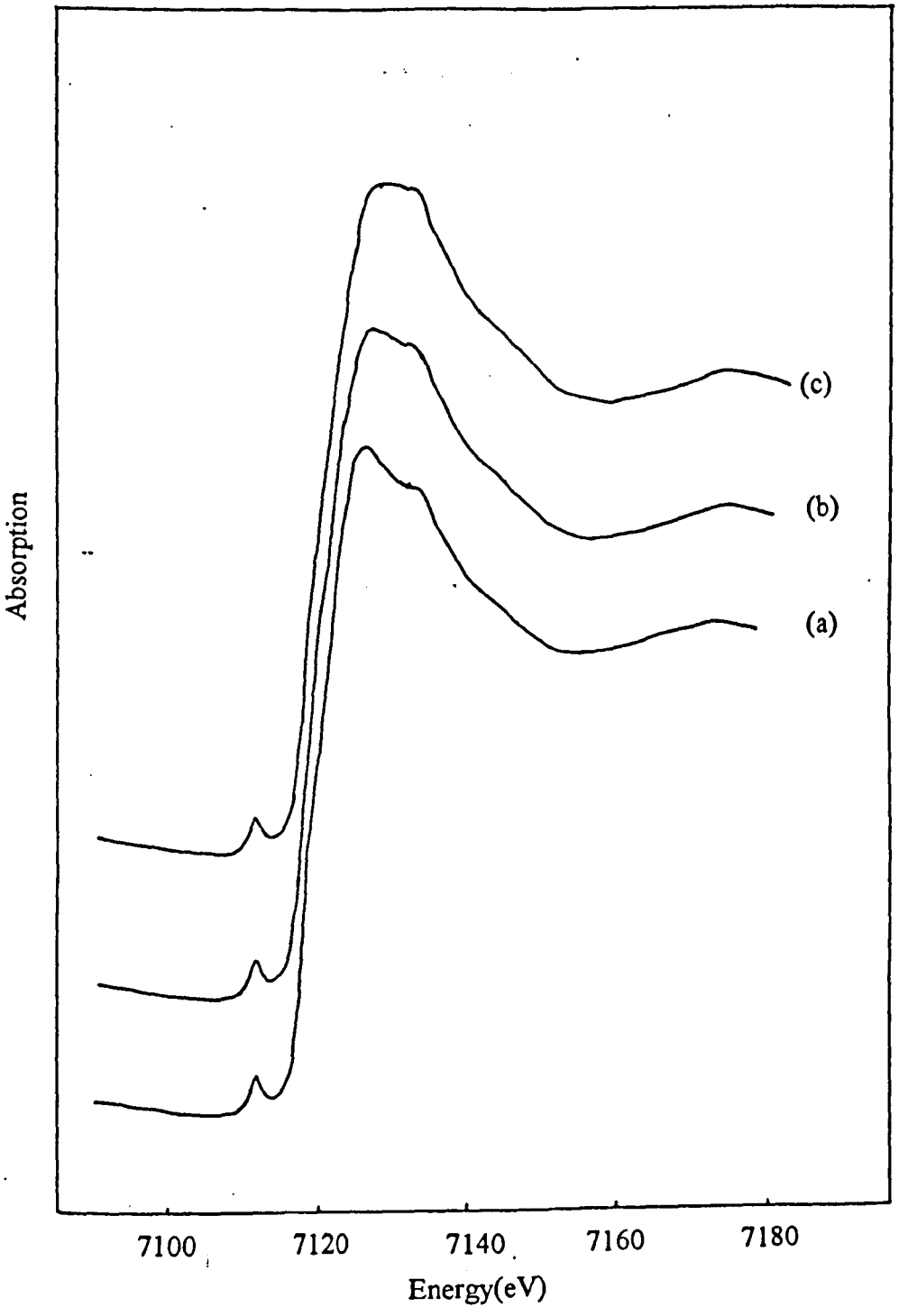

Figure 6.2 XANES of (a) PEO_8:$FeBr_2$ (dry-cast), (b) PEO_{20}:$FeBr_2$ (dry-cast) and (c) PEO_{50}:$FeBr_2$ (dry-cast)

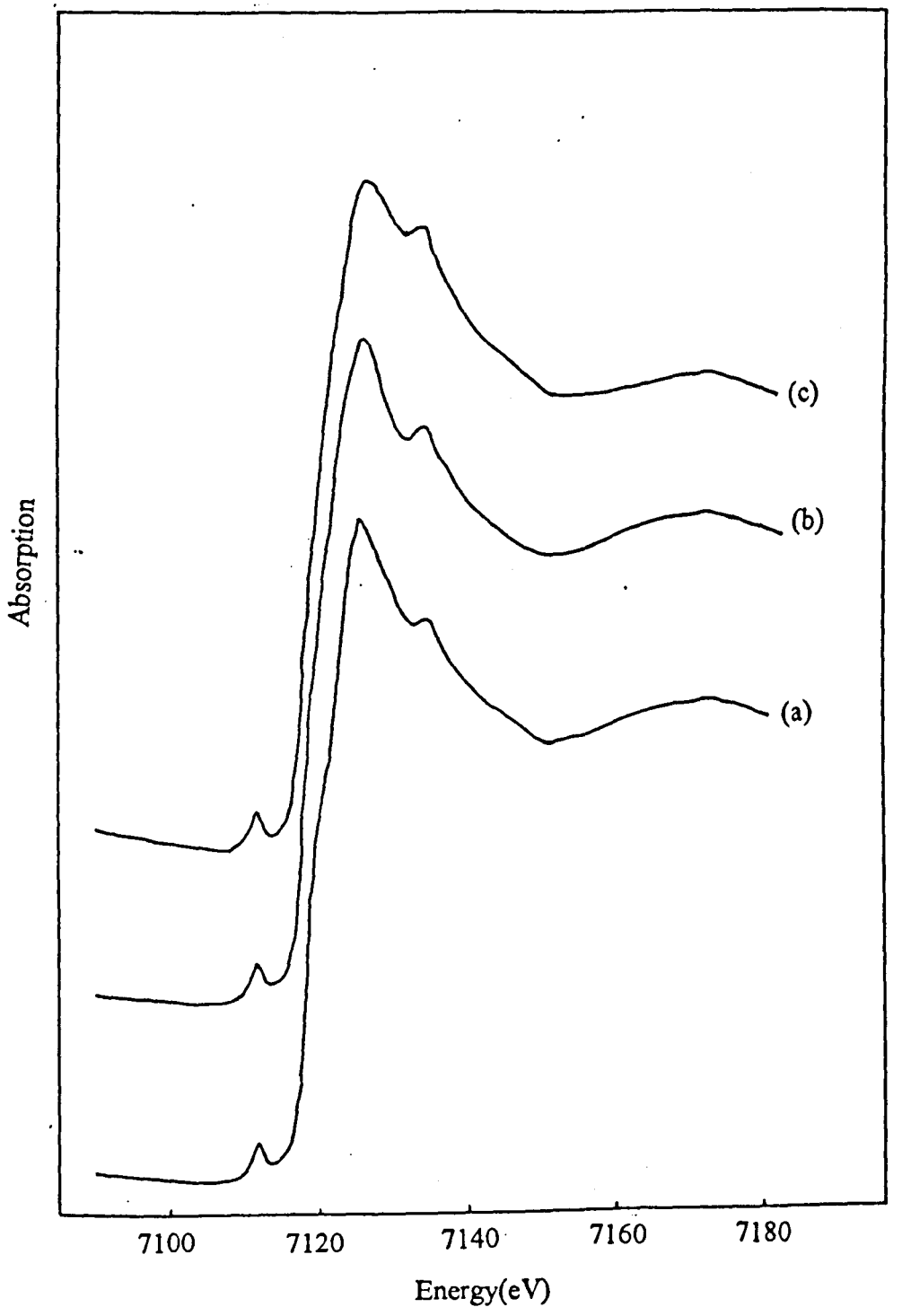

Figure 6.3 XANES of (a) $FeBr_3$, (b) PEO_8:$FeBr_3$ (air-cast), and (c) PEO_{50}:$FeBr_3$ (air-cast).

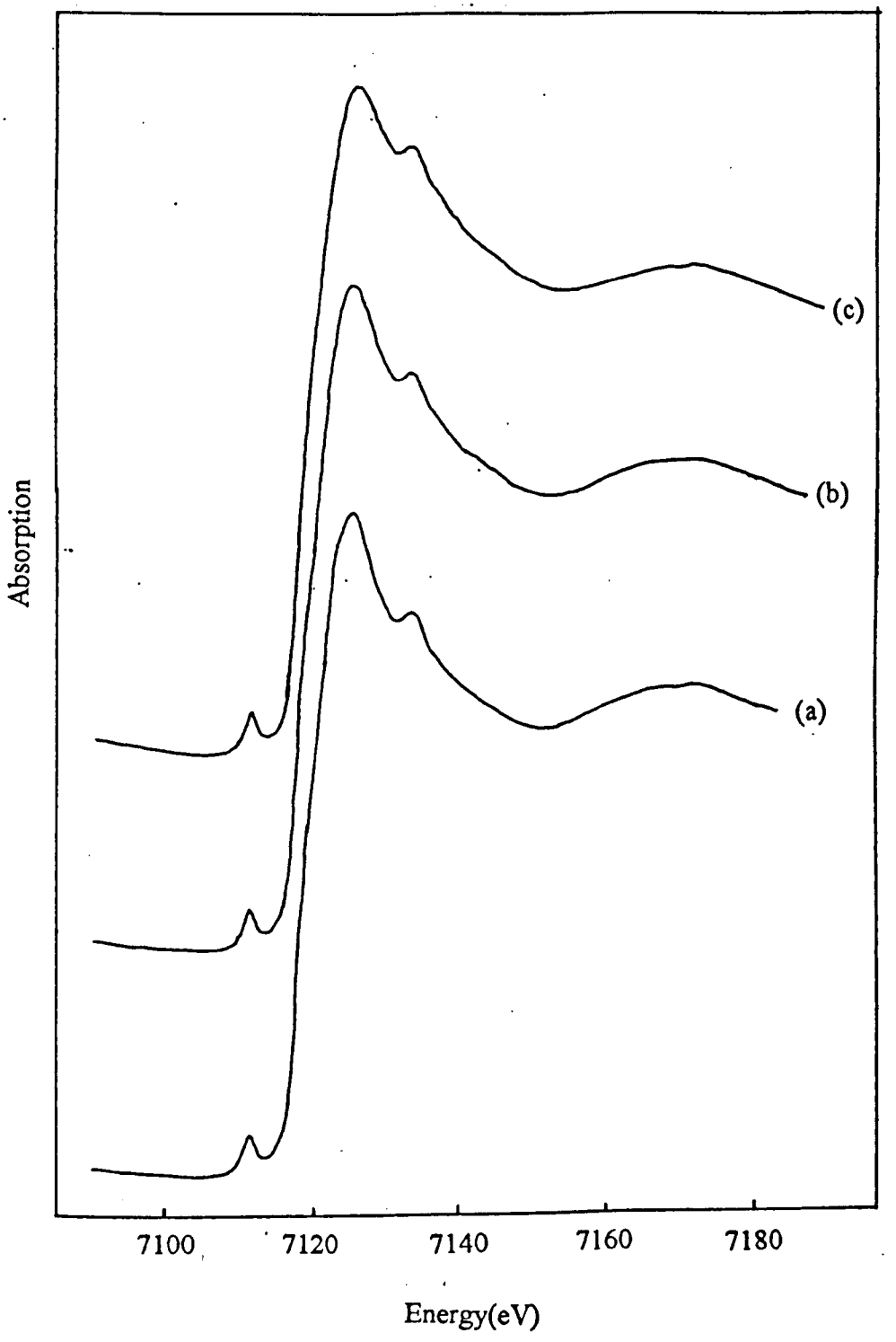

Figure 6.4 XANES of (a) PEO_8:$FeBr_3$ (dry-cast), (b) PEO_{20}:$FeBr_3$ (dry-cast) and (c) PEO_{50}:$FeBr_3$ (dry-cast).

The results of the XANES studies are tabulated in table 6.2.

Table 6.2 Peak positions in the XANES studies on the iron systems.

Samples	Positions (eV)		
	Pre-edge	White line	Post-edge
$FeBr_2$	7111.5	7122.7	7125.4
(Air cast)			
PEO_8:$FeBr_2$	7111.9	7127.4	7133.7
PEO_{50}:$FeBr_2$	7112.2	7130.0	7134.4
(Dry cast)			
PEO_8:$FeBr_2$	7111.9	7126.7	7133.3
PEO_{20}:$FeBr_2$	7111.9	7127.9	7133.3
PEO_{50}:$FeBr_2$	7111.9	7128.9	7133.3
$FeBr_3$	7112.2	7125.6	7134.1
(Air cast)			
PEO_8:$FeBr_3$	7112.2	7125.9	7134.4
PEO_{50}:$FeBr_3$	7113.0	7127.0	7134.4
(Dry cast)			
PEO_8:$FeBr_3$	7111.9	7125.6	7133.7
PEO_{20}:$FeBr_3$	7111.5	7125.6	7133.7
PEO_{50}:$FeBr_3$	7111.9	7125.9	7133.7

The pre-edge peak corresponding to the $1s$ -----> $3d$ transition appears at the same positions, within the limits of experimental error, in all the samples, including the model compounds. The only difference noticeable is the intensity of the transition. It appears that those in the Fe(III) samples are more intense than the Fe(II) samples especially in the model compounds.

The main absorption peak assigned to the $1s$ -----> $4p$ transition in the iron systems is more complex with respect to its position. There is no change in the position between the Fe(III) model compound and the Fe(III) dry cast samples. For the air-cast samples the dilute sample, PEO_{50}:$FeBr_3$, is at a higher position than the concentrated sample, PEO_8:$FeBr_3$, and the corresponding model compound by 1 eV. In the Fe(II) samples the positions are between 4 to 7 eV higher than the corresponding model compound. In the air-cast samples the concentrated sample, PEO_8:$FeBr_2$, is 4 eV higher than the model compound and the dilute sample, PEO_{50}:$FeBr_2$, is 7 eV higher than the model compound. In the dry samples, the concentrated sample, PEO_8:$FeBr_2$, is 4 eV higher than the model compound and the dilute sample, PEO_{50}:$FeBr_2$, is 6 eV higher than the model compound. The position of the peak for an intermediate concentration, PEO_{20}:$FeBr_2$, is 5 eV higher than the model compound. This phenomenon is not observable in the intermediate concentration of the Fe(III) system.

The position of the third peak, on the descent of the main absorption peak, is the same in all the samples except for the Fe(II) model compound which is 8 eV below the others. The intensity of the peak in the Fe(II) polymer systems seems to increase when the

concentration is more dilute. This is paricularly distinct in the dilute samples, PEO_{50}:$FeBr_2$, for both casting processes.

XANES spectra of PEO_8:$FeBr_x$ (x=2 and 3) dry samples at the various temperature is shown in Figure 6.5. The positions of the three peaks of concerned are listed in Table 6.3.

Table 6.3 Peak positions in the heat treatment studies on PEO_8:$FeBr_x$ (x=2 and 3).

Temperature	Peak Positions (eV)	
	PEO_8:$FeBr_2$	PEO_8:$FeBr_3$
22°C		
Pre-edge	7108.6	7108.6
White line	7124.8	7124.4
Post-edge	7131.0	7131.4
70°C		
Pre-edge	7108.6	7108.6
White line	7124.8	7122.4
Post-edge	7131.5	7131.5
Cooled 22°C		
Pre-edge	7110.3	7110.3
White line	7125.4	7122.4
Post-edge	7133.3	7133.3

The data of the dry samples at room temperature in Table 6.2 are not the same as in Table 6.3 because the samples are different. They are from the same batch but the experiments were done at a different time; the temperature related studies were three months later. Also the system could have changed with time (the white line of the Fe(II) and Fe(III) in the later experiments were about the same), because polymer electrolytes are kinetically controlled systems. Systems involving Fe(II) may be subject to oxidation and this is a further complication in addition to the morphological aspects of kinetic control. Care must be taken when interpreting the data as systems which are apparently based on Fe(II) may in fact be either Fe(III) or involve mixed oxidation states.

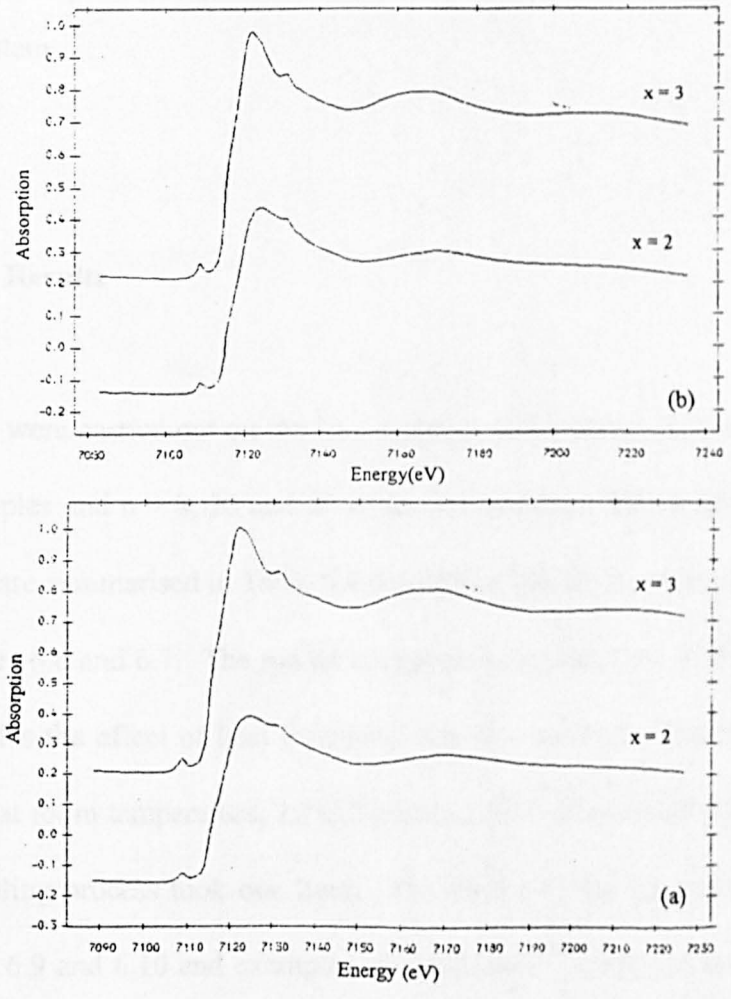

Figure 6.5 XANES spectra of PEO_8:$FeBr_x$ (x = 2 and 3) dry samples at (a) 22°C and (b) 70°C.

The pre-edge and post-edge of the Fe(II) and Fe(III) systems are at the same position irrespective of the temperature of the systems. The only difference in the position of peaks is for the white line. The position of the peak in the Fe(II) system is 2 eV higher than the Fe(III) system when the temperature of the systems is 22°C and 70°C but 3 eV higher when the samples were cooled from 70°C to 22°C.

Apart from the positions of the peaks, the spectra of the Fe(II) and Fe(III) systems can be distinguished by the shape. The intensity of the post-edge peak in the Fe(II) systems is more intense than the Fe(III) systems reflecting the difference in the local environment of each type of system.

6.2.2 EXAFS Results

EXAFS studies were carried out on the iron systems of the compositions n = 8 and 50 for the air-cast samples and n = 8, 20 and 50 of the dry samples. The results of the excurv92 fitting program are summarised in Table 6.4 through to Table 6.8; examples of the plots are shown in Figures 6.6 and 6.7. The model compounds chosen were $FeBr_2$ and $FeBr_3$. For the n = 8 samples the effect of heat treatment was also studied. The respective samples were examined at room temperature, 22°C, heated to 70°C and cooled to room temperature again. The cooling process took one hour. The results of the heat treatment studies are listed in Tables 6.9 and 6.10 and examples of the excurv92 plots are shown in Figure 6.8 and Figure 6.9.

Table 6.4a EXAFS results of iron model compounds.

Compounds	NNA	r (Å)	N	σ^2 (Å^2)	$E_o(eV)$	r (Å)	N
Experimental						Literature	
$FeBr_2$	Br	2.660	3.8	0.017	13.64	2.669*	4.0
$FeBr_3$	Br	2.352	3.2	0.018	11.93	2.36[+]	4.0

NNA= nearest neighbour atom; r= interatomic distance; N = coordination number; σ^2=Debye-Waller factor; E_o= difference between value at absorption edge energy from the experimental EXAFS spectrum and that found after data deconvolution.

* Inorganic Crystal Structure Database (Daresbury Laboratories)

[+] The Chemical Elements and their Compounds Vol.2 by Sidgwick, Oxford University Press, London, 1950, p.1356.

In the refinement procedure the *afac* value is 0.7 and *vpi* is -2.

Table 6.4b Literature Data of Fe_2O_3

EXAFS fit of the model compound Fe_2O_3 (Cole, 1996).

Shell	Nearest Neighbour	Coordination Number	Bond Distance	Debye-Waller Factor
1	O	3.0	1.936Å	0.012
2	O	3.0	2.094Å	0.021

Crystal structure data of Fe_2O_3 (Blake *et al.*,1966)

Shell	Nearest Neighbour	Coordination Number	Bond Distance
1	O	3.0	1.946Å
2	O	3.0	2.116Å

Table 6.5 EXAFS results of PEO_n:$FeBr_2$ (n = 8 and 50); (Air cast)

Sample PEO_n:$FeBr_2$	NNA	r (Å)	N	σ^2 (Å^2)	$E_o(eV)$
n = 8	O	2.14	2.6	0.015	12.38
	Br	2.32	2.7	0.008	
n = 50	O	2.06	1.6	0.015	8.96
	Br	2.33	1.7	0.008	

Table 6.6 EXAFS results of PEO_n:$FeBr_3$ (n = 8 and 50); (Air cast)

Sample PEO_n:$FeBr_3$	NNA	r (Å)	N	σ^2 (Å^2)	$E_o(eV)$
n = 8	O	2.07	1.8	0.019	9.83
	Br	2.33	1.9	0.007	
n = 50	O	2.06	2.0	0.019	9.39
	Br	2.32	1.7	0.008	

NNA= nearest neighbour atom; r= interatomic distance; N = coordination number; σ^2=Debye-Waller factor; E_o= difference between value at absorption edge energy from the experimental EXAFS spectrum and that found after data deconvolution.

In the refinement procedure the *afac* value is 0.7 and *vpi* is -2.

Table 6.7 EXAFS results of PEO_n:$FeBr_2$ (n = 8, 20 and 50); (Dry cast)

Sample PEO_n:$FeBr_2$	NNA	r (Å)	N	σ^2 (Å^2)	$E_o(eV)$
n = 8	O	2.15	2.9	0.021	12.32
	Br	2.32	2.8	0.007	
n = 20	O	2.15	3.1	0.031	11.36
	Br	2.32	2.7	0.007	
n = 50	O	2.13	2.6	0.024	11.30
	Br	2.32	2.7	0.007	

Table 6.8 EXAFS results of PEO_n:$FeBr_3$ (n = 8, 20 and 50); (Dry cast)

Sample PEO_n:$FeBr_3$	NNA	r (Å)	N	σ^2 (Å^2)	$E_o(eV)$
n = 8	O	2.09	3.3	0.032	11.20
	Br	2.32	2.4	0.008	
n = 20	O	2.07	3.6	0.035	10.74
	Br	2.32	2.5	0.008	
n = 50	O	2.06	3.5	0.033	9.03
	Br	2.33	2.5	0.008	

NNA= nearest neighbour atom; r= interatomic distance; N = coordination number; σ^2=Debye-Waller factor; E_o= difference between value at absorption edge energy from the experimental EXAFS spectrum and that found after data deconvolution. In the refinement procedure the *afac* value is 0.7 and *vpi* is -2.

Table 6.9 EXAFS results of PEO_8:$FeBr_2$ at various temperatures.

Temperature (°C)	NNA	r (Å)	N	σ^2 (Å^2)	$E_0(eV)$
22	O	2.19	3.1	0.021	12.32
	Br	2.32	2.7	0.006	
70	O	2.20	3.4	0.031	11.84
	Br	2.32	2.4	0.006	
22	O	2.19	3.2	0.022	12.45
	Br	2.32	2.7	0.006	

NNA= nearest neighbour atom; r= interatomic distance; N = coordination number; σ^2=Debye-Waller factor; E_0= difference between value at absorption edge energy from the experimental EXAFS spectrum and that found after data deconvolution. In the refinement procedure the *afac* value is 0.7 and *vpi* is -2.

Table 6.10 EXAFS results of PEO_8:$FeBr_3$ at various temperatures.

Temperature (°C)	NNA	r (Å)	N	σ^2 (Å^2)	E_o(eV)
22	O	2.11	3.4	0.042	11.39
	Br	2.32	2.7	0.008	
70	O	2.12	1.9	0.035	11.22
	Br	2.32	2.4	0.009	
22	O	2.11	3.3	0.040	11.43
	Br	2.32	2.8	0.008	

NNA= nearest neighbour atom; r= interatomic distance; N = coordination number; σ^2=Debye-Waller factor; E_o= difference between value at absorption edge energy from the experimental EXAFS spectrum and that found after data deconvolution. In the refinement procedure the *afac* value is 0.7 and *vpi* is -2.

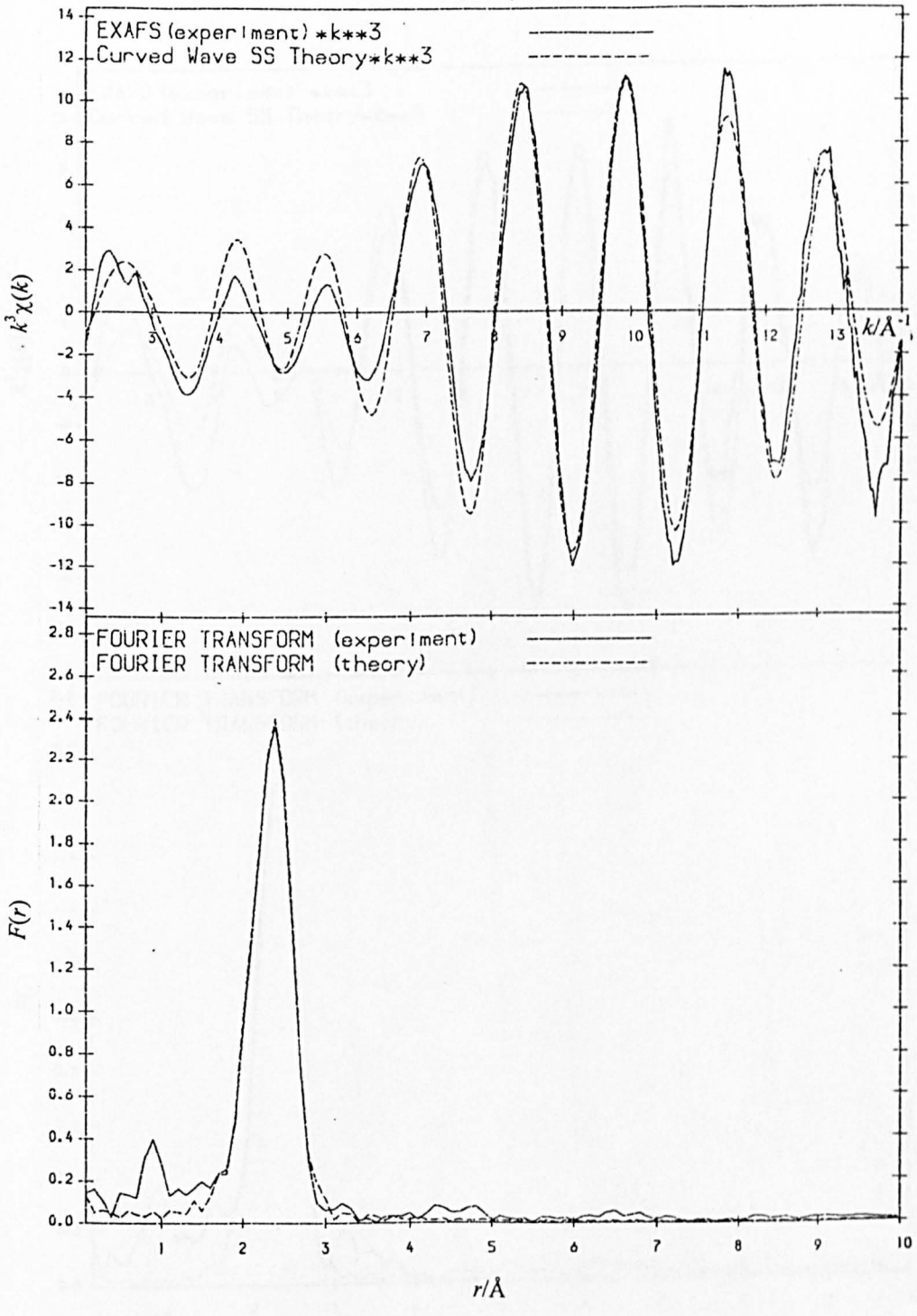

Figure 6.6 *Excurv92* plot of PEO_{20}:$FeBr_2$ dry sample.

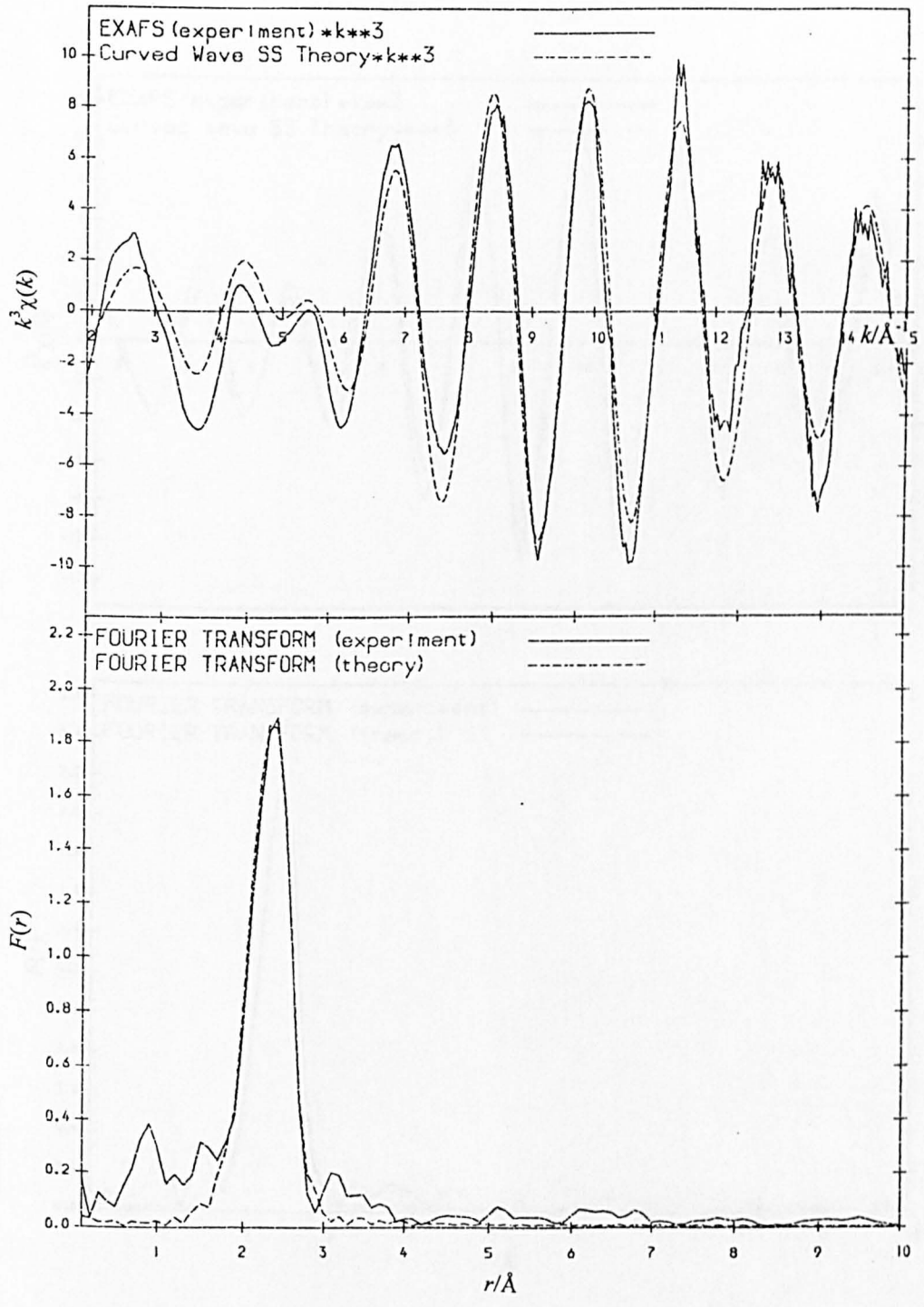

Figure 6.7 *Excurv92* plot of PEO_{20}:$FeBr_3$ dry sample.

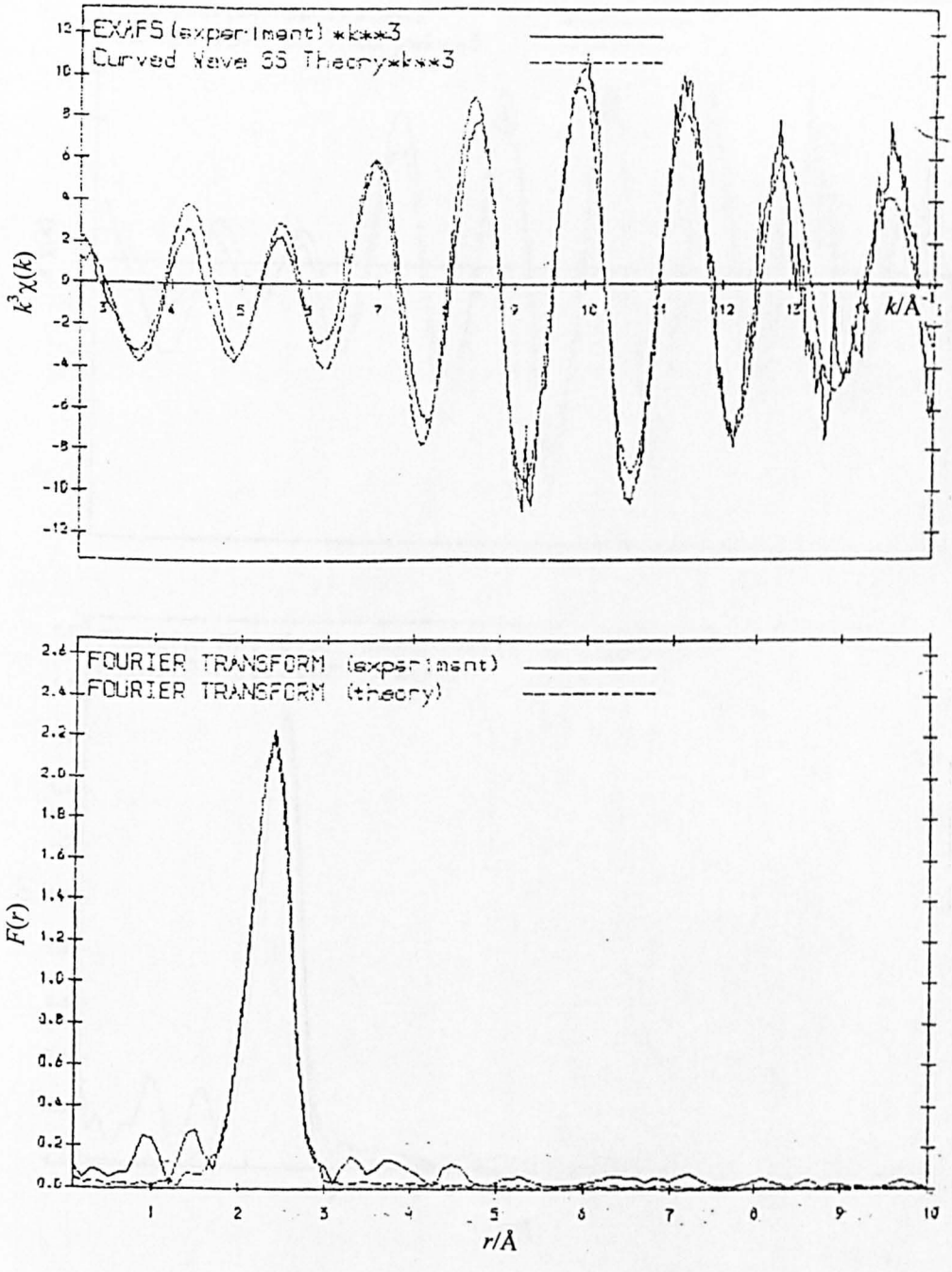

Figure 6.8 *Excurv92* plot of PEO_8:$FeBr_2$ dry sample at 70°C.

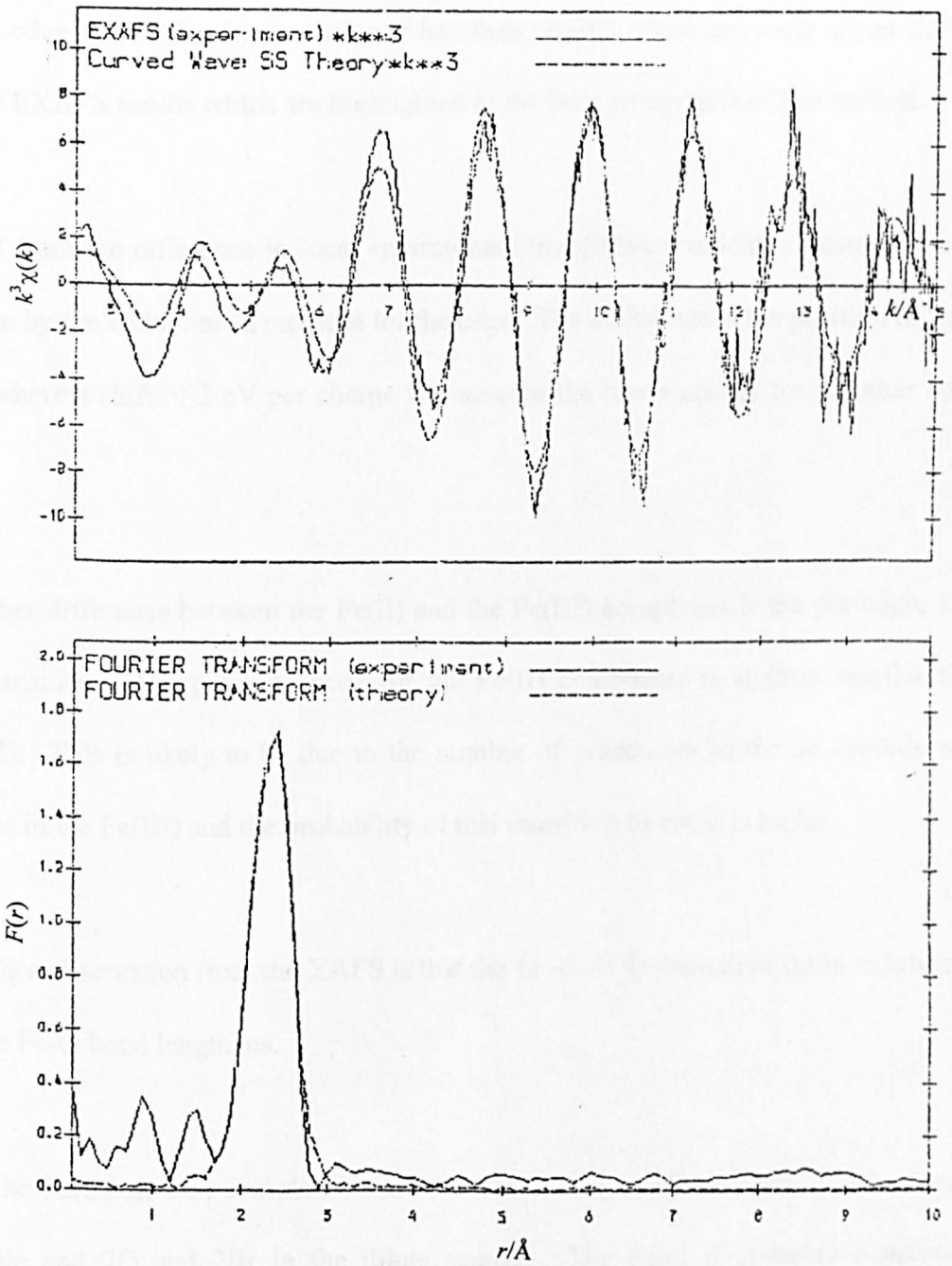

Figure 6.9 *Excurv92* plot of PEO_8:$FeBr_3$ dry sample at 70°C.

6.2.3 Comments on Results

The XANES studies suggest that different local environments may result in different shape at the edge, especially the post-edge at less than 50 eV. There are some minor differences in the EXAFS results which are highlighted in the later paragraphs of this section.

Apart from the difference in local environment the different oxidation state of the iron is shown by the white line, a measure for the edge. The difference is the position of the white line where a shift of 2 eV per charge was seen in the lower energy for a higher oxidation state.

Another difference between the Fe(II) and the Fe(III) complexes is the pre-edge, $1s$ -----> $3d$ transition. The pre-edge peak for the Fe(II) complexes is slightly smaller than the Fe(III). This is likely to be due to the number of vacancies in the $3d$ orbitals which is higher in the Fe(III) and the probability of this transition to occur is higher.

Another observation from the XAFS is that the $1s$ -----> $4p$ transition shifts to lower energy as the Fe-O bond lengthens.

For the Fe(II) air cast complexes the Fe is cordinated to 3O and 3Br in the concentrated sample and 2O and 2Br in the dilute sample. The Fe-O interatomic distance in the concentrated sample is longer than the dilute sample by 0.08Å. The Fe-Br interatomic distances are not significantly different.

concentrated sample is longer than the dilute sample by 0.08Å. The Fe-Br interatomic distances are not significantly different.

For the Fe(III) air cast complexes the Fe is coordinated to 2O and 2Br irrespective of concentration. The Fe-O and Fe-Br distances also do not change significantly with concentration.. The dilute Fe(II) sample resembles the Fe(III) sample.

For the dry samples in both Fe(II) and Fe(III), the Br and O coordinations are about the same at 3 each although the O coordination in Fe(III) shows an intermediate value of 2.5. The Fe-O and Fe-Br interatomic distances follow the same trend as in the air cast samples at the respective values of 2.09Å and 2.32Å for Fe(III) concentrated sample and 2.06Å and 2.33Å for the dilute samples. For the Fe(II) samples the concentrated and dilute samples the Fe-O interatomic distance is 2.15Å and 2.13Å respectively. The Fe-Br interatomic distance is 2.32Å for both the concentrations studied.

The data in Tables 6.9 and 6.10 pertain to an older aliquots of the samples used in the measurements reported in Tables 6.7 and 6.8. In the EXAFS studies at various temperatures of the concentrated samples the Fe-O interatomic distances for Fe(II) and Fe(III) at 70°C are slightly higher than that at 20°C. For both the Fe(II) and Fe(III) systems the difference is 0.01Å. The Fe-Br interatomic distance remains the same for both systems at the two studied temperatures.

6.3 Conductivity Studies

Conductivity studies were carried out employing the a.c impedance technique as described in section 3.2. The shape of the impedance spectra varies with the composition, temperature and type of samples. The impedance spectra obtained for the iron samples are peculiar. The iron(II) samples exhibit the typical semicircle spike type of spectra (exemplary of polymer electrolytes) with a prominent large semicircle for low temperature spectra to a conspicuous spike at higher temperatures as illustrated in Figure 6.10.

For the iron(III) samples the impedance spectra at low temperatures, less than the melting point of the low melting spherulites, show a double semicircle. The second semicircle disappears as the temperature reaches the melting point of the low melting spherulites. This phenomenon could be observed in all the iron(III) samples studied as can be seen for example in Figure 6.11.

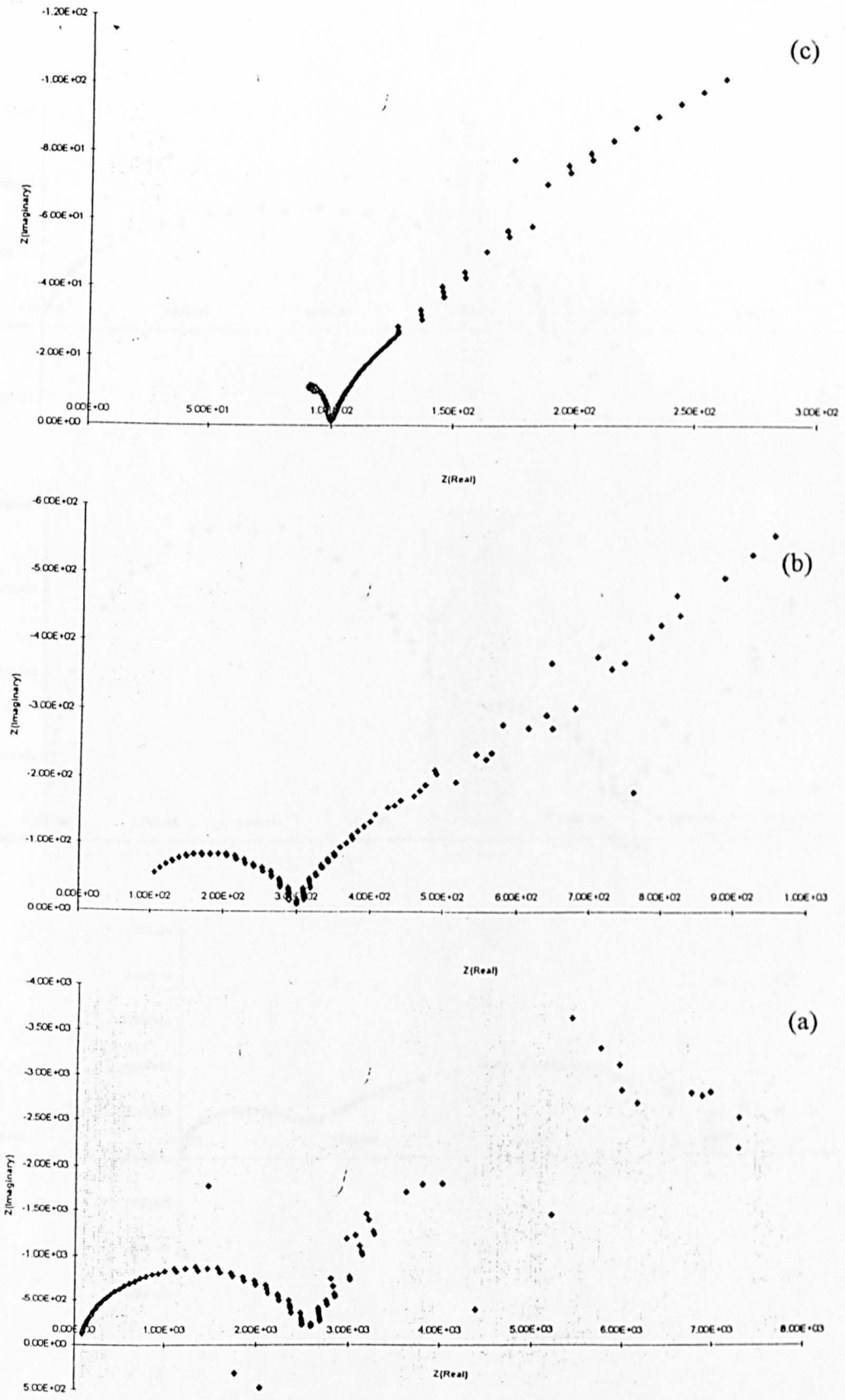

Figure 6.10 Impedance spectra of PEO_8:$FeBr_2$ at (a) 40 °C, (b) 70 °C and (c)100 °C.

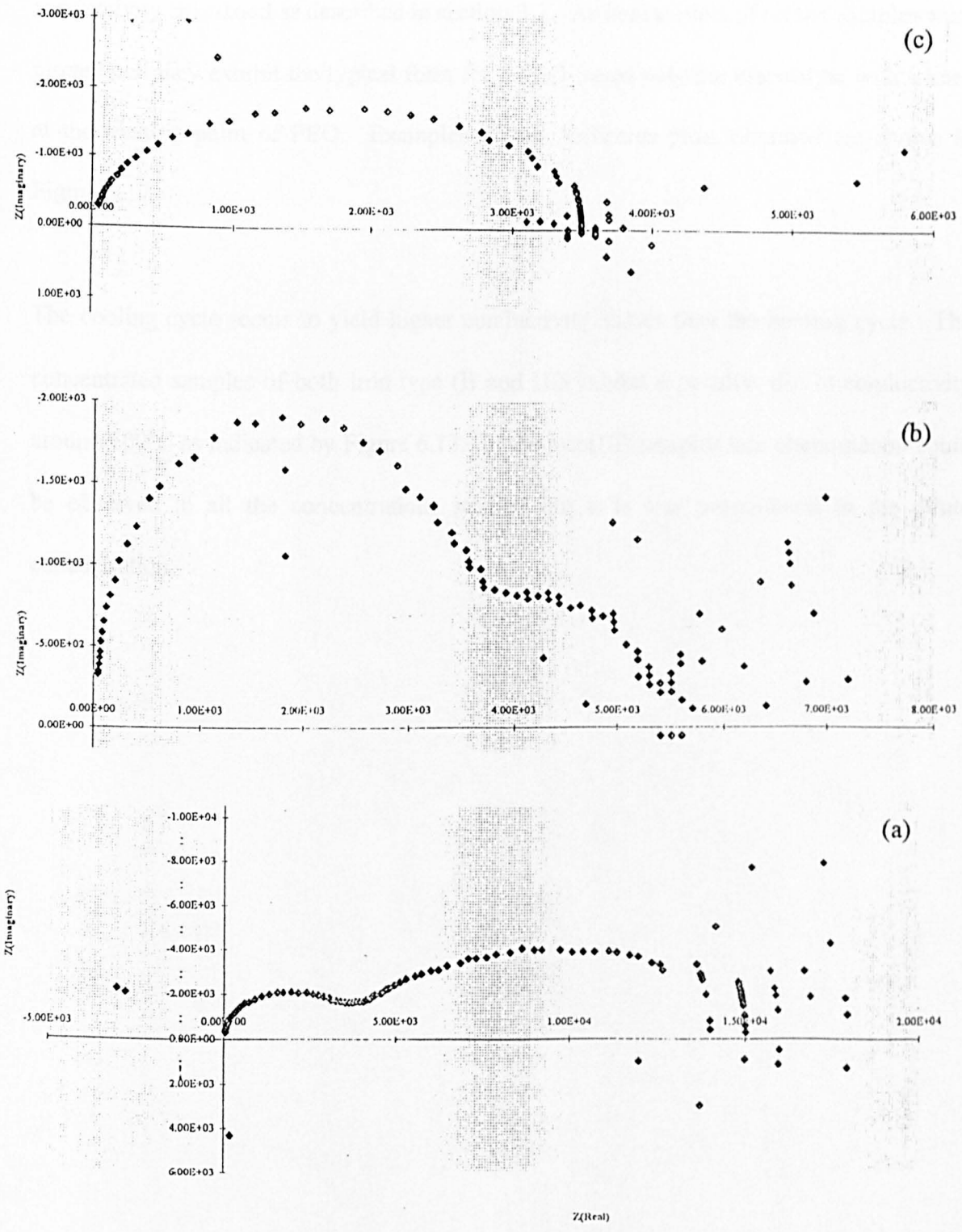

Figure 6.11 The impedance spectra of PEO_8:$FeBr_3$ at (a) 40°C, (b) 50°C and 70°C.

From the impedance spectra of the samples the resistances are evaluated and the conductivity calculated as described in section 3.2. Arrhenius plots of all the samples were plotted and they exhibit the typical form for a PEO-based polymer electrolyte with a knee at the melting point of PEO. Examples of the Arrhenius plots obtained are shown in Figure 6.12.

The cooling cycle seems to yield higher conductivity values than the heating cycle. The concentrated samples of both iron type (II and III) exhibit a peculiar dip in conductivity around 100°C as indicated by Figure 6.13. In the iron(III) samples this phenomenon could be observed in all the concentrations studied but it is less pronounced in the dilute concentration.

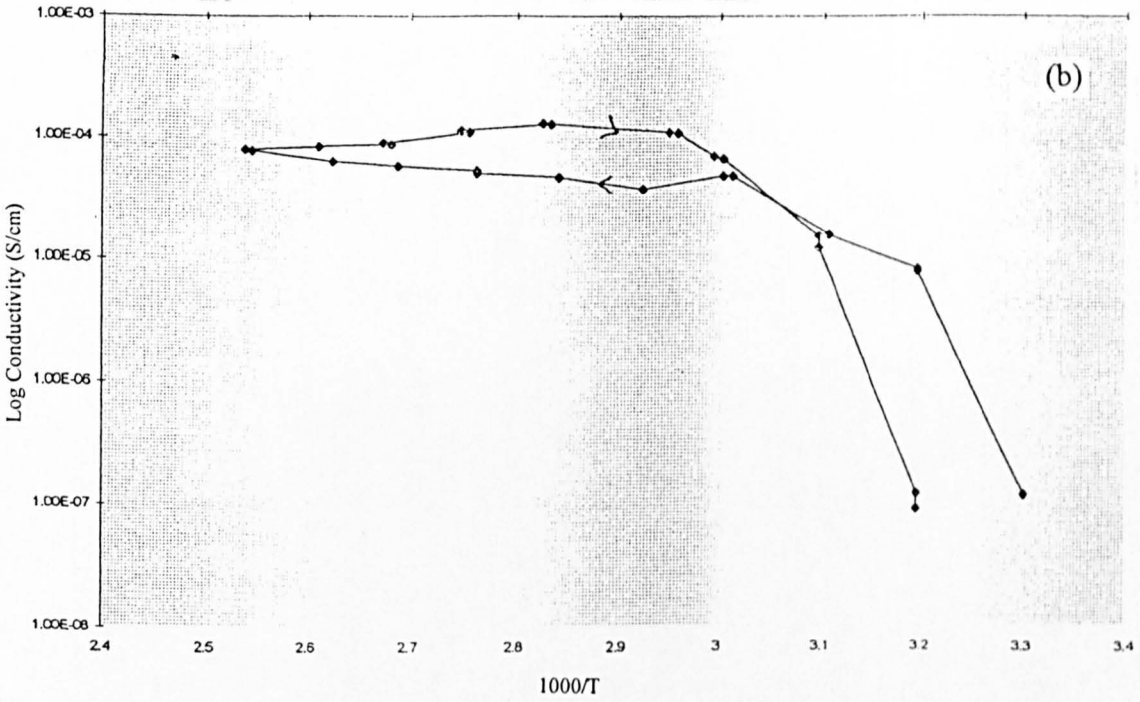

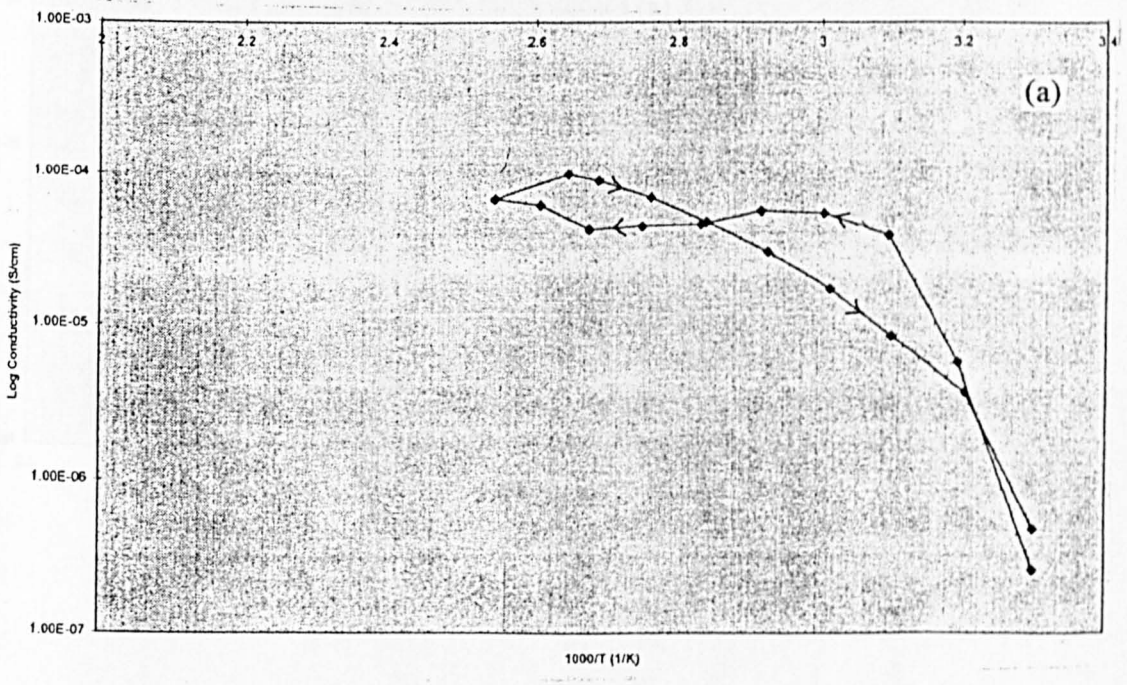

Figure 6.12 Arrhenius plots of (a) PEO_8:$FeBr_2$ (Dry sample) and (b) PEO_{20}:$FeBr_2$ (Air-cast sample).

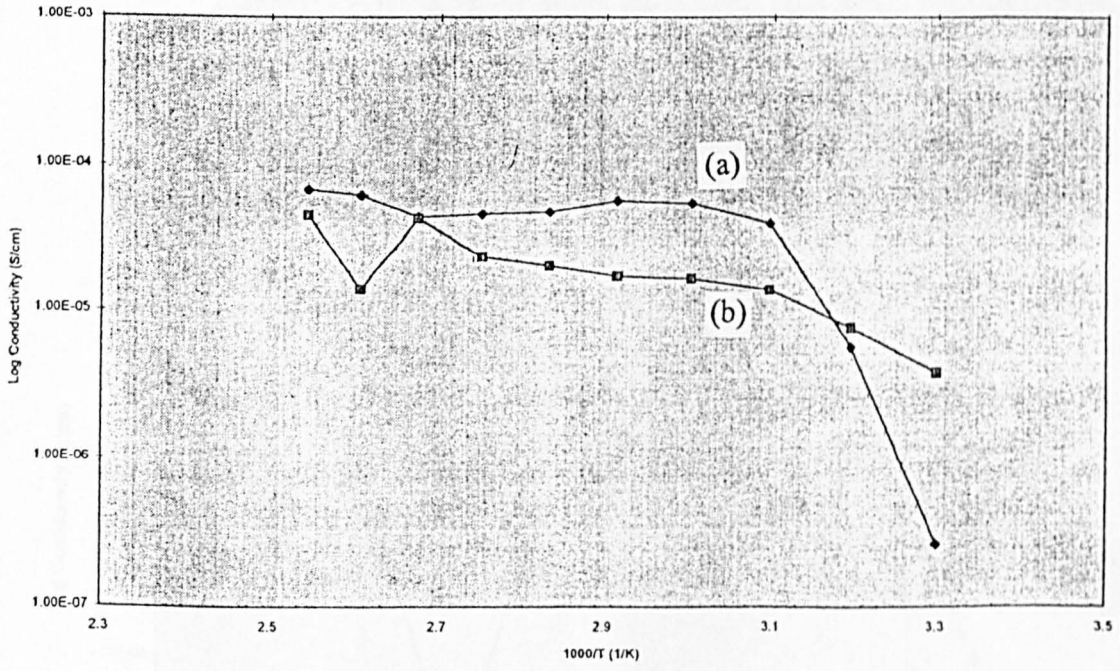

Figure 6.13 Arrhenius plots of (a) PEO_8:$FeBr_2$ (Dry sample) and (b) PEO_8:$FeBr_3$ (Dry sample).

Another anomaly is the Arrhenius plot for PEO_8:$FeBr_2$ air-cast sample where in the cooling cycle the conductivity values remain roughly the same at a high value after an initial dip. This phenomenon was not observed for the dry-cast sample as shown in Figure 6.14.

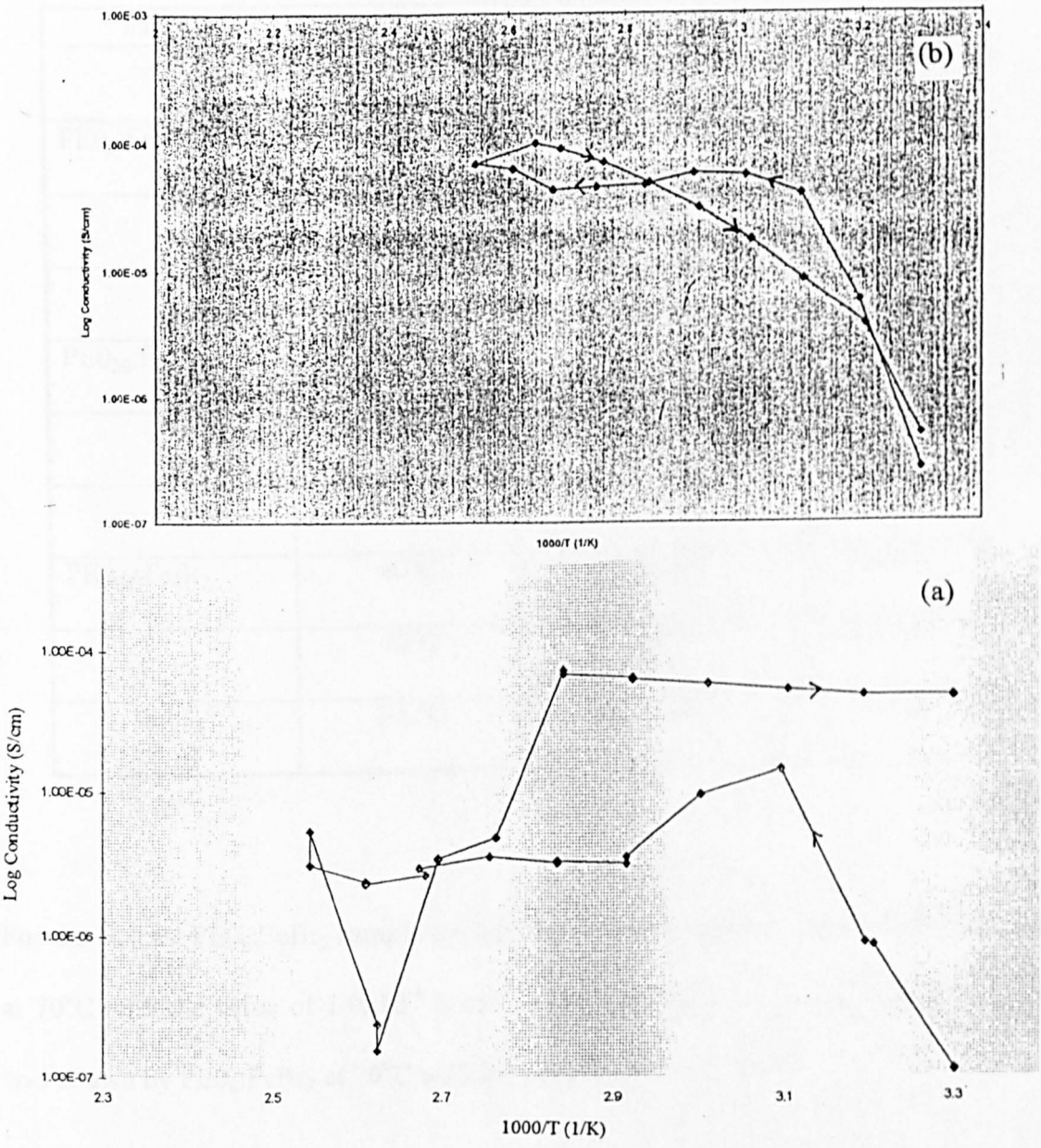

Figure 6.14 Arrhenius plots of (a) PEO_8:$FeBr_2$ (air-cast) and (b) PEO_8:$FeBr_2$ (dry-cast).

The conductivity values of the iron samples vary with composition and casting procedure. The conductivity values of PEO_n:$FeBr_2$ are listed in Table 6.11.

Table 6.11 Conductivity values of PEO_n:$FeBr_2$ at different temperatures.

Sample	Temperature	Conductivity (S cm^{-1})	
		Air-cast	Dry-cast
PEO_8:$FeBr_2$	40°C	$8.9x10^{-7}$	$5.0x10^{-6}$
	70°C	$3.4x10^{-6}$	$5.6x10^{-5}$
	100°C	$2.9x10^{-6}$	$4.3x10^{-5}$
PEO_{20}:$FeBr_2$	40°C	$1.1x10^{-7}$	$2.5x10^{-6}$
	70°C	$1.0x10^{-4}$	$3.0x10^{-6}$
	100°C	$8.2x10^{-5}$	$2.8x10^{-6}$
PEO_{50}:$FeBr_2$	40°C	$2.1x10^{-6}$	$2.3x10^{-7}$
	70°C	$1.0x10^{-5}$	$6.9x10^{-7}$
	100°C	$1.4x10^{-5}$	$1.3x10^{-7}$

For the air-cast PEO_n:$FeBr_2$ sample the highest conductivity was exhibited by PEO_{20}:$FeBr_2$ at 70°C with the value of $1.0x10^{-4}$ S cm^{-1}, while for the dry-cast counterpart the highest was shown by PEO_8:$FeBr_2$ at 70°C with the value of $5.6x10^{-5}$ S cm^{-1}.

For the iron(III) samples the conductivity values are listed in Table 6.12.

Table 6.12 Conductivity values of PEO_n:$FeBr_3$ at different temperatures.

Sample	Temperature	Conductivity (S cm^{-1})	
		Air-cast	Dry-cast
PEO_8:$FeBr_3$	40°C	$9.7x10^{-7}$	$7.5 x10^{-6}$
	70°C	$2.3x10^{-5}$	$1.7x10^{-5}$
	100°C	$1.8x10^{-5}$	$4.2x10^{-5}$
PEO_{20}:$FeBr_3$	40°C	$3.6x10^{-7}$	$2.0x10^{-6}$
	70°C	$4.2x10^{-5}$	$6.9x10^{-6}$
	100°C	$1.2x10^{-5}$	$1.8x10^{-5}$
PEO_{50}:$FeBr_3$	40°C	$2.0x10^{-7}$	$5.3x10^{-7}$
	70°C	$1.4x10^{-4}$	$1.5x10^{-5}$
	100°C	$2.1x10^{-4}$	$1.6x10^{-5}$

The highest conductivity value shown by the iron(III) air-cast sample is PEO_{50}:$FeBr_3$ at 100°C with the value of $2.1x10^{-4}$ S cm^{-1} and for the dry-cast sample it was exhibited by PEO_8:$FeBr_3$ at 100°C with the value of $4.2x10^{-5}$ S cm^{-1}.

6.3.1 Comments on Results

In polycrystalline solids, transport properties are strongly affected by microstructure, and impedance spectra usually contain features that can be directly related to microstructure. Some of the microstructural features that may be inferred are grains and grain boundaries (Bonanos et. al, 1984). Figure 6.11 is an example of an impedance spectrum showing the grain boundary effect. At low temperature the resistivity can be dominated by the grain boundaries, shown by the larger size of the second semicircle. At higher temperatures the grain boundary contribution is minimised. It has also been reported that the double semicircle is due to charge transfer processes but, the fact that it only appears at low temperatures (below the melting point of the low melting spherulites) and is confined to the iron(III) systems, means that this process is not likely to dominate. There are also cases where the grain boundary response is lacking due to reorientation of the crystals, known as twinning, in a single crystal (Bonanos and Butler, 1985). The grain boundary arc is also sometimes absent in polycrystalline ceramics (Slowtwinski et. al, 1985) and they suggested that finely twinned crystallites along the substantial lengths of grain boundary effectively eliminate the grain boundary impedance. Thus, it is suggested that grain boundary impedance is not a significant contribution in the iron(II) systems.

All the iron samples studied exhibit the characteristic PEO-based polymer electrolytes Arrhenius plot; a knee at the melting temperature of the polymer. This suggests that the iron samples studied contain a mixed crystalline-amorphous morphology.

The conductivity of the iron samples depends very much on the composition and preparation conditions. The air-cast samples show little, if any, trends in conductivities. In the iron(II) systems, for example, the highest conductivity recorded was at an intermediate temperature, 70°C, of an intermediate composition, PEO_{20}:$FeBr_2$. Whereas, in the iron(III) systems the highest conductivity was recorded for a more dilute composition, PEO_{50}:$FeBr_2$, at the highest temperature studied, 100°C. For a given composition the conductivity of the iron(II) and iron(III) systems increases with temperature, as in PEO_8:$FeBr_x$ (x=2 nd 3); or can increase to a maximum value and down again, as in PEO_{20}:$FeBr_x$ (x=2 and 3).

In the dry samples the conductivity trend is clearer. For both the iron(II) and iron(III) systems the highest conductivity was exhibited by the concentrated samples, PEO_8:$FeBr_x$ (x=2 and 3); the highest being the iron(II) system. The temperature dependence of conductivity is different in the two systems. In the iron(II) systems the conductivity is maximum at 70°C for all concentrations, whereas in the iron(III) systems the conductivity is maximum at 100°C. Of the two systems the conductivity of the iron(II) system is higher than the iron(III) system at high concentration and at lower concentration the opposite applies.

6.4 Differential Scanning Calorimetry (DSC) Studies

DSC studies were carried out on all the iron samples, $PEO_n:FeBr_x$ (n = 8, 20 and 50; x = 2 and 3) air-cast and dry, to identify the phases and transition temperatures. The experimental technique is outlined in detail in section 3.3. The DSC traces of the concentrated and intermediate dry samples are shown in Figure 6.15 and 6.16 respectively. The DSC traces of the concentrated and intermediate concentrations air-cast samples are shown in Figure 6.17 and 6.18 respectively. The DSC traces for the dilute samples for all the systems look alike and an example is shown in Figure 6.19.

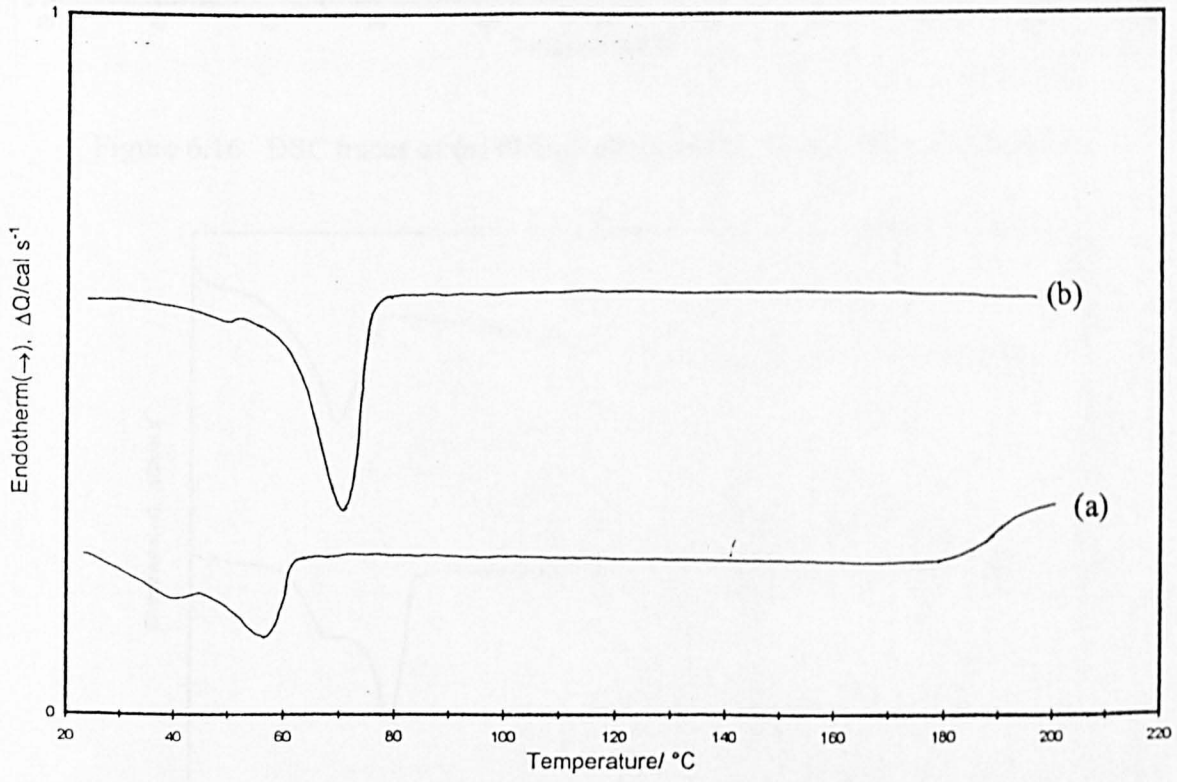

Figure 6.15 DSC traces of (a) $PEO_8:FeBr_2$ and (b) $PEO_{20}:FeBr_2$ dry samples.

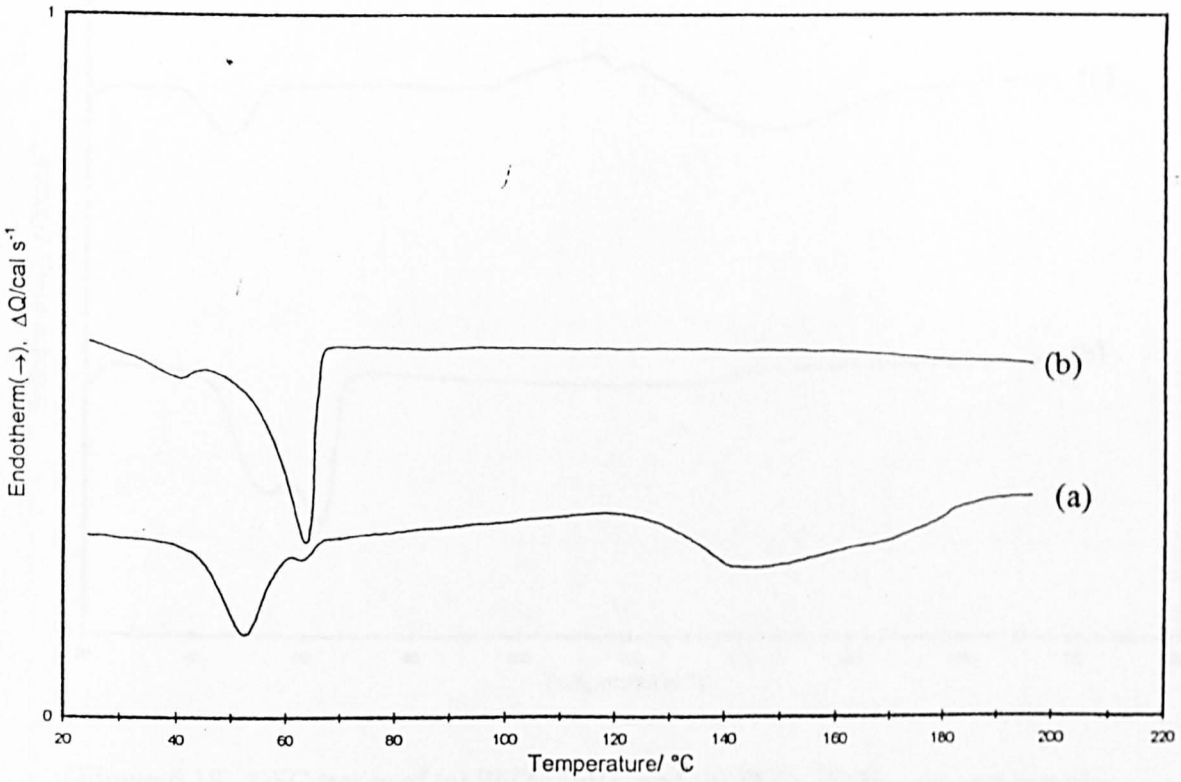

Figure 6.16 DSC traces of (a) PEO_8:$FeBr_3$ and (b) PEO_{20}:$FeBr_3$ dry samples.

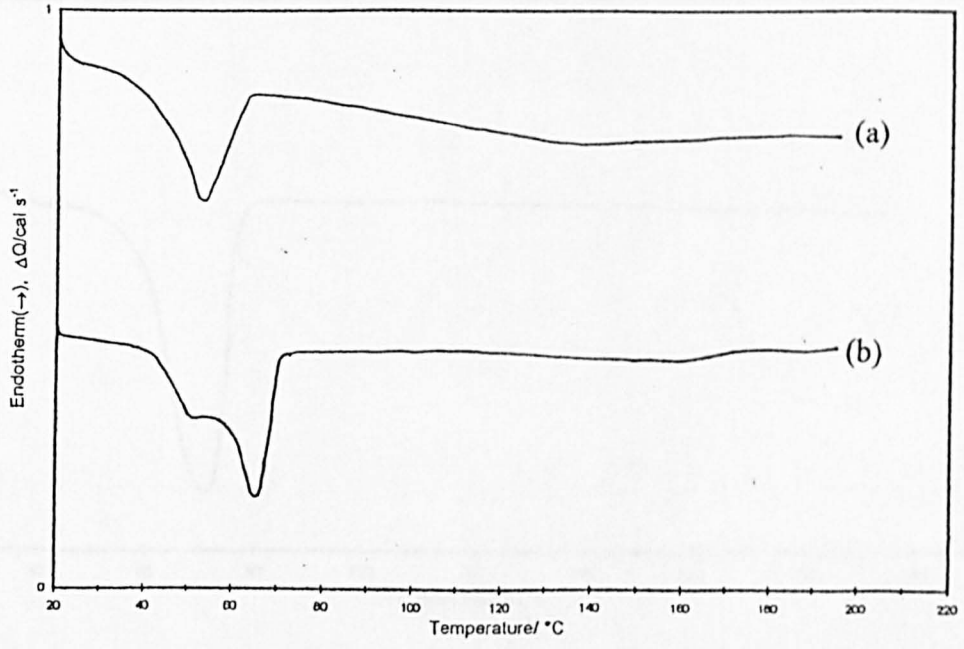

Figure 6.17 DSC traces of (a) PEO_8:$FeBr_2$ and (b) PEO_{20}:$FeBr_2$ air-cast samples.

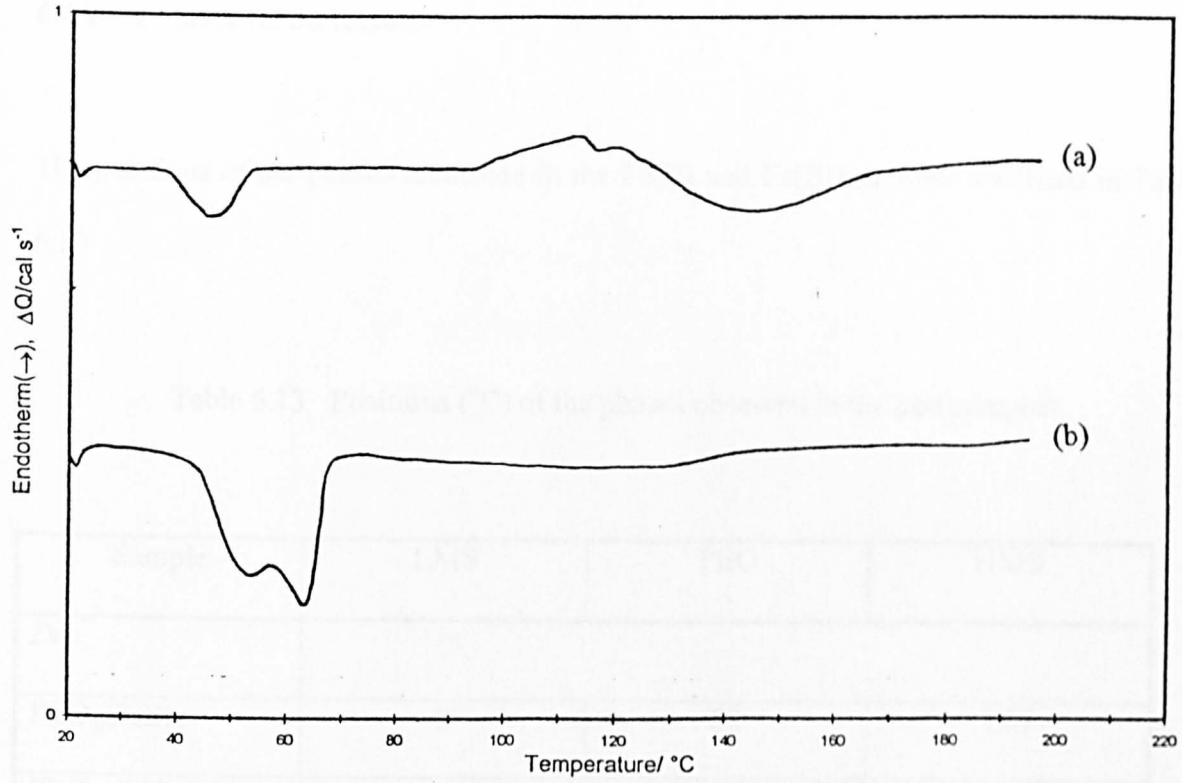

Figure 6.18 DSC traces of (a) PEO_8:$FeBr_3$ and (b) PEO_{20}:$FeBr_3$ air-cast samples.

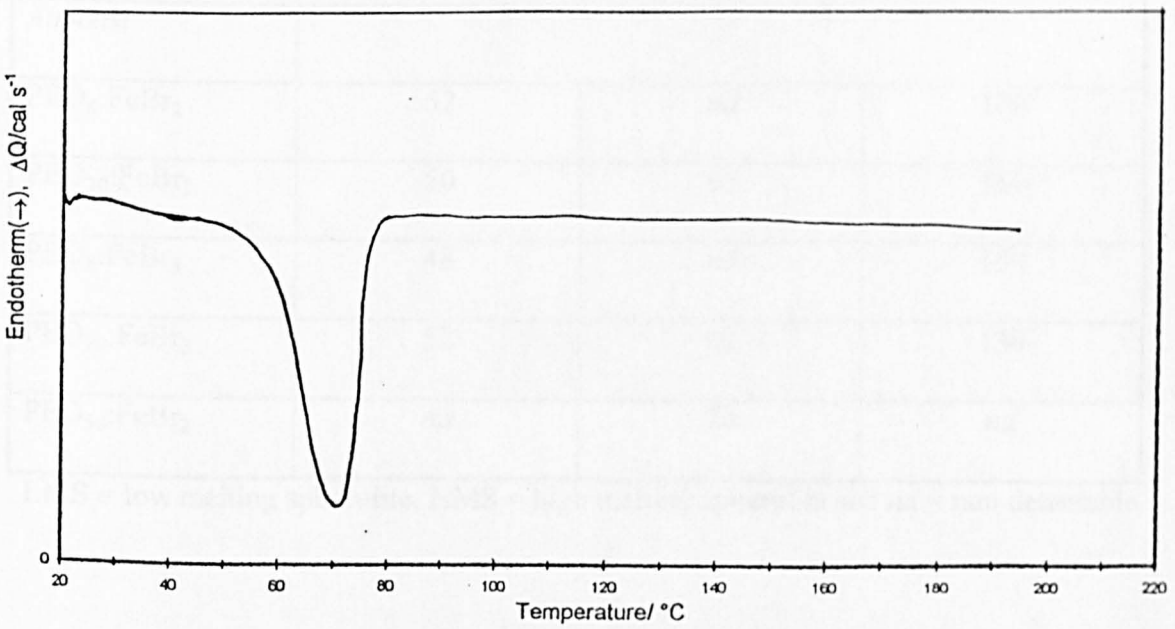

Figure 6.19 DSC traces of PEO_{50}:$FeBr_2$ air-cast sample.

6.4.1 Comments on Results

The positions of the phases identified in the Fe(II) and Fe(III) samples are listed in Table 6.13

Table 6.13 Positions (°C) of the phases observed in the iron samples.

Sample	LMS	PEO	HMS
Dry			
PEO_8:$FeBr_2$	40	58	180
PEO_{20}:$FeBr_2$	50	65	*nd*
PEO_8:$FeBr_3$	53	63	150
PEO_{20}:$FeBr_3$	40	63	*nd*
Air-cast			
PEO_8:$FeBr_2$	52	*nd*	140
PEO_{20}:$FeBr_2$	50	65	160
PEO_8:$FeBr_3$	48	*nd*	150
PEO_{20}:$FeBr_3$	52	62	130
PEO_{50}:$FeBr_2$	*nd*	70	*nd*

LMS = low melting spherulite, HMS = high melting spherulite and *nd* = non detectable.

There are a few differences, except for the dilute samples, between the DSC traces of the air-cast and dry samples. In the PEO_8:$FeBr_x$ and PEO_{20}:$FeBr_x$ (x = 2 and 3) of the dry

samples the PEO peak and the low melting spherulites are resolvable. Whereas, in the air-cast samples the two peaks are resolvable in the n = 20 sample but not in the n = 8. In the dry samples the low melting peak of PEO_n:$FeBr_3$ is more pronounced than PEO_n:$FeBr_2$, especially in the concentrated sample (n = 8) reflecting the amount present. In the PEO_8:$FeBr_x$ (x = 2 and 3) air-cast samples the PEO peak is absent and when it appears in the PEO_{20}:$FeBr_x$ (x = 2 and 3) it is again more pronounced in the Fe(III) sample.

6.5 Atomic Force Microscopy (AFM)

6.5.1 Introduction

AFM is based on scanning tunneling microscopy (STM) in which the 'aperture' is a tiny tungsten probe with a finely ground tip that could be only a single atom in width. The tip is manoeuvred to within a nanometer or two of the surface of a conducting specimen via piezoelectric controls. The distance is so close that electron clouds of the atom at the probe tip and of the nearest atom of the specimen overlap.

For STM, when a small voltage is applied to the tip, electrons 'tunnel' across the gap. The strength of the tunnelling current generated is sensitive to the width of the gap. *X* and *y* piezoelectric controls move the probe back and forth across the specimen surface in a raster pattern. If the probe maintained a steady height, the tunnelling current would fluctuate, increasing as the tip passed over bumps such as surface atoms and falling to

nothing as it crossed gaps between atoms. The probe moves up and down in consonance with the topography. A feedback mechanism senses the variations in tunnelling current and varies the voltage applied to a third, *z*, control. The *z* piezoelectric moves the probe vertically to stabilise the current and maintain a constant gap between the microscope's tip and the surface. The variations in the voltage applied to the *z* piezoelectric are electronically translated into an image of surface relief. STM image can reveal individual atoms if the probe is sharp, the controls precise and the fineness of the raster scan is sufficient.

What such images map is a surface of constant tunnelling probability. The tunnelling probability is not only affected by topography, but it is also affected by variations in the abundance and energies of surface electrons. When the specimen is composed of just a single element, tunnelling probability closely follows topography. A contaminant atom on an otherwise uniform surface may appear as an anomalous pit or bump, depending on its electronic properties. STM is largely restricted to imaging electrical conductors.

In 1985 Bennig, Quate and Gerber introduced the atomic force microscope (AFM), a scanned probe device that does not need a conducting specimen. The tip in this case is an atomically sharp shard of a diamond mounted on a strip of metal foil. In place of tunnelling current the AFM records contours of force - the repulsion generated by the overlap of the electron clouds of surface atoms. The tip deflection caused by the reflection is observed by means of a laser beam that is reflected off the foil. Movement of the foil

shifts the path of the reflected beam, so that a photocell placed in the beam path some distance away can detect tiny movements of the foil.

The signal from the photocell activates the *z* piezoelectric to maintain a steady tip displacement. The sample's movements are translated into a surface profile. The optical sensor provides a more reliable measure of tip deflection than the tunnelling sensor does, and so it renders the AFM's touch more consistent and gentle.

6.5.2 Experimental

A schematic diagram of an AFM is shown in Figure 6.20

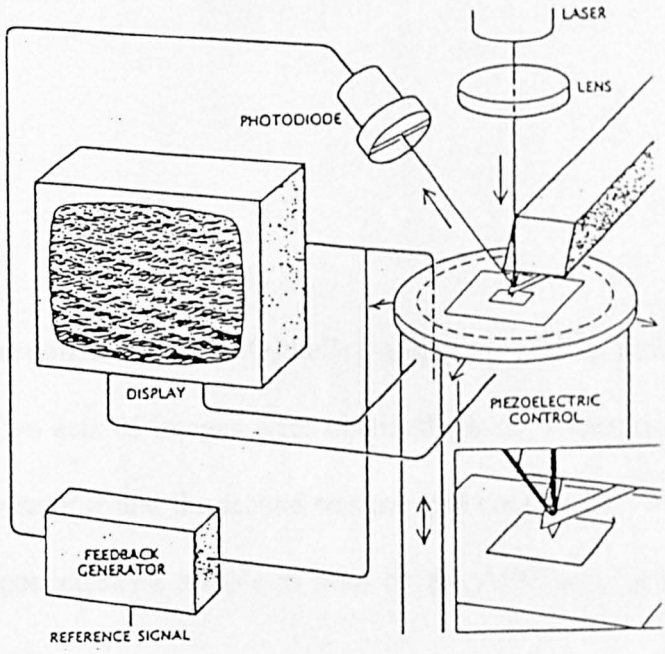

Figure 6.20 A schematic diagram of an AFM.

The samples used in the studies (PEO_n:$FeBr_2$; n = 8, 50 and 500) were prepared by a spin coat technique. Only one solvent cast sample (PEO_8:$FeBr_2$) managed to give a good image. In the spin coat technique, three drops of the polymer electrolyte solutions were placed on a spinning metal substrate until the solvent has evaporated (about one minute). The thin polymer electrolyte is cast on the substrate by the spinning action.

The sample is mounted on top of a tube scanner. Using the coarse and fine advance screws, the tip, mounted on a cantilever, is brought into gentle contact with the sample surface. By actuating the tube scanner, the tip is raster scanned over the sample surface. The force between the tip and the sample is detected by the photodiode. The signal, after amplification, is compared with a reference value. The difference signal, is again amplified to drive a feedback circuit. A constant force topographic image of the surface structure is obtained. Through some computation the image can be displayed as required.

6.5.2 Results

AFM images of the concentrated (PEO_8:$FeBr_2$) and dilute (PEO_{50}:$FeBr_2$) samples of Fe(II) were captured. Two sets of images were obtained for the concentrated sample; the first was the as cast dry sample and the second was the spin coat sample. Figure 6.21 (a) shows the image of the concentrated sample as seen by the AFM and in (b) with the contour lines.

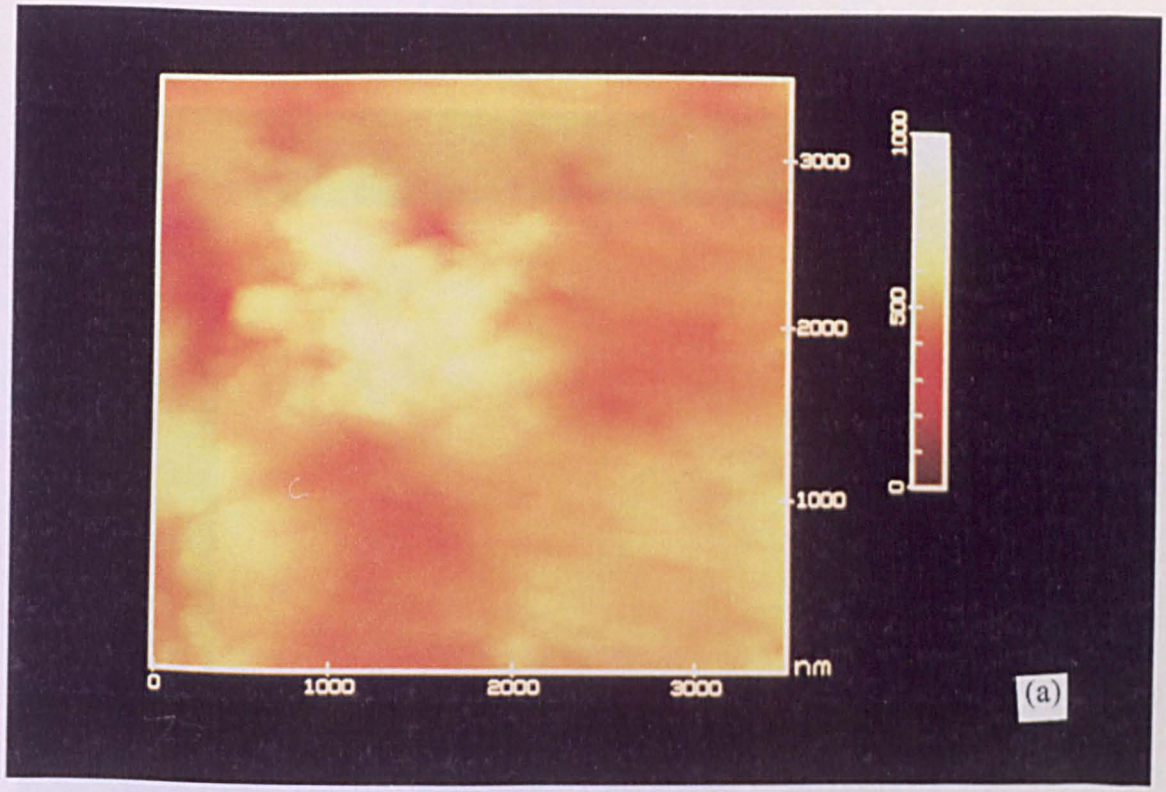

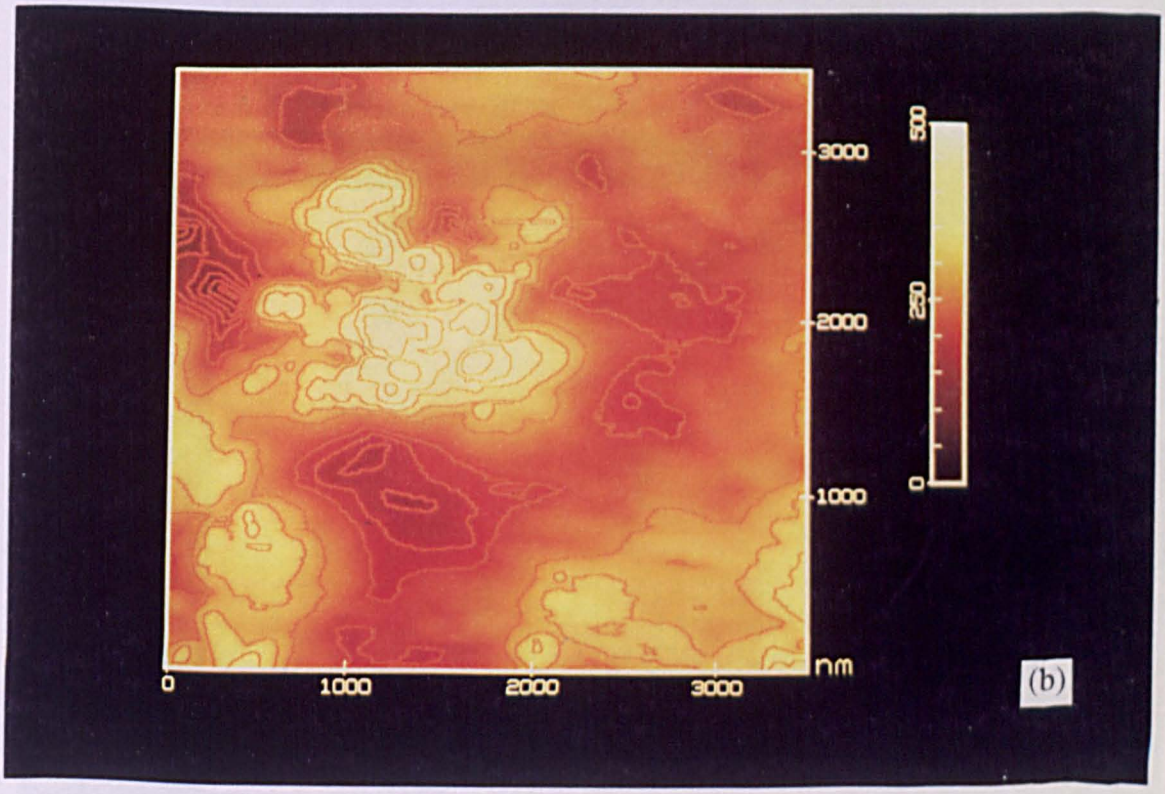

Figure 6.21 (a) Image of as cast PEO_8:$FeBr_2$ film seen by AFM, (b) with contour lines.

A clearer image can be seen in the surface view with the background hardened as depicted in Figure 6.22.

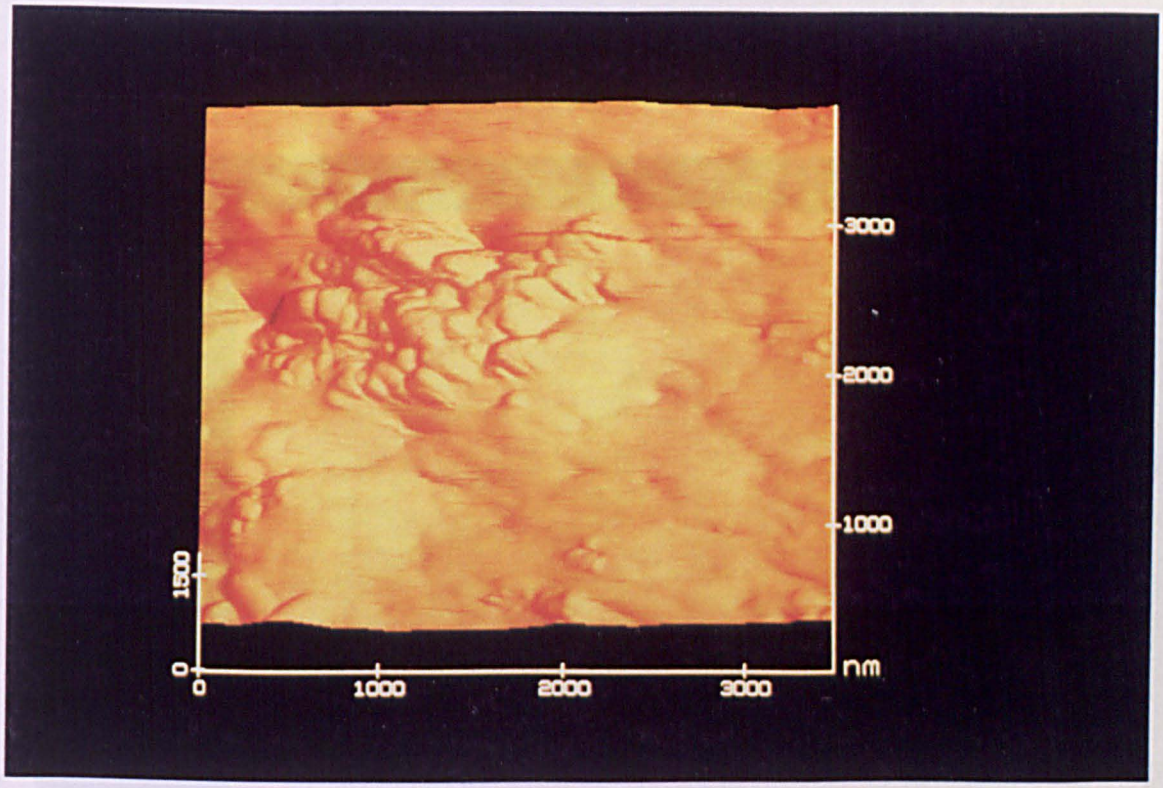

Figure 6.22 Surface view of the AFM image of the as cast PEO_8:$FeBr_2$ film.

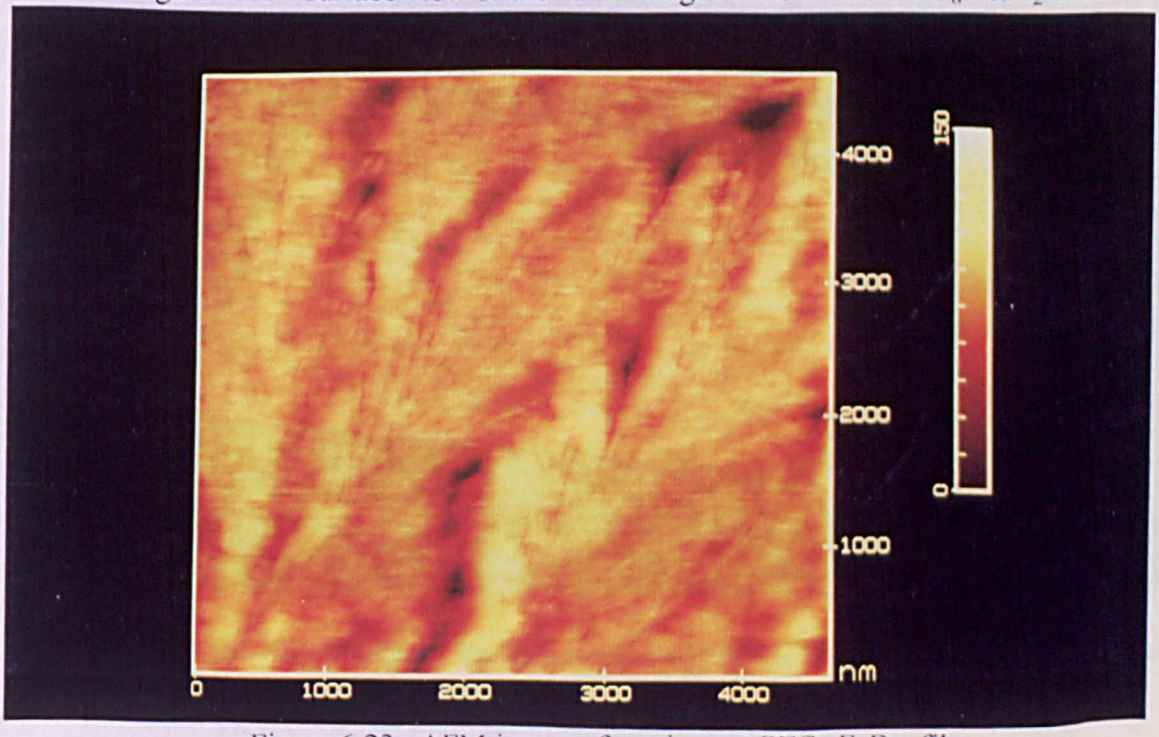

Figure 6.23 AFM image of a spin coat PEO_8:$FeBr_2$ film.

Figure 6.23 shows the image as seen by AFM of PEO_8:$FeBr_2$ spin coat film. This image shows the newly grown spherulites. The fibrils of the spherulites could be seen in the image. Images of the spin coat PEO_{50}:$FeBr_2$ sample are shown in Figure 6.24.

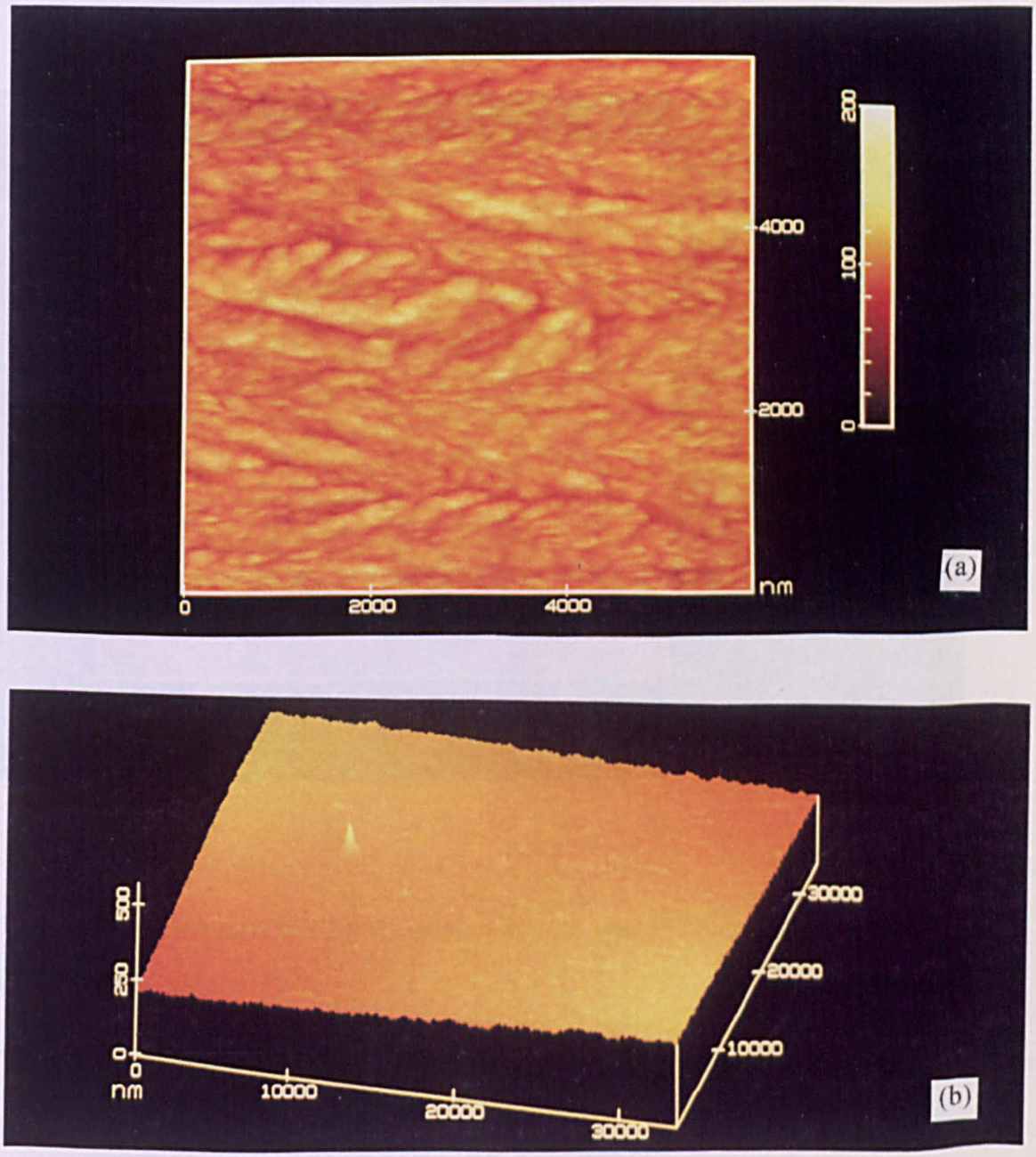

Figure 6.24 (a) AFM image of the dilute spin coat PEO_{50}:$FeBr_2$ sample and (b) Surface view of the AFM image of the dilute spin coat PEO_{50}:$FeBr_2$ sample.

A more dilute composition of the Fe(II) system has also been imaged. The AFM image of the spin coat PEO_{500}:$FeBr_2$ sample is shown in Figure 6.25.

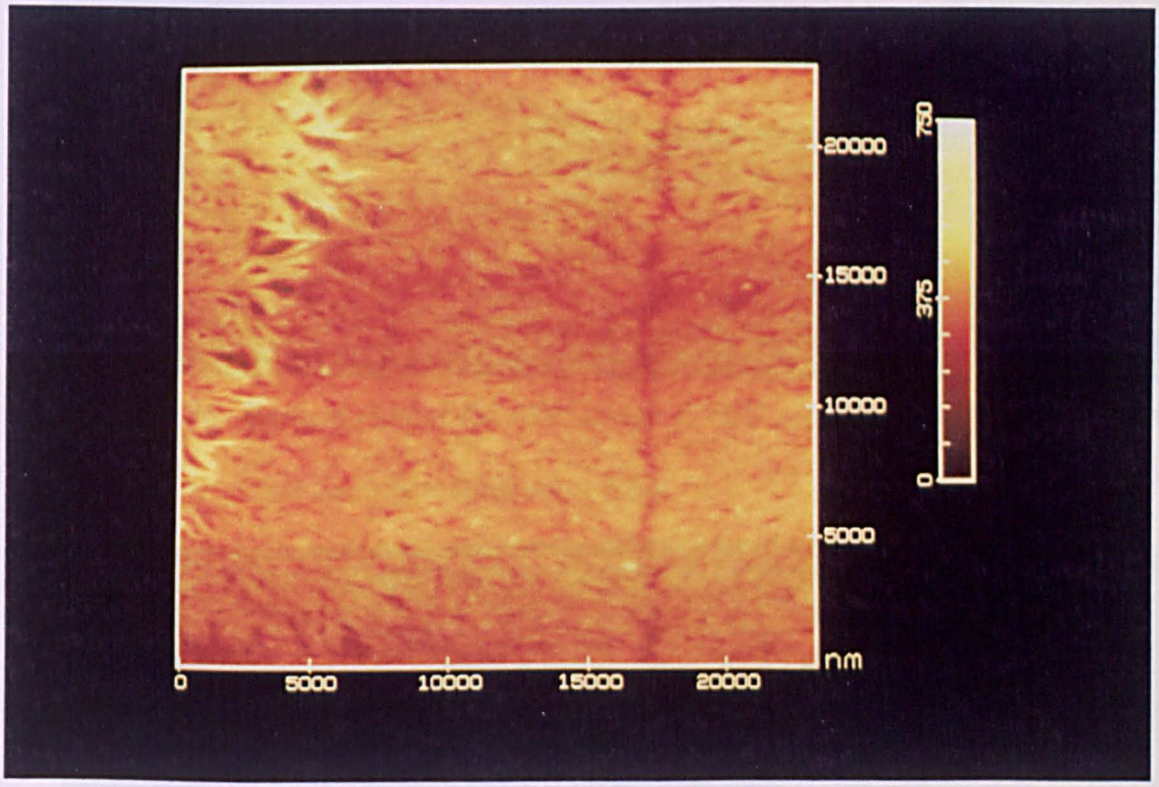

Figure 6.25 AFM image of the spin coat PEO_{500}:$FeBr_2$ film.

The line in the lower quarter of the picture is the boundary of spherulites merging and the bright structure on the upper right hand corner of the picture is a ridge. These features are shown clearly in Figure 6.26 and Figure 6.27.

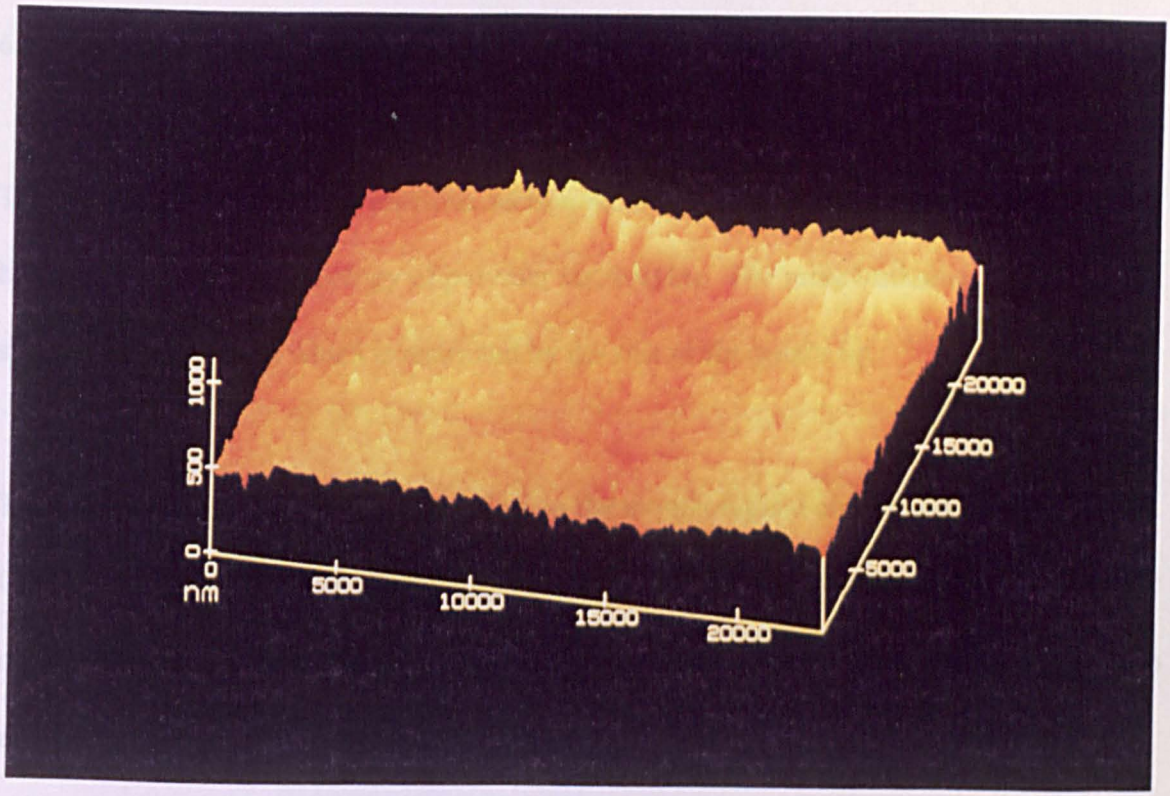

Figure 6.26 Surface view of the AFM image of PEO_{500}:$FeBr_2$ film showing the boundary between spherulites and a ridge.

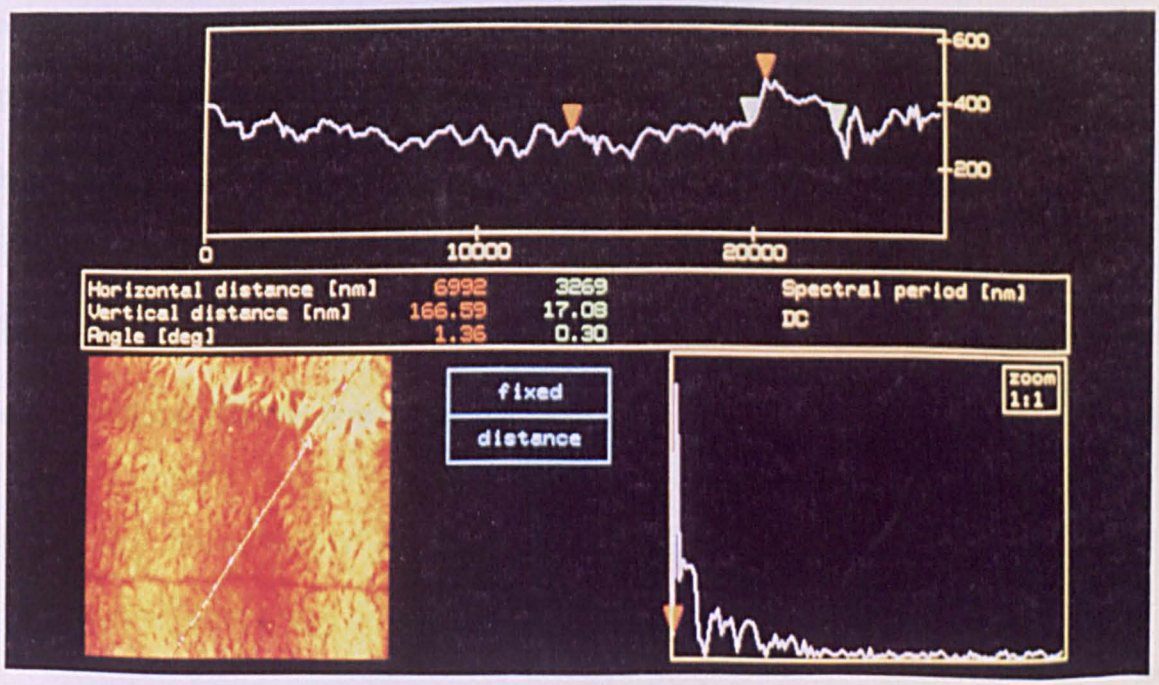

Figure 6.27 Cross-section of the AFM image of PEO_{500}:$FeBr_2$ film showing the depth of the boundary between spherulites and height of the ridge.

6.5.3 Comments on Results

The images presented in the previous section provide a general view of the potential AFM has in studying the morphology of polymer electrolytes. The main limitation in the present study is the resolution which is restricted by the size of the quartz tip.

The images captured provide information on the morphological complexity of the systems. On the one hand one could see a regular morphology with the size of the fibrils being the only difference, as for the PEO_{50}:$FeBr_2$ image; at the other extreme, the presence of ridges as in the image of PEO_{500}:$FeBr_2$ can be revealed.

The as cast samples are difficult to image. This is because the roughness of the film is too much for the tip to raster scan a decent image. The tip tends to scrape the surface of the film rather than hovering across. The surface view of the PEO_8:$FeBr_2$ image clearly showed some parts of the polymer electrolyte in the form of small spheres about 50 nm in diameter. There are areas in the film where the spherulitic regions are more localised. It is difficult to say whether that particular region is different in nature than the immediate surrounding, i.e. different type of spherulites.

6.6 Overview of Iron Systems

The preparation of the iron samples was straightforward, as for the other PEO-based polymer electrolytes but for the concentrated samples the solution should not be left stirring for longer than three days as the iron salt will degrade the polymer resulting in a less viscous solution. In the drying stage of the preparation there exists a metastable state where the texture of the films, especially the concentrated films, become rubbery and flexible; after cooling, the texture returns to the original state. This is due to the melting and recrystallisation of the low melting spherulites (LMS) which occur at about 45°C. This is confirmed by DSC studies.

DSC studies reveals clearly the presence of LMS and the amount fluctuates from an amount higher than in PEO spherulites to that lower than PEO. The presence of moisture in the preparative stage has an effect on the structure of the film. This is effectively so in the concentrated samples where the air-cast counterparts show only the LMS peak and not the PEO peak. This is reminiscent of Neat's (Neat, R.J.; 1988) classification of type I (HMS), type II (LMS) and type III (PEO) spherulites. It seems that the ratio of the LMS to the PEO peak is an important factor in determining the ionic conductivity of the samples.

The ionic conductivities of the dry iron samples show the expected behaviour, the concentrated sample (PEO_8:$FeBr_x$; x= 2 and 3) giving the highest conductivity in the series prepared. For the air-cast samples, the expected behaviour does not hold and it is difficult

to predict which composition has a higher conductivity (PEO_{20}:$FeBr_2$ for Fe(II) and PEO_{50}:$FeBr_3$ for Fe(III)).

The Arrhenius plots generally show a typical semicrystalline composition. There is a dip at high temperature (around 100°C) which is not typical of polymer electrolytes. It is thought that a non-conducting phase might have developed by phase separation (salting out) of the salts. To try to confirm this, a new technique, AFM, in studying the structure of polymer electrolytes has been employed. In the images obtained there appears to be phase separation taking place in the concentrated sample.

The XAFS studies show the complementary nature of the XANES and EXAFS. The shortening and the lengthening of the Fe - O bond have been shown to affect the position of the white line. It was found that the lengthening of the Fe - O bond shifts the position of the white line to lower energy. The shape of the spectra of the Fe(II) samples and the Fe(III) samples reflects the different coordination adopted and distinctly shown by EXAFS, six coordination for the Fe(II) samples and four coordination for the Fe(III) samples.

7.0 Introduction

This chapter will summarise the findings pertaining to the structure - conductivity studies in PEO-based polymer electrolytes of the multivalent salts. A general discussion will be given on the structural and conductivity studies carried out. At the end of the chapter some recommendations for further studies relating to polymer electrolytes will be outlined.

7.1 Structural Studies

Throughout the work two regimes of structural studies were undertaken, i.e. local structures and morphology. In the local structural studies, the complementary nature of XANES and EXAFS was noted. Changes in the interatomic distance, as shown by EXAFS, is synchronous with changes in the XANES features.

The XANES features that were found to give some responses were the shoulder on the rising side of the white line, the positions of the white line (representing the edge) and the shape of the post-edge peaks. The changes in the shoulder is exemplified by XANES studies of the PEO-modified nickel systems. The ligand to metal charge transfer was found to contribute to this feature and it is further enhanced by the presence of the electron

donating methyl group in the polymer. The position of the white line is determined very much by the oxidation state of the absorber atom and the interatomic distance. The dependence on the oxidation state is demonstrated by the Fe(II) and Fe(III) absorption spectra, where an energy of 2 eV separates the two edges, the same shift on other edges as found by other workers (Cramer et. al, 1976; Chan, Hu and Gamble, 1978). The interatomic distance of the target atom and the heteroatom of the polymer seems to be reflected in the position of the white line. The bromine atom seems to be tightly bound to the target atom, for both the zinc and iron systems. The observations in the iron systems indicate that lengthening of the Fe - O bond is accompanied by a shift in the white line. The shape of the post-edge is characteristic of the coordination of the target atom as shown by Fe(II) which is six -coordinated and Fe(III) which is four -coordinated.

The EXAFS results show greater precision in evaluating the interatomic distances and less in the coordination number. The immediate environment around the target atom provides evidence of cation solvation in zinc ultra dilute and iron polymer electrolytes. The EXAFS of the iron systems suggests that the anions are barely solvated by the polymer. The anions are stabilised in the polymer more by attraction to the cations than by interaction with the polymer chains. In the zinc ultra dilute samples, the structure resembles that shown in Figure 7.1. The cation is perhaps "pushed" closer to the polymer chain by coulombic anion-cation interaction as in a solvated ion pair. By contrast, the more concentrated systems studied by Cole *et al.* (1989) may be regarded as analogous to the contact ion pairs shown in Figure 7.2, the cation-chain interaction being less intimate. This comparison could lead one to expect shorter Zn-O distances in the ultradilute "pushed" systems than

those found in more concentrated systems. Comparison of Table 7.1 to Table 5.6 shows this to be the case.

Table 7.1 EXAFS results of PEO_n:$ZnBr_2$ (n = 12, 15, 20 and 30) (from Cole *et al.*, 1989)

Sample PEO_n:$ZnBr_2$	NNA	r (Å)	N	σ^2 (Å^2)	$E_o(eV)$
n = 12	O	2.130	6.4	0.052	15.53
	Br	2.339	2.1	0.012	
n = 15	O	2.113	6.6	0.055	14.91
	Br	2.339	1.8	0.011	
n = 20	O	2.094	6.2	0.047	16.55
	Br	2.333	2.2	0.014	
n = 30	O	2.037	5.7	0.046	17.56
	Br	2.338	1.8	0.009	

NNA= nearest neighbour atom; r= interatomic distance; N = coordination number; σ^2=Debye-Waller factor; E_o= difference between value at absorption edge energy from the experimental EXAFS spectrum and that found after data deconvolution.

In the refinement procedure the *afac* value is 0.8 and *vpi* is -2.

Comparison of the Zn-Br distances of n < 30 and n = 1000 and 2000 supports the arguement of contact ion pairs in the former case. It is interesting to observe that at still

higher dilutions, n = 3000, 4000, 5000 the Zn-Br distances are close to those for the concentrated system. This is discussed later.

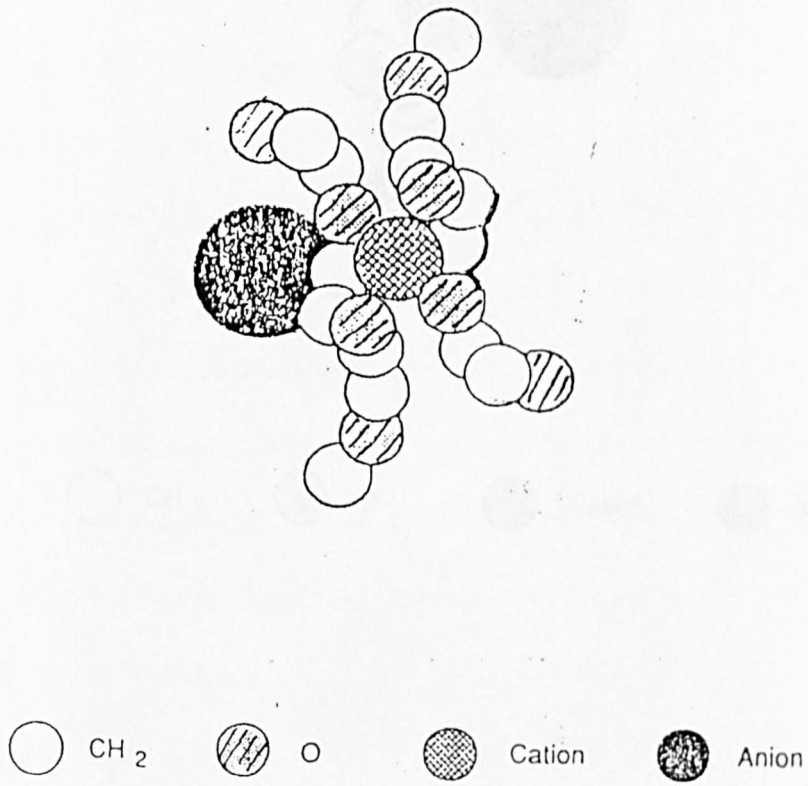

Figure 7.1 Solvated ion pair in PEO_n:$ZnBr_2$ (n > 2000).

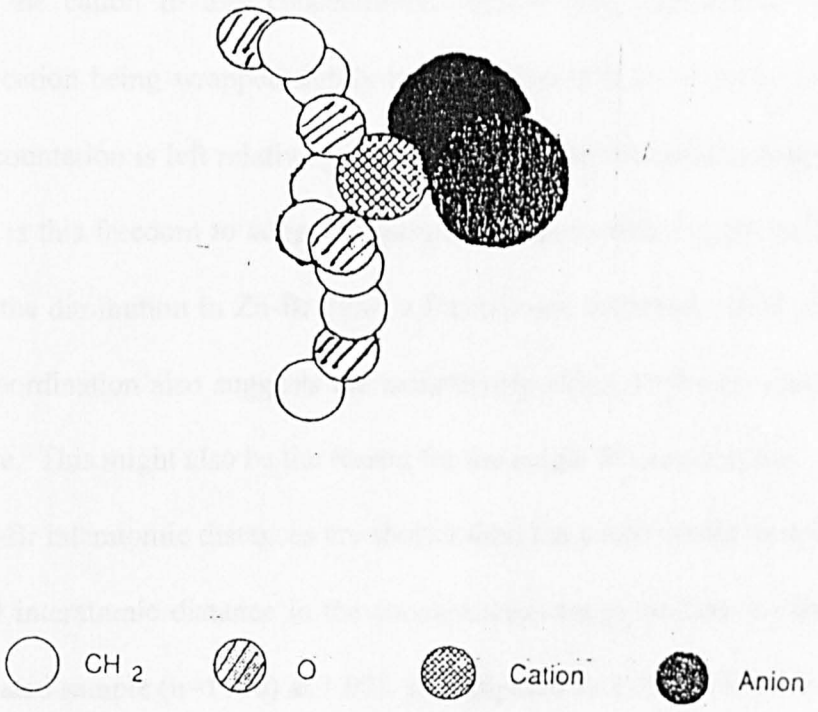

Figure 7.2 Contact ion pair in PEO_n:$ZnBr_2$ (n < 2000).

The EXAFS of the ultradilute samples studied show two different local environments. For the more concentrated system (< n=3000) the coordination is as in the 'normal'

concentration (n= 8) reported by Bandara and coworkers (Bandara *et al.*, 1994), at 2 oxygen and 2 bromine neighbours. The more dilute samples (> n=4000) show a coordination system of 3 oxygen and 1 bromine, similar to the results for PEO_8:ZnI_2 reported by Latham and coworkers (Latham *et al.*, 1989). The trend in these ultradilute systems is that the cation tends to coordinate more with the oxygen of the polymer and less with the counterion as the dilution is increased. This could be due to the low number or concentration of the cation in this concentration regime (very ultradilute) where the energetics of the cation being wrapped tightly by the polymer is more favourable. As a result of this the counterion is left relatively free with respect to the coordination sphere. It is possible that it is this freedom to adopt an optimum location with respect to the cation that may explain the diminution in Zn-Br ditance for extreme dilutions, noted previously. The high Zn-O coordination also suggests the neutralising effect on the Zn resulting in a less positive centre. This might also be the reason for the single Br coordination.

The Zn-O and Zn-Br interatomic distances are shorter than the concentrated samples (n=8). The longest Zn-O interatomic distance in the concentration range studied is exhibited by the most concentrated sample (n=1000) at 1.97Å as compared to 2.03Å in the concentrated sample (n=8) reported by Bandara *et al.*, 1994. In their studies on water cast systems, Einset and coworkers (Einset *et al.*, 1991) found that the undried sample exhibited a shorter Zn-O interatomic distance, 1.99Å as compared to 2.17Å for a dried sample. This gives an indication of solvation of the cation by the oxygen neighbours. In the ultradilute systems studied, as the dilution is increased the Zn-O interatomic distance gets shorter and the most dilute sample exhibits a Zn-O interatomic distance of 1.93Å. The Zn-O interatomic distance is slightly shorter than that in the ZnO model compound, 1.94Å. The

reason might be that there is a covalent polarization as it will lead to bond contraction (Phillips and Williams, 1966). There are reports of X-ray diffraction studies on zinc complexes where the Zn-O interatomic distance is less than 1.95Å. One of the zinc atoms in $Zn_5(P_3O_{10})_2.17H_2O$ possesses a Zn-O interatomic distance as short as 1.93Å (Johnson, 1978). Similarly, in $Zn_2HP_3O_{10}.6H_2O$ the Zn-O interatomic distance may be as short as 1.92Å (Johnson, 1978a). In one zinc polymeric complex, bis-(2-chlorobenzoato)zinc, each zinc is bonded in a tetrahedral fashion to four oxygens from four different ligands to form a chain-like structure exhibiting Zn-O interatomic distance ranging from 1.91 to 1.94Å (Johnson, 1978b). In another zinc polymeric complex, $MZnSO_4Cl$ (M=Rb and Tl), Zn is surrounded by an O_3Cl donor set, forming a distorted tetrahedron with Zn-O interatomic distance of 1.94-1.97Å (Johnson, 1978c). The zinc ultradilute samples may resemble closely with the local Zn environment thought of as a O_3Br cluster and Zn-O interatomic distance of 1.93-1.97Å. It is suggested that the polymer electrolyte could be regarded as having lattice-like configuration with the Zn surrounded by an O_3Br donor set forming a distorted tetrahedron. In principle the oxygens could come from more than one chain.

For the iron systems all the Fe-O interatomic distances in the Fe(II) samples are longer than for the Fe(III) counterparts. The values of the Fe-O interatomic distances in the dry samples are longer than the air cast samples. The Fe-O interatomic distances of the Fe(II) samples are shorter than the model compound by 0.48Å. The value exhibited by the concentrated samples, 2.14Å for the air cast samples and 2.15Å for the dry cast samples, are similar to $[Fe(H_2O)_6]^{2+}$ octahedra quoted in Phillips and Williams (1966a) at 2.17Å, 2.14Å and 2.10Å. Bailer *et al.* (1973) also quoted a similar value for $[Fe(H_2O)_6]^{2+}$ unit in

$[Fe(H_2O)_6]^{2+}$ unit in $(NH_4)_2SO_4.FeSO_4.6H_2O$ where one of the Fe-O interatomic distances is 2.14Å. For the dilute samples the Fe-O interatomic distance is shorter by 0.02Å in the dry sample and 0.08Å in the air cast sample. The value in the dilute air cast sample is similar to the Fe(III) samples. This suggests a similar local environment to the Fe(III) samples is present in the dilute air cast sample.

The value of the Fe-O distance exhibited by the concentrated samples, 2.07Å for the air cast samples and 2.09Å for the dry cast samples, are nearly the same to the Fe-O interatomic distance shown in Fe^{3+} (EDTA) (Phillips and Williams, 1966b) at a value of 2.05Å. The value of the Fe-O interatomic distance for the dilute samples of the Fe(III) system is the same for both the air cast and the dry cast samples with a value of 2.06Å.

The Fe-Br interatomic distance in all the samples, irrespective of the oxidation state of Fe and casting conditions, are the same at a value of 2.32Å. This value is similar to that in $(NMeH_3)_2FeBr_5$ (Wilkinson *et al.*, 1987) at 2.32Å.

In the EXAFS studies at various temperatures of the concentrated samples, the Fe-O interatomic distances for Fe(II) and Fe(III) at 70°C are slightly higher than that at 22°C. For both the Fe(II) and Fe(III) systems the difference is 0.01Å. The Fe-Br interatomic distance remains the same for both systems at the two studied temperatures. The Fe-O distances are different from those reported in Tables 6.7 and 6.8. The reason could be that the samples used in the temperature related studies were three months older. Since the polymer electrolyte systems are kinetically controlled and not thermodynamically controlled, the older samples might be more crystalline.

In morphological studies the techniques involved are DSC, VTPM and AFM. In DSC studies the low temperature transition phases of the polymer electrolytes studied were well defined but the high temperature transition is not easily determined due to the broadness of the peak and in the dilute and ultra dilute samples the peak is not resolvable. Nevertheless this technique helps to explain the texture of the iron samples during drying at 50°C.

VTPM has been very useful in identifying the types of spherulites. The various spherulites could be seen melting and appearing and the transition temperatures noted. It complements DSC in identifying the phases and transitions. The importance is clearly demonstrated in the ultra dilute samples where DSC fails to register the presence of the high melting spherulites which could be clearly seen in VTPM.

It is believed that AFM morphology studies have not previously been applied to studies of polymer electrolytes. Theoretically it is possible to image the polymer electrolytes on a molecular scale through this technique. The resolution of the images depends on the sharpness of the imaging tip and the smoothness of the sample. From the studies carried out it is possible to image the 100 μm as cast sample but the thinner samples obtained through spin coating provide better images and more details can be extracted. The tip in this study was not sufficiently fine to image molecular resolution. It would also be beneficial to incorporate a hot stage in the set up to look at the structure at which the conductivity is high.

7.2 Conductivity

The impedance spectra of the divalent salts polymer electrolytes display similar shapes at low and high temperatures, a typical big semicircle followed by a spike at low temperature changing to a small semicircle and a long spike. The trivalent iron complexes gave a slightly different picture. There is an additional semicircle which disappears as the temperature of the system is increased. This divergence suggests that the two systems have slight morphological differences. There might be some surface effects in the trivalent system as observed in composite systems (Ovenston and Walls, 1992). This would result in an additional resistance term in the system thus reducing the conductivity. The result is reflected in the generally low conductivity values in the trivalent iron samples compared with the divalent counterparts. The surface effects are not permanent; in fact they are temperature related, being absent at high temperatures (higher than the low melting spherulites).

Apart from the morphological difference there is also the local structural difference as reflected by the EXAFS results. The trivalent Fe ion is highly coordinated, 3 O and 3 Br, as compared to 2 O and 2 Br in the divalent systems. The trivalent ion coordination shows a tightly bound configuration which would hamper the process of dissociation from the coordination spheres followed by movement through the polymer matrix.

In the different preparative procedure studied in the iron systems, the dry method produced films with the highest conductivity composition of n = 8 irrespective of the valence state

of the cation whereas for the air-cast method the compositions that exhibit the highest conductivity are n = 20 for the divalent cation and n = 50 for the trivalent system.

7.3 Structure-Conductivity Relationships.

The ionic conductivity at low temperature (30°C) of the ultradilute systems is highest for the most concentrated sample in the series (n=1000) and the lowest is exhibited by the most dilute sample (n=5000). There is similarity in trends between the local structure and ionic conductivity in the ultradilute systems studied as shown in Figure 7.3.

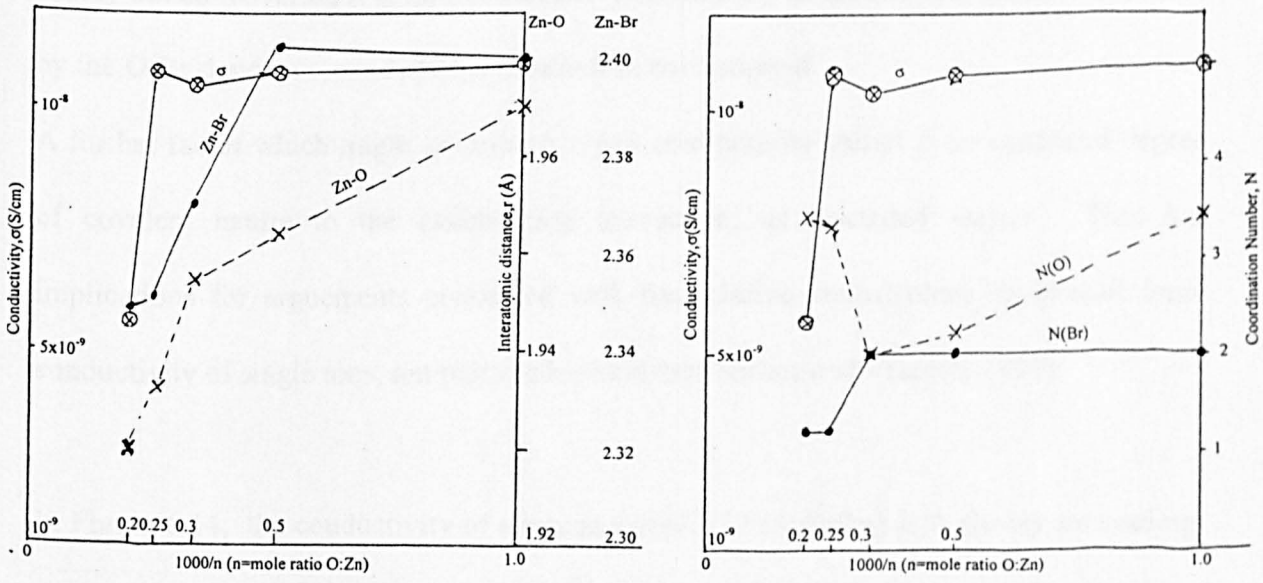

Figure 7.3 Trends between local structure and ionic conductivity in zinc ultradilute samples.

The system in which the Zn-O interatomic distance is the longest exhibit the highest conductivity. This is displayed by the most concentrated sample, n=1000. In the most dilute sample (n=5000) the Zn-O interatomic distance is the shortest. Furthermore, the cation in the most dilute sample has higher oxygen coordination number than that of the most concentrated sample, 3 and 2 oxygen respectively. These two factors, length of Zn-O interatomic distance and number of oxygen neighbour, are the main contributors to the low conductivity value. This is consistent with the findings of Andrews *et al.* (1988) for Ca polymer electrolytes in which a very high coordination number was reported. The conductivity of such systems is notoriously low. The short Zn-O interatomic distance is indicative of a more covalent character of the interaction. As a consequence the cation is tightly bound rendering it to be less mobile. The mobility of the cation is further restrained by the O_3Br donor set in a distorted tetrahedron environment.

A further factor which might contribute to low conductivity values is an enhanced degree of covalent nature to the cation-anion interaction, as discussed earlier. This has implications for arguements concerned with the relative contributions to overall ionic conductivity of single ions, ion pairs and ion clusters (Bruce and Vincent, 1989).

In Figure 6.14, the conductivity of a heated sample (PEO_8:$FeBr_2$) falls slowly on cooling. This could be for the following reason. As the temperature is increased the degree of crosslinking would be lowered which could result in the formation of nanoclusters in the concentrated sample. Evidence for nanocluster formation in Rb polymer electrolytes has recently been provided by the EXAFS studies of McBreen et al. (1995). These clusters

would cause a decrease in the crystallinity of the sample (Eisenberg and King, 1977). The crystallisation rate would then result in a gradual drop in conductivity of the sample on cooling.

7.4 Conclusions

Some general conclusions that can be drawn from the present studies are:

1. X-ray absorption fine structure studies (XAFS) should include XANES and EXAFS in order to provide a holistic view of the local structural environment. So far, XANES has been excluded in local structural studies in polymer electrolytes and the present studies found that XANES is a useful complement to EXAFS. On the other hand XANES alone was found not to be able to explain comprehensively the local structural environment as shown by the zinc temperature related studies.

2. XAFS studies suggest an activated state to the ionic conduction mechanism in which the M - O bond is stretched and this state dominates in the amorphous region.

3. The ultra dilute systems suggests local structure coordination characteristic of highly solvated ion pairs and for the more concentrated systems the dominant configuration is the contact ion pairs. The solvated ion pairs have a coordination sphere which is saturated with the heteroatoms. This reduces the free volume space which impedes

local segmental motion thus retarding the movement of charge carriers. In the contact ion pairs the cation is coordinated by the same number of anions as heteroatoms. There is enough free volume space to allow local segmental motion for ionic conduction.

4. The preparation related studies on the iron systems revealed the sensitivity of moisture in affecting the conductivity of PEO-based polymer electrolytes. The results suggest moisture encourages crystallization. The dry samples exhibit a high conductivity value at the most concentrated composition (n=8) prepared irrespective of the valence state of the cation whereas the air-cast samples show high conductivity values which are dependent on the valence state of the cation. For the iron systems the divalent cation showed a high conductivity value at the intermediate composition (n=20) and the trivalent cation at a dilute composition (n=50).

5. A surface effect, which is temperature related, is observed in PEO-based polymer electrolyte in a.c. impedance spectra. This phenomenon is shown by the Fe(III) samples irrespective of the compositions studied. This effect is also manifested in the Arrhenius plots where there is a dip in conductivity at high temperature (100°C). In the Fe(II) samples only the concentrated composition exhibits this phenomenon but it did not appear in the impedance spectrum.

6. Atomic force microscopy (AFM) can be succesfully employed in looking at the surface morphology of polymer electrolytes. Images taken of the as cast concentrated sample of Fe(II) sample showed the surface effect mentioned in 5.

7.4 Further Studies

Listed below are the recommendations for further studies on PEO-based polymer electrolytes with particular emphasis on structure-conductivity relationships:

1. In order to obtain a clearer picture of the local structures the anion edge should also be looked at. In the present studies Br was chosen as the anion so that XAFS of Br edge could also be studied. Unfortunately the beamtime allocated at the Synchrotron Radiation Source, Daresbury was on a station where the Br edge intensity is rather limited.

2. In the present studies the optimum conductivity of the dry samples was exhibited by the sample with the composition of n=8 irrespective of the valence state. It would be interesting to find out whether the optimum conductivity of PEO-based polymer electrolytes is around this composition for any other cations.

3. In the present EXAFS studies on the zinc samples at different temperatures it was found that the recrystallisation process was slow. The slow process will facilitate

crystallisation studies which could lead to a better understanding of the crystalline regime. This would reciprocate the understanding of the mixed morphology of the PEO-based polymer electrolyte systems. The same might apply to other di- and trivalent systems. Another aspect of crystallisation studies is annealing. This has not been intensively studied (McGhie, 1989) and it might have an impact on the recrystallisation process.

4. Transport number measurements would also be useful in the understanding of the conduction mechanism in these polymer systems. Some of the methods for measuring ionic transport number, as quoted by Watanabe and co-workers (Watanabe *et al.*, 1988), includes PFG-NMR measurements, tracer diffusion experiments, complex impedance measurements and Tubant method.

5. Atomic force microscopy should be continued. For a good AFM specimen the samples must be as thin and smooth as possible. Spin coat counterparts can always be prepared. The samples must also be free from undissolved substrate and this can be done by filtering the solutions before casting. To get high resolution the tip must be as fine as can be achieved.

6. Apart from the experimental results on the local structure, computer modelling could also be done which would further help the understanding of the conduction mechanism in these polymer systems.

Abraham (1993), Chapter 3 in *Applications of Electroactive Polymers*, ed. Scrosati, B., Chapman and Hall, London.

Abrahams, I.L., Bremner, I., Diakun, G.P., Garner, C.D., Hasnain, S.S., Ross, I. and Vasak, M. (1986), *Biochem. J.*, **236**, 585-589

Abrantes, T.M.A., Alcacer, L.J. and Sequeira, C.A.C. (1986) *Solid State Ionics*, **18/19**, 315-320

Abruna, H.D. (1990) in *'Advances in Chemical Physics'*, eds. Prigogine, I. and Rice, S.A., John Wiley, New York, p.270

Albinsson, I., Jacobsson, P., Mellander, B.-E. and Stevens, J.R. (1992) *J. Chem. Phys.*, **96**, 681-690

Albinsson, I., Jacobsson, P., Mellander, B.-E. and Stevens, J.R. (1992) *Solid State Ionics*, **53/56**, 1044-1053

Andrews, K.C., Cole, M., Latham, R.J., Linford, R.G. and Williams, H.M. (1988) *Solid State Ionics*, **28/30**, 929-935

Angell, C.A. (1964) *J. Phys. Chem.*, **68**, 1917-1929

Arai, K. and Eisenberg, A. (1980) *J. Macromol. Sci.-Phys.*, **817**, 803-832

Armand, M.B. (1987) in *Polymer Electrolytes Review-1*, (eds. MacCallum, J.R. and Vincent, C.A.) Elsevier, London, 23-37

Armand, M.B., Chabagno, J.M. and Duclot, M.J. (1978) *Second International Conference on Solid Electrolytes*, St. Andrews, paper 6.5

Armand, M.B., Chabagno, J.M. and Duclot, M.J. (1979) in *Fast Ion Transport in Solids* (eds. Vashishta, P., Mundy, J.N. and Shenoy, G.K.), Elsevier North-Holland, New York, p.131

Ashley, C.A. and Doniach, S. (1975) *Phys. Rev. B.*, **11**, 1279-1288

Bailer, J.C., Emeleus, H.J., Nyholm, R. and Trotman-Dickenson, A.F. (1973) in *Comprehensive Inorganic Chemistry* Vol. 3, Pergamon Press, Exeter, p.1026

Bair, R.A. and Goddard, W.A. (1980) *Phys. Rev. B.*, **20**, 2767-2776

Bandara, H.M.N., Schlindwein, W.S., Latham, R.J. and Linford, R.G. (1994) *J. Chem. Soc., Faraday Trans.*, **90**, 3549-3553

Bandara, H.M.N. (1995) Personal communication.

Bannister, D.S., Davies, G.R., Ward, I.M and MacIntyre, J.E. (1983) *Polymer*, **25**, 1291-1296

Bardwell, J.A., Davenport, A.J., Isaacs, H.S., Sproule, G.I., MacDougall, B. and Graham, M.J. (1992) in *X-ray Methods in Corrosion and Interfacial Electrochemistry* (eds. Davenport, A. and Gordon II, J.G.) New Jersey, p.254

Barrett, N.T., Gibson, P.N., Greaves, G.N., Mackle, P., Roberts, K.J. and Sacchi, M. (1989), *J. Phys. D: Appl. Phys.*, **22**, 542-546

Berthier, C., Gorecki, W., Minier, M., Armand, M.B., Chabagno, J.M. and Rigaud, P. (1983) *Solid State Ionics*, **11**, 91-95

Bianconi, A. (1980) *Appl. Surf. Sci.*, **6**, 392-418

Binks, A.E. and Sharples, A. (1968) *J. Polym. Sci.*, **6(A2)**, 407-420

Blake, R. L., Hessevick, R.E., Zolkai, T. and Finger, L.W. (1966) *American Mineralogist*, **51**, 123

Blonsky, P.M. and Shriver, D.F. (1986) *Solid State Ionics*, **18/19**, 258-264

Blumberg, A.A., Pollack, S.S and Hoeve, C.A (1964) *J. Polym. Sci.*, **2(A2)**, 2499-2502

Bonanos, N. and Butler, E.P. (1985) *J. Mat. Sci. Lett.*, **4**, 561-564

Bonanos, N. Slotwinski, R.K., Steele, B.C.H. and Butler, E.P. (1984) *J. Mat. Sci.*, **19**, 785-793

Bouridah, A., Dalard, F., Deroo, D and Armand, M.B. (1986) *Solid State Ionics*, **18/19**, 287-290

Bruce, P.G. (1987) in *'Polymer Electrolyte Reviews-1'*, eds. MacCallum, J.R. and Vincent, C.A., Elsevier, London, p.258

Bruce, P.G., Evans, J., Krok, F. and Vincent, C.A (1988) *Br. Polym. J.*, **20**, 193-194

Bruce, P.G., Krok, F. and Vincent, C.A (1988) *Solid State Ionics*, **27**, 81-88

Bruce, P.G., Hardgrave, M.D. and Vincent, C.A (1989) *J. Electroanal. Chem.*, **271**, 27-34

Bruce, P.G., and Vincent, C.A (1989) *Faraday Discuss. Chem. Soc.*, **88**, 43

Bruce, P.G., and Vincent, C.A (1993) *J. Chem. Soc. Faraday Trans.*, **89**, 3187-3203

Cameron, G.G., Harrie, J.L., Ingram, M.D. and Sorrie, G.A. (1988) *Br. Polym. J.*, **20**, 199-202

Careem, M., Glasse, M.D., Latham, R.J., Linford, R.G. and Schlindwein, W.S. (1993) *Ext. Abst. 9th. Int. Con. on Solid State Ionics*, (eds. Boukamp, B.A., Burggraaf, A.J. and Schoonman, J.), Oral-523.

Chadwick, A.C. and Worboys, M.R. (1987) in *Polymer Electrolytes Review-1*, (eds. MacCallum, J.R. and Vincent, C.A.) Elsevier, London, 275-313

Chan, S.I., Hu, V.W. and Gamble, R.C. (1978) *J. Molecular Struc.*, **45**, 239-266

Chatani, Y., Fujii, Y., Takayanagi, T. and Honwa, A. (1990) *Polymer*, **31**, 2238-2244

Chatani, Y. and Okamura, S. (1987) *Polymer*, **28**, 1815-1820

Citrin, P.H., Eisenberger, P. and Kincaid, B.M. (1976), *Phys. Rev. Lett.*, **36**, 1346-1349

Cole, M. (1996) Private communication.

Cole, M., Sheldon, M.H., Glasse, M.D., Latham, R.J. and Linford, R.G. (1989) *Appl. Phys.*, **A 49**, 249-257

Cramer, S.P., Eccles, T.C., Kutzler, F., Hodgson, K.O. and Mortenson, L.E. (1976) *J. Amer. Chem. Soc.*, **98**, 8059-8069

Doniach, S., Eisenbergger, P. and Hodgson, K.O. (1980) in *Synchrotron Radiation Research* (eds. Winick, H. and Doniach, S.) Plenum Press, New York, p.425

Doscher, T.M., Myers, G.C. and Atkins, D.C.Jr. (1951) *J. Colloid Sci.*, **6**, 223-235

Dupon, R., Papke, B.L., Ratner, M.A., Whitmore, D.H. and Shriver, D.F. (1982) *J. Amer. Chem. Soc.*, **104**, 6247-6251

Dupon, R., Whitmore, D.H. and Shriver, D.F. (1981) *J. Electrochem. Soc.*, **128(3)**, 715-717

Einset, A.G., Schlindwein, W.S., Latham, R.J., Linford, R.G and Pynenburg, R. (1991) *J. Electrochem. Soc.*, **138**, 1569

Eisenberger, A. and King, M. (1977) in *Ion-Containing Polymers:Physical Properties and Structure*, Academic Press, p.161

Eisenberger, P. and Brown, G.S. (1979) *Solid State Commun.*, **29**, 481-484

Eisenberger, P.M. and Kincaid, B.M. (1975) *Chem. Phys. Lett.*, **36**, 134-136

Fenton, B.E., Parker, J.M. and Wright, P.V. (1973) *Polymer*, 14, 589-589

Fontanella, J.J., Wintersgill, M.C., Calame, J.P., Pursel, F.P., Figueroa, D.R. and Andeen, C.G. (1983) *Solid State Ionics*, **9/10**, 1139-1146

Fontanella, J.J., Wintersgill, M.C., Calame, J.P. and Andeen, C.G. (1985) *J. Polym. Sci.*, **23**, 113-120

Fouss, R.M. and Kraus, C.A. (1933) *J. Amer. Chem. Soc.*, **A55**, 2387-2399

Frech, R., Manning, J., Teeters, D. and Black, B.E. (1988) *Solid State Ionics*, **28/30**, 954-957

Glasse, M.D. and Linford, R.G. (1987) in *Electrochemical Science and Technology of Polymers vol. 1* (ed. Linford, R.G.), Elsevier North-Holland, London, p. 23-43

Gorecki, W., Andreani, R., Berthier, L. and Armand, M.B. (1986) *Solid State Ionics*, **18/19**, 295-299

Gray, F.M. (1990) *Solid State Ionics*, **40/41**, 637-640

Gray, F.M. (1991) *J. Polym. Sci.*, **B29**, 1441-1445

Hagan, W.P., Latham R.J., Linford R.G. and Vickers S.L. (1994) *Solid State Ionics*, **70/71**, 666-669

Hall, P.G., Davies, G.R., Ward, I.M. and MacIntyre, J.E. (1986) *Polym. Comm*, **27**, 100-102

Harries, J., E., Hukins, D.W.L. and Hasnain, S.S. (1986), *J. Phys. C: Sol. St. Phys.*, **19**, 6859-6872

Hayes, T.M., Boyce, J.B. and Beeby, J.L. (1978) *J. Phys. C*, **11**, 2931-2937

Hibma, T. (1983) *Solid State Ionics*, **9/10**, 1101-1106

Huq, R. and Farrington, G.C. (1988) *Solid State Ionics*, **28-30**, 990-993

Huq, R., Saltzberg, M.A. and Farrington, G.C. (1989) *J. Electrochem. Soc.*, **136(5)**, 1260-1265

Ito, Y., Syakushiro, K., Hiratani, M., Miyauchi, K. and Kudo, T. (1986) *Solid State Ionics*, **18/19**, 277-281

James, D.B., Wetton, R.E. and Brown, D.S. (1979) *Polymer*, **20**, 187-195

Johnson, B.F.G. (1978) in *Inorganic Chemistry of the Transition Elements* **Vol. 6**, The Chemical Society, London, p.412

Johnson, B.F.G. (1978a) in *Inorganic Chemistry of the Transition Elements* **Vol. 6**, The Chemical Society, London, p.412

Johnson, B.F.G. (1978b) in *Inorganic Chemistry of the Transition Elements* **Vol. 6**, The Chemical Society, London, p.415

Johnson, B.F.G. (1978c) in *Inorganic Chemistry of the Transition Elements* **Vol. 6**, The Chemical Society, London, p.414

Kakihana, M., Schantz, S., Torell, L.M. and Stevens, J.R. (1990) *Solid State Ionics*, **40(4)**, 641-644

Killis, A., Le Nest, J.F., Gandini, A. and Cheradame, H. (1984) *Macromolecules*, **17**, 63-66

Lampreia, M.I. and Barreira, F. (1976) *Electrochim Acta*, **21**, 485-489

Latham, R.J., Linford, R.G. and Schlindwein, W.S. (1989) *Faraday Discuss. Chem. Soc.*, **89**, 103

Latham, R.J., Linford, R.G., Pynenburg, R.A.J. and Schlindwein, W.S. (1993) *J. Chem. Soc. Faraday Trans.*, **89(2)**, 349-354

Lee, P.A. and Pendrry, J.B., (1975), *Phys. Rev. B*, **11**, 2795-2811

Lever, A.B.P. (1968) *Inorganic Electronic Spectroscopy*, Elsevier Publishing Co., Amsterdam, p.204

Lightfoot, P., Mehta, M.A. and Bruce, P.G. (1992) *J. Mater. Chem.*, **2**, 379-381

Lightfoot, P., Mehta, M.A. and Bruce, P.G. (1993) *Science*, **262**, 883-885

Linford, R.G. (1989) in *Electrochemical Science and Technology of Polymers vol. 2* (ed. Linford, R.G.), Elsevier Applied Science, London, p. 291

Lundberg, R.D., Bailey, F.E. and Calard, R.W. (1966) *J. Polym. Sci.*, **4(A1)**, 1563-1577

MacCullum, J.R., Tomlin,A.S. and Vincent, C.A. (1986), *Eur. Polym. J.*, **22**, 787-791

MacCullum, J.R. and Vincent, C.A. (1987) in *Polymer Electrolytes Review-1*, (eds. MacCallum, J.R. and Vincent, C.A.) Elsevier, London, 23-37

McBreen, J., Yang, X.Q., Lee, H.S. and Okamoto, Y. (1995) *J. Electrochem. Soc.*, **142**, 348

McGhie, A.R. (1989) in *Electrochemical Science and Technology of Polymers vol. 2* (ed. Linford, R.G.), Elsevier Applied Science, London, p. 221

Morrel, E., Baines, J.T.M., Campbell, J.C., Diakun, G.P., Dobson, B.R., Greaves, G.N. and Hasnain, S.S. (1987) in *EXAFS users' Manual*, Daresbury Laboratory (Internal publication).

Moryoussef, A., Bonnat, M., Fouletier, M. and Hicter, P. (1985) *6th Riso Int. Sym. on Metallurgy and Materials Science*, 335-340

Nabavi, M., Taulele, F., Sanchez, C. and Verdegner, M. (1990) *J. Phys. Chem. Solids*, **51(12)**, 1375-1382

Neat, R.J. (1988) *Ph.D Thesis*, Leicester Polytechnic (De Montfort University), U.K.

Neat, R.J., Hooper, A., Glasse, M.D. and Linford, R.G. (1986) *Solid State Ionics*, **18/19**, 1088-1092

Ovenston, A. and Walls, J.R. (1992) *Solid State Ionics*, **55/56**, 825-830

Pandey, S.K. and Chetal, A.R. (1992) *Phys. Stat. Sol. (B)*, **170**, 631-635

Papke, B.L. (1987) *J. Phys. Chem. Solids*, **42**, 493-499

Papke, B.L., Ratner, M.A. and Shriver, D.F. (1981) *J. Phys. Chem. Solids*, **42**, 493-500

Papke, B.L., Ratner, M.A. and Shriver, D.F. (1982) *J. Electrochem Soc.*, **129(7)**, 1434-1438

Papke, B.L., Ratner, M.A. and Shriver, D.F. (1982) *J. Electrochem Soc.*, **129(7)**, 1694-1701

Parker, J.M, Wright, P.V. and Lee, C.C. (1981) *Polymer*, **22**, 1305-1307

Patrick, A.J. (1986) *Ph.D Thesis*, Leicester Polytechnic (De Montfort University), U.K.

Pearson, R.G. (1963) *J. Amer. Chem. Soc.*, **85**, 3533-3539

Petersen, G., Jacobson, P. and Torell, L.M. (1992), *Electrochim. Acta*, **37-9**, 1495-1497

Phillips, C.S.G. and Williams, R.J.P. (1966) in *Inorganic Chemistry* Vol. 2, Oxford University Press, Oxford, p.230

Phillips, C.S.G. and Williams, R.J.P. (1966a) in *Inorganic Chemistry* Vol. 2, Oxford University Press, Oxford, p.249

Phillips, C.S.G. and Williams, R.J.P. (1966b) in *Inorganic Chemistry* Vol. 2, Oxford University Press, Oxford, p.231

Pizzini, S., Roberts, K.J., Dring, L.S., Oldman, R.J. and Cupertino, C.C. (1993), *J. Mater. Chem.*, **3(8)**, 811-819

Pynenburg, R.A.J. (1994) *Ph.D Thesis*, De Montfort University, U.K.

Rawlins, D.J. (1992) in *'Light Microscopy'*, BIOS Scientific, Oxford, p.33

Robinson, J., Herron, M.E., Walsh, F.C., Doyle, S.E., Pizzini, S., Roberts, K.J. and Hards, G (1992) in *X-ray Methods in Corrosion and Interfacial Electrochemistry* (eds. Davenport, A. and Gordon II, J.G.) New Jersey, p.171

Schantz, S. (1991) *J. Chem. Phys.*, **94**, 6296-6305

Schantz, S, Kakihana, M. and Sanberg, M. (1988) *Solid State Ionics*, **40/41**, 645-647

Schantz, S., Sandahl, J., Borjesson, L., Torell, L.M. and Stevens, J.R. (1988) *Solid State Ionics*, **28/30**, 1047-1053

Schantz, S. and Torell, L.M. (1993) *Solid State Ionics*, **60**, 47-53

Schantz, S., L., Torell, L.M. and Stevens, J.R. (1991) *J. Chem. Phys.*, **94**, 6862-6867

Schlindwein, W.S. (1990) *Ph.D Thesis*, University of Leicester, U.K.

Shriver, D.F., Dupon, R. and Stainer, M. (1983), *J. Power Sources*, **9**, 383-388

Shriver, D.F., Papke, B.L., Ratner, M.A., Dupon, R., Wong, T. and Brodwin, W. (1981) *Solid State Ionics*, **5**, 83-88

Shulman, R.G., Yaffet, Y., Eisenberger, P.E. and Blumberg, W.E. (1976) *Proc. Natl. Acad. Sci. USA*, **73**, 1384-1388

Slotwinski, R.K., Bonanos, N. and Butler, E.P. (1985) *J. Mat. Sci. Lett.*, **4**, 641-644

Sorenson, P.R. and Jacobsen, T. (1983) *Solid State Ionics*, **9/10**, 1147-1154

Spindler, R. and Shriver, D.F. (1988) *J. Amer. Chem. Soc.*, **110**, 3036-3043

Stainer, M., Hardy, L.C., Whitmore, D.H. and Shriver, D.F. (1982) *J. Amer. Chem. Soc.*, **104**, 6247-6251

Steel, A.T., Feiters, M.C., Garner, C.D., Hasnain, S.S., Levason, W. and Higgins, S.J. (1985), *J. Chem. Soc. Chem. Comm.*, **8**, 484-485

Stern, E.A. (1974), *Phys. Rev. B*, **10**, 3027-3037

Stern, E.A., Sayers, D.E. and Lytle, F.W. (1975), *Phys. Rev. B*, **11**, 4836-4846

Stevens, J.R. and Jacobsson, P. (1991) *Can. J. Chem.*, **69**, 1980-1984

Takahashi, Y. and Takadoro, H (1973) *Macromolecules*, **6**, 672-675

Watanabe, M., Nagono, S., Sanui, K. and Ogata, N. (1988) *Solid State Ionics*, **28/30**, 911-917

West, A.R. (1984) *Solid State Chemistry and its Applications*, John Wiley, London, p.89

Williams, A.R. and Lang , N.D. (1978) *Phys. Rev. Lett.*, **40**, 954-957

Wilkinson, G., Gillard, R.D. and McCleverty, J.A. (1987) in *Comprehensive Coordination Chemistry* Vol. 4, Pergamon Press, Exeter, p.248

Winick, H. (1980) in '*Synchrotron Radiation Research*', (eds. Winick, H. and Doniach, S.) Plenum, New York, p.11

Wissburn, K.F. and Hannon, M.J. (1975) *J. Polym. Sci., Polym. Phys.*, **13**, 223-241

Wong, T., Brodwin, M., Papke, B.L. and Shriver, D.F. (1981) *Solid State Ionics*, **5**, 689-692

Yang L.L., Huq, R. and Farrington, G.C. (1986) *Solid State Ionics*, **18/19**, 291-294

Yokoyama, M., Ishihara, H., Iwamoto, R. and Tadokoro, H. (1969) *Macromolecules*, **2**, 184-192